

https://dspace.org/

Effect of particle filling and size on the behaviour of the ball load and power in a dry mill.

Kiangi, Kiangi Kimera.

2012-01-27
http://hdl.handle.net/10539/11183

Downloaded from a DSpace repository. https://dspace.org/

EFFECT OF PARTICLE FILLING AND SIZE ON THE BEHAVIOUR OF THE BALL LOAD AND POWER IN A DRY MILL

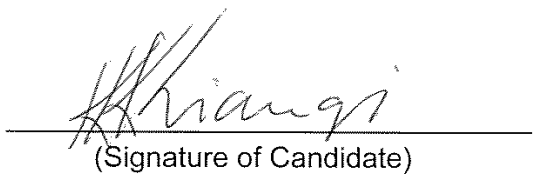
Kiangi Kimera Kiangi

A thesis submitted to the Faculty of Engineering and the Built Environment, University of the Witwatersrand, Johannesburg, in fulfilment of the requirements for the degree of Doctor of Philosophy.

Johannesburg, 2011

DECLARATION

I declare that this thesis is my own, unaided work. It is being submitted for the Degree of Doctor of Philosophy in the University of the Witwatersrand, Johannesburg. It has not been submitted before for any degree or examination in any other University.



(Signature of Candidate)

23rd Day of September (year) 2011

If I have seen further, it is by standing upon the shoulders of giants.

- Sir Isaac Newton

If one is to stand on the shoulders of giants, one must first climb up their backs; and the greater the body of knowledge, the harder this climb becomes.

- Benjamin Jones (Professor at the Kellogg School of Management, Northwestern University)

ABSTRACT

This study on the effects of particle filling and size on the ball load behaviour and power in a dry mill was initiated at the University of the Witwatersrand in 2003. The aim of the study was to make available a better understanding of the underlying causes in the different power draws that occur in mills when ore particles are being added to the ball load. This mimics the process of filling an industrial grinding mill after a grind out has been performed. Typically after a grind out, the mill operator would refill the mill with ore up to the point where maximum mill power draw is registered. At maximum power draw it is assumed that the void spaces within the ball load are filled with ore particles and that the charge is well mixed.

In order to conduct the study an inductive proximity probe was used to measure the dynamics of the load behaviour. This novel technique in measuring load behaviour was chosen due to the fact that the probe could sense the presence of steel balls independent of the presence of particles in the mill. The probe's response to a load comprised of steel balls only at the fillings of 15-45% and mill speeds of 60 – 105% indicate that the various changes in load behaviour such as cataracting, centrifuging, ball packing and toe and shoulder responses were easily distinguished in probes responses. Further tests were conducted in a mill with a 20% ball filling with increasing coarse or fine silica sand particle filling from 0 – 150% at the mill speeds of 63-98% of the critical mill speed. These tests

clearly reveal radial segregation of coarse silica sand, increased ball cataracting and centrifuging of just silica sand or a combination of balls and silica sand. The impacts of these phenomena have been discussed with reference to industrial mills.

The physical parameters defining the load provided by the inductive probe made it interesting to make use of Morrell's C model to simulate the power drawn by the mill. Modifications to Morrell's model were made thus leading to a modification in the toe and shoulder model and proposals for a segregated charge model, a centrifuged charge model and a particle pool model. Furthermore a modelling study based on the torque-arm modelling approach was conducted. Here Moys power model was used to study the effect increasing coarse and fine particle filling has on the power drawn by a mill. A liner model was proposed to define N* as a function of particle filling. In both modelling cases the models were used to account for the various conditions arising within the load as particle filling and mill speed increases.

DEDICATION

I dedicate this thesis to my wonderful parents, Dr. Peter M R Kiangi and Mrs. Helen W Kiangi, who have shown devotion, passion and unending support for my personal development and growth from childhood right up to now. God bless you both to live a long and happy life.

ACKNOWLEDGEMENTS

It is my pleasure to thank the people who made this thesis possible.

It is difficult to overstate my gratitude towards my PhD supervisor Professor M H Moys who took me under his wing and showed me how to use my previously gained undergraduate engineering knowledge in conducting mineral processing research. His enthusiasm, guidance, inspiration and occasional encouragement to push forward with my thesis will be forever cherished. Prof. Moys has been a true friend, advisor and mentor to me. I shall be forever indebted to him. Thank you very much.

I am also indebted to my fellow colleagues in Prof. Moys research group who provided a stimulating, fun and challenging environment to learn and grow. I am especially grateful to Dr M. Bwalya, Dr. H Dong, Mr. G Finnie, Mr C Couvas, Dr. J Kalala, Mr. G Monama, Mr L Niyoshaka and Mr A Makokha.

I am also grateful to the workshop staff who tirelessly worked on my requests to fabricate the necessary experimental equipment that I required.

I wish to thank my close friend and countryman, Dr. T Mwakabaga, who lent me his ears during my times of doubt. He has also been a good guide to my pursuit towards improving my computer programming skills.

Last but by no means least; I would like to thank God for blessing me throughout my life. He has blessed me with this journey through Wits and afforded me the opportunity to work under a great African scientist Prof. Moys.

========== **Ahsante Sana Na Mungu Awabariki**[1] ==========

.

[1] Swahili for Thank you very much and may God bless you all

TABLE OF CONTENTS

DECLARATION ..... **I**
ABSTRACT ..... **III**
DEDICATION ..... **V**
ACKNOWLEDGEMENTS ..... **VI**
TABLE OF CONTENTS ..... **VIII**
LIST OF FIGURES ..... **XI**
LIST OF TABLES ..... **XIV**

CHAPTER 1INTRODUCTION **1**
1.0 INTRODUCTION 2
1.2 OBJECTIVE OF THE THESIS 3
1.3 THESIS OUTLINE 3

CHAPTER 2 LITERATURE REVIEW **7**
2.0 INTRODUCTION 8
2.1 LOAD BEHAVIOUR MEASUREMENT TECHNIQUES 14
2.1.1 ACOUSTIC EMISSION MEASUREMENT TECHNIQUE 15
2.1.2 CONDUCTIVITY MEASUREMENT TECHNIQUE 17
2.1.3 VIBRATIONS MEASUREMENT TECHNIQUE 19
2.1.4 MOVEMENT, PRESSURE OR FORCE MEASUREMENT TECHNIQUE 22
2.1.5 X-RAY MEASUREMENT TECHNIQUE 26
2.2 MODELS FOR MILL POWER 28
2.2.1 EMPIRICAL MILL POWER MODELS 29
2.2.1.1 Rose and Sullivan's Power Model *31*
2.2.1.2 Bond's Power Model *33*
2.2.1.3 Fuerstenau, Kapur and Velamakanni's Power Model *34*
2.2.1.4 Moys Power Model *37*
2.2.1.5 Morrell's Power Model *41*
2.2.2 MECHANISTIC MILL POWER MODELS 45
2.2.2.1 The Discrete Element Method (DEM) *46*
2.3 CONCLUSION 50

CHAPTER 3 MEASUREMENT TECHNIQUE **52**
3.0 INTRODUCTION 53
3.1 THE INDUCTIVE PROXIMITY PROBE 54
3.2 EXPERIMENTAL EQUIPMENT AND METHOD 56

3.3 INDUCTIVE PROXIMITY PROBE SIGNAL ANALYSIS 56
3.3.1 DESCRIPTION OF THE INDUCTIVE PROXIMITY PROBE'S SIGNAL 59
3.4 EXPERIMENTAL RESULTS AND ANALYSIS 62
3.4.1 INDUCTIVE PROXIMITY PROBE'S SIGNAL AS A FUNCTION OF MILL SPEED 62
3.4.2 INDUCTIVE PROXIMITY PROBE'S SIGNAL AS A FUNCTION OF MILL FILLING 65
3.4.3 LOAD ORIENTATION AS A FUNCTION OF MILL SPEED AND MILL FILLING 67
3.4.4 COMPARISON OF THE INDUCTIVE PROBE WITH THE FORCE PROBE 68
3.5 CONCLUSION 70

CHAPTER 4 EXPERIMENTAL STUDY 71
4.0 INTRODUCTION 72
4.1 EXPERIMETAL EQUIPMENT AND METHOD 73
4.2 RESULTS AND DISCUSSIONS 76
4.2.1 EFFECT OF PARTICLE FILLING AND PARTICLE SIZE ON THE NET POWER 76
4.2.2 EFFECT OF PARTICLE FILLING AND PARTICLE SIZE ON THE BALL LOAD BEHAVIOUR 78
4.3 RADIAL SEGREGATION WITHIN THE LOAD 85
4.4 EFFECT OF REDUCING THE CHANGE IN PARTICLE SIZE DISTRIBUTION 89
4.5 CONCLUSION 90

CHAPTER 5 MODELLING STUDY 1 93
5.0 INTRODUCTION 94
5.1 MORRELL'S MODEL 95
5.2 ANALYSIS AND DISCUSSIONS 97
5.2.1 MODELLING OF THE COARSE PARTICLE EFFECTS 98
5.2.2 MODELLING THE EFFECTS OF RADIAL SEGREGATION 106
5.2.3 MODELLING OF THE FINE PARTICLE EFFECTS 113
5.3 CONCLUSION 118

CHAPTER 6 MODELLING STUDY 2 120
6.0 INTRODUCTION 121
6.1 MOYS POWER MODEL FRAMEWORK 121
6.2 ANALYSIS AND DISCUSSIONS 124
6.2.1 MODELLING OF COARSE PARTICLE EFFECTS ON POWER 125
6.2.2 MODELLING OF THE FINE PARTICLE EFFECTS ON POWER 130
6.3 CONCLUSION 134

CHAPTER 7 CONCLUSION AND RECOMMENDATION 137
7.0 CONCLUSION 138

REFERENCES 147

APPENDIX 1.....155
A1.1 EXPERIMENTAL DATA FOR THE COARSE PARTICLE EXPERIMENTS 156
A1.2 EXPERIMENTAL DATA FOR THE FINE PARTICLE EXPERIMENTS 158

APPENDIX 2.....160
A2.1 MIXED CHARGE MODELLING.....161
A2.2 CENTRIFUGED CHARGE MODELLING 167
A2.3 SEGREGATED CHARGE MODELLING 179
A3.4 POOL POWER MODELLING USING SIMPSON'S METHOD 187
A2.5 MATLAB PROGRAM: POOL'S TORQUE AND POWER.....195

APPENDIX 3.....207
A3.1 REGRESSION ON BALLS ONLY DATA.....208
A3.2 REGRESSION ON POWER DATA FROM COARSE PARTICLE EXPERIMENTS 210
A3.3 REGRESSION ON POWER DATA FROM FINE PARTICLE EXPERIMENTS 218

LIST OF FIGURES

Chapter 2

Figure 2.1	Variations in load behaviour with increasing mill speed	10
Figure 2.2	Specific rates of breakage as a function of particle size	12
Figure 2.3	Specific rates of breakage as a function of particle and ball filling	13
Figure 2.4	Assembly diagram for the conductivity probe	18
Figure 2.5	Illustrations of movement and pressure probes	23
Figure 2.6	Force probe installed in an industrial mill	24
Figure 2.7	Tri-axial force sensor installed in a Hicom nutating mill	26
Figure 2.8	Illustration of the torque-arm load shape	31
Figure 2.9	Illustration of Fuerstenau et al simplified load shape	35
Figure 2.10	Illustration of Moys simplified charge shape	38
Figure 2.11	Illustration of Morrell's simplified charge shape	42
Figure 2.12	Spring-slider-dashpot model for interactions between two particles	47

Chapter 3

Figure 3.1	Inductive proximity probe's assembly	52
Figure 3.2	Inductive proximity probe's static response curves for a 30mm steel ball at various distances away from the probe's centre	54
Figure 3.3	Dynamic response of the inductive proximity probe	55
Figure 3.4	Typical signal from the inductive proximity probe for a mill filling of 35% and a mill speed of 75% of the critical mill speed	57
Figure 3.5	Inductive probe's signal as a function of mill speed for a load filling of 35%	60
Figure 3.6	Photographs of the load behaviour as a function of mill speed for a load filling of 35%	61
Figure 3.7	Inductive proximity probe's signal as a function of mill filling for a mill speed of 75% of the critical mill speed	62
Figure 3.8	Load behaviour as a function of load filling for a mill speed of 75% of the critical mill speed	63
Figure 3.9	Load orientation as a function of mill speed and filling measured by the inductive proximity probe	64
Figure 3.10	Inductive proximity and force probe signals for J =15% and N = 75%	66

Chapter 4

Figure 4.1	Photograph of the mill and the installation of inductive proximity probe	71
Figure 4.2	Photographs of the coarse and fine particles	72
Figure 4.3	Variations in net power draw with particle filling at different mill speeds for a ball filling of 20%	74
Figure 4.4	Inductive probe's signal, ball load orientation and Power draw as particle filling increases at 63% of the critical speed for a ball filling of 20%	76
Figure 4.5	Inductive probe's signal, ball load orientation and Power as particle filling increases at 78 and 88% of the critical speed for a ball filling of 20%	78
Figure 4.6	Inductive probe's signal and ball load orientation as particle filling increases at 98% of the critical speed for a ball filling of 20%	80
Figure 4.7	Effect of particle filling and mill speed on radial segregation	85
Figure 4.8	Net power, ball load orientation and Inductive probe signal as particle filling increases at 76% of the critical and a ball filling of 20%	87

Chapter 5

Figure 5.1	Morrell's C load behaviour model description	93
Figure 5.2	Load orientation, power and the inductive probe average signal for the mill speeds of 63% and 78% of the critical	96
Figure 5.3	Load orientation, power and the inductive probe average signal for the mill speeds of 88% and 98% of the critical	100
Figure 5.4	Centrifuging of the charge for both segregated and mixed charge conditions	103
Figure 5.5	Variation of coarse particle radial segregation with mill speed and particle filling	104
Figure 5.6	Illustration of the radial segregation charge model	106
Figure 5.7	Modelling the variation of the radial segregation index with particle filling for various mills speeds	107
Figure 5.8	Load orientation, power and the inductive probe average signal for the mill speeds of 63%, 78% and 88% of the critical	112
Figure 5.9	Load orientation, power and the inductive probe average signal for the mill speeds of 98% of the critical speeds	115

Chapter 6

Figure 6.1	Moys power model predictions and the inductive probe average signal for the mill speeds of 63% and 78% of the critical	123
Figure 6.2	Moys power model predictions and the inductive probe average signal for the mill speeds of 88% and 98% of the critical	125
Figure 6.3	Moys power model predictions and the inductive probe average signal for the mill speeds of 63%, 78% and 88% of the critical	129
Figure 6.4	Moys power model predictions and the inductive probe average signal for the mill speeds of 98% of the critical speeds	130

LIST OF TABLES

Chapter 3

Table 3.1	Bulk toe, Load locked in and Shoulder angular positions for a mill filling of 35% and a mill speed of 75% of the critical	57
Table 3.2	Analysis of the inductive and force probe signals for five revolutions for J = 15% and N = 75%	66

Chapter 6

Table 6.1	Established parameters for a balls only load	122

CHAPTER 1

INTRODUCTION

1.0 INTRODUCTION

The power drawn by grinding mills has a complex non linear relationship to the various variables that affect it. Such variables are load volume, load density, mill speed, mill dimensions, liner type, particle size distribution and ore properties etc. The power is related to the dynamic behaviour of the load within the mill. Any significant influence that these variables have on the load orientation will surely cause a change in the power drawn by the mill. Studying the load behaviour can bring about an improved understanding of the effects that various variables have on the efficient transfer of energy from the mill shell to the load and on the grinding efficiency. Furthermore, correlations between these variables and their effects on mill power have been developed.

Ball mills are typically operated close to their maximum power draw. At the maximum power draw, it is assumed that the ball charge is well mixed and void spaces between the balls are filled with particles. But, in reality, particles can influence the ball charge in various ways causing the maximum power draw to shift depending on the nature of the influence. The ball load contributes to the bulk of the charge mass; consequently a change in the location of its centre of gravity significantly affects the power drawn by the mill. It is therefore worthwhile to study the behaviour of the ball charge and the influence particles have on it. From such a study, one can infer the conditions within the charge that lead to maximum power

draw and optimal throughput. This insight can lead to significant improvements in production capacity, energy efficiency, mill control and design. Furthermore the development and improvement of mill power models can be a benefit from such a study.

1.2 OBJECTIVE OF THE THESIS

The objective of this thesis is to understand the influence particle filling and size have on the load behaviour and power in a dry grinding mill. This objective was achieved by developing a novel technique in load behaviour measurements by using an inductive proximity probe so as to measure the ball load behaviour independently of the particles present in the mill. A further understanding of these effects is brought about by using Morrell's power model (Morrell, 1993) to model the power as a function of increasing particle filling. Furthermore torque arm model was used in the form of Moys power model to gain an added insight into the effect particles have on the mill power and the challenges faced in modelling the power draw as the load behaviour changes with increasing particle addition.

1.3 THESIS OUTLINE

This thesis is divided into seven chapters including this introduction. The following is a brief outline of the content of the various chapters and where they chapters have been published:

Chapter 2: This chapter gives a review of published work on load behaviour measurement techniques and the development of select power models used to predict mill power draw. The power model development targets models developed from various simplified load behaviour shapes, their advantages and disadvantages and further discussions of the Discrete Element Method and its strengths as a useful tool in mill design and optimisation.

Chapter 3: A novel measurement technique requiring the use of an inductive proximity probe is described in this chapter. Tests on the probe to determine its suitability in measuring load behaviour are presented. A comparison of load behaviour measurements from the probe and photographs are presented. The probe is then compared to a force probe to display its advantages over the force probe in load behaviour measurements. This chapter has been published in the Minerals Engineering Journal (Kiangi & Moys, 2006) and presented in the South African Institute of Mining and Metallurgy - Mineral Processing Conference 2005, Somerset west, South Africa.

Chapter 4: This chapter analyses the experimental study on the effects of particle filling and size on the load behaviour and power in a dry pilot mill using the inductive probe as a measurement tool. A copy of this chapter has been accepted for publication by the Powder Technology journal. This

chapter has been presented in the South African Institute of Mining and Metallurgy - Mineral Processing Conference 2006, Newlands, South Africa and the Joint Symposium of Chemical and Metallurgical Engineering, 2007, Pretoria, South Africa. Second prize was won for the presentation of this experimental data at the Joint Symposium of Chemical and Metallurgical Engineering, 2007.

Chapter 5: Morrell's model is used to model the experimental results from chapter 4. Necessary modifications to the physical parameters that define the load behaviour in Morrell's model were made. The modified model has been used to simulate the power drawn by a load comprised of balls and coarse silica particles and that comprised of balls and fine silica particles. The effect of radial segregation within the coarse particle charge has been included in the modified model.

Chapter 6: The torque arm model in the form of Moys power model is used to model the power having gained insight into the impact increasing coarse or fine particle filling has on the behaviour of the ball load and power drawn by the mill via chapter 4 and 5. The parameter N* in Moys power model was used to model the effects particles filling has on the power draw. In all cases N* was either kept as a constant value meaning it was independent of particle filling or made to be a linear model that was a function of the particle filling. In conditions where both cataracting and centrifuging resulted as particle filling was increased as the mill's speed

remained constant better power predictions were achieved by using separate linear models to define the parameter N* over the load condition.

Chapter 7: This chapter draws up the main conclusions on the study. Recommendations for further research are also made.

CHAPTER 2

LITERATURE REVIEW

2.0 INTRODUCTION

The power drawn by a tumbling mill depends on the dynamics of the charge motion. Accurate measurements and descriptions of the charge motion have been the central focus of mill power modelling research. Accurate and precise measurements of the load behaviour (i.e. toe and shoulder angular positions) avails the possibility of an additional mill control variable. Ideally, controlling the load behaviour through the variables that affect it could lead to a stable mill power draw and likewise a consistent mill product. Alternatively, a mill power prediction model can be used to control the mill. The challenge a researcher faces here is to draw up a power model based on a sound and good description of the charge behaviour as affected by various variables such as mill filling, mill speed, liner profile, charge density, particle filling, slurry viscosity etc. The more representative the load behaviour model is of the actual load dynamics the more accurate the predictions in the mill power draw. Obviously, this would lead to an increase in the physics content of the model so that it can accurately describe the interactions of the balls and ore (not to forget the slurry when a wet mill is considered) within the load and the load and its surrounding environment. Such a model exists and is based on Discrete Element Methods (DEM) which was developed by Mishra and Rajamani (1992). Due to the high computational demand and lengthy time required to carry out DEM simulations the model cannot be used to carry out simple and quick on the spot power calculations but rather it has earned its

reputation as an advanced modelling research tool for understanding and improving tumbling mills or other mineral processing equipment. Simpler models such as the torque-arm whose load description resembles the quarter moon are still dominantly used for mill power draw calculations. Torque arm power prediction models are less accurate at higher speeds (i.e. mill speeds > 60%) as they treat the charge as a single body and fail to accurately describe the cataracting or centrifuging portion of the charge.

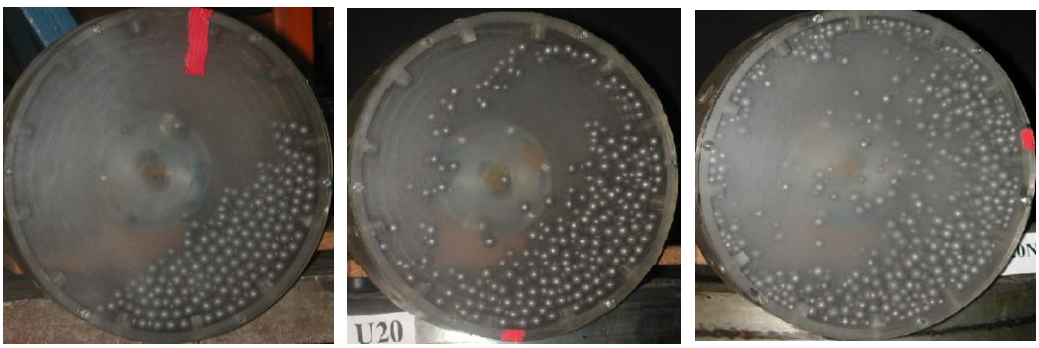
Depending on the mill's speed, visual analyses of a ball charge reveal the following characteristic behaviour of the charge:

Cascading – Occurs at low mill speed (i.e. <60% of critical speed). Once the charge material has emerged from the shoulder of the load it then rolls down the free surface of the charge to the toe of the load (Fig. 2.1a). Breakage of particle in this mode is by abrasion and attrition.

Cataracting – Occurs at mill speed less than the critical speed (< 100% of critical speed) but greater than cascading speeds. This behaviour is characterised by some of the charge material being projected from the shoulder clear of the free surface of the load and then the material either lands on the surface of the load close to the toe or strikes the mill shell and enters the toe (Fig. 2.1b). The cataracting intensity increases with mill speed and so does the tendency of cataracting material striking the exposed mill shell. Cataracting of charge onto the exposed mill shell

reduces the mill's power and increases liner and ball wear thus reducing the mill's efficiency. It is preferred that the high energy impacts of the cataracting balls go to the breakage of large particles.

Centrifuging – Occurs at mill speed in excess of the critical speed (>100% of critical speed) and in the absence of the load slipping on the liner (Fig. 2.1c). Here the outermost layer of charge in contact with the mill shell is centrifuged first and rotates with the mill shell followed by the inner layers of the charge should the mill speed be increased. Centrifuging reduces the mill diameter and also causes part of the charge to become inactive. In this case mill efficiency is reduced by the mill drawing less power mainly due to a decreased mill diameter and a reduced throughput will be registered as a portion of the charge will not participate in the milling action.



a) Cascading b) Cataracting c) Centrifuging

Figure 2.1: Variations in load behaviour with increasing mill speed

Surging - This phenomenon occurs in mills fitted with smooth liners (i.e. no lifters). The whole charge in the mill moves in a cyclic-like motion around the centre of the mill. At one part of the motion, the whole charge becomes keyed into the rotary motion of the mill it then slips and moves in a counter direction to the mill rotation (Agrawala et al, 1997; Vermeulen and Howat, 1986; Rose and Sullivan, 1958). Surging of the charge is more evident in mills with a low ball filling (J < 30%). It can lead to excessive liner wear and cyclic mill noise.

Mill speed, liner profile, particle size distribution, particle filling and ball filling are among some of the variables that can affect the load behaviour, power draw and specific grinding rates in a mill. Austin et al (1984) clearly demonstrates how these variables affect the power drawn by a mill and likewise how the specific grinding rates are affected. Typically in a ball mill as the mill speed increases so does the mill power up to its maximum power draw then drops with subsequent increases in the mill's speed. The maximum power draw occurs in the range of 70-85% of the mill's critical speed. The normal specific grinding rates vary with mill speed in a similar fashion to the power draw. The normal specific grinding rates experience relatively small changes at mill speeds near where the maximum in power draw occurs. Thus in order to maximise the specific grinding rates in a mill it will have to be operated close to its maximum power draw. This will lead to improved grinding efficiencies.

Smaller particles are considered to be relatively stronger than larger particles due to less Griffith flaws to initiate crack propagation as implied on the theory of fracture. Furthermore, it is less likely that a given mass of small particles will be nipped as compared to similar mass of large particles.

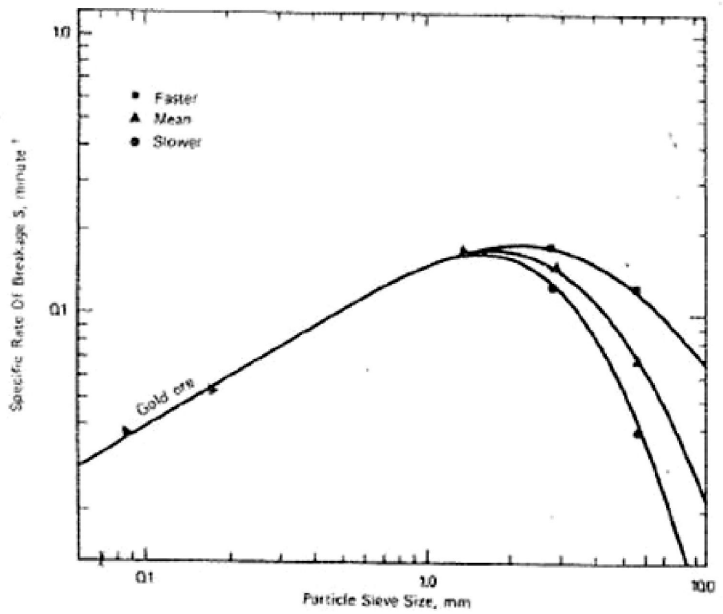


Figure 2.2: Specific rates of breakage as a function of particle size (*Courtesy Austin et al, 1984*)

For smaller particles, as seen in Figure 2.2, the specific rates of breakage increase with increasing particle size up to a critical particle size after which the specific grinding rates will decrease with increasing size. This critical size varies from one ore type to another and is normally larger for softer ore types. The smaller sizes are considered to undergo first order breakage (normal breakage) while the larger sizes undergo non-first order

breakage (abnormal breakage). In the case of abnormal breakage the particle sizes are considered to be too big for the energy of the tumbling balls to be used efficiently in causing fracture. The inclusion of lifters in a mill and higher mill speeds tend to increase the rates of breakage of coarse particles as a result of the increase of high energy impacts from cataracting balls.

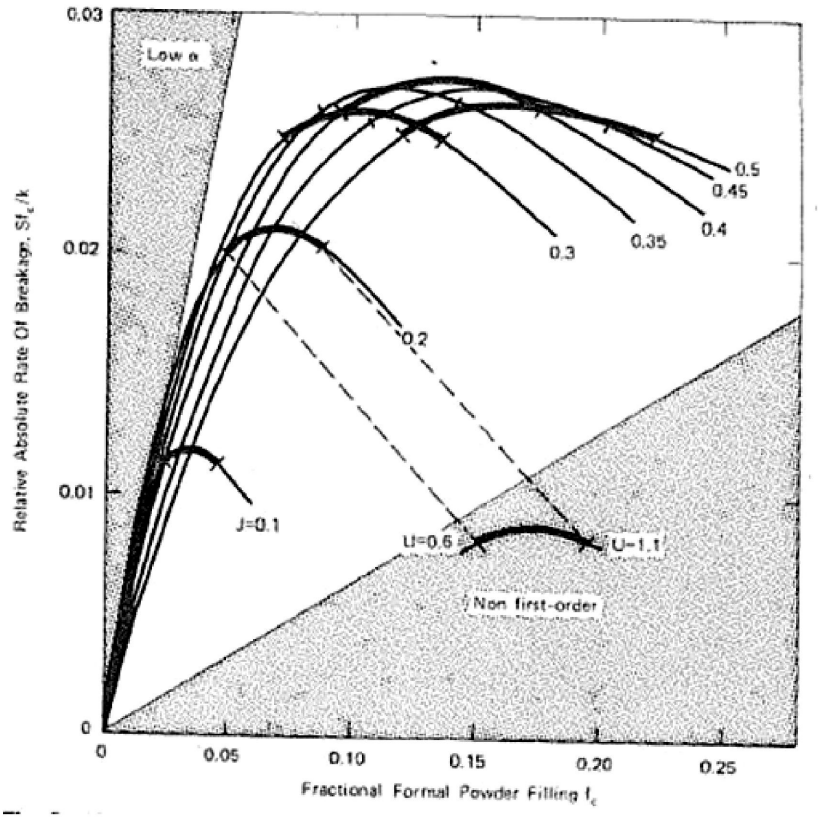


Figure 2.3: Specific rates of breakage as a function of particle and ball filling (*Courtesy Austin et al, 1984*)

A low particle filling gives a small rate of breakage, as seen in Figure 2.3. Increasing the particle filling will lead to the spaces between the balls being filled and thus increasing the rates of breakage to a point where the

void spaces are totally filled with particles (i.e. U=1). Increasing the particle filling beyond this point will cause a decrease in the relative breakage rate due to the fact that the collision zones are already saturated. Thus at a given ball load it is undesirable to underfill or overfill a mill with particles. In the case of low particle fillings (i.e. U<0.6) much of the energy is taken up in steel to steel contact thus giving low values of volume of particles broken per unit time per unit mill volume. Likewise steel on steel contacts increase the chances of increased ball and liner wear. In the case of high particle fillings (i.e. U>1.1) the particles cushion the breakage action thus resulting in a low value of the volume of particles broken per unit time per unit mill volume. In order to maximise the breakage rates for a specific ball load an optimum particle filling of between 0.6 - 1.1 should be used.

Various techniques have been explored to measure the load behaviour within a mill and are reviewed in detail below. Likewise, selected power models and their basis of development are discussed.

2.1 LOAD BEHAVIOUR MEASUREMENT TECHNIQUES

The dynamic behaviour of the load can be measured either by mounting the sensor directly onto the mill shell or mounting off the mill shell. On mill sensors rotate with the mill and are able to provide continuously information directly related to the condition of the mill charge at every point on the mill. The challenges faced with this method include, effective

methods of transmitting power and data from the sensor to a place off the mill.

On-mill sensors that are placed in the mill through liner bolts (Vermeulen, Ohlson and Schakowski, 1984) are always exposed to the harsh elements within the mill and wear with time; variations in temperature within the load can also cause a drift in the measurement made by the instrument. Such factors that affect accurate and precise measurements have to be put into consideration when calibrating the probes.

Off-mill sensors are normally fixed at one position close to the mill shell and do not rotate with the mill. They monitor events related to conditions within the charge indirectly as process variables are changed. With these sensors it would be impossible to know the condition of the charge within the mill. Through monitoring the events one can infer the conditions of the mill that would lead to an efficient operation. A few techniques have been reviewed below.

2.1.1 Acoustic Emission Measurement Technique

The grinding process in mills produces a lot of noise (acoustic emissions), which depending on the conditions in the mill, can vary at different extents of intensity. Experienced mill operators have been known to use this noise to discern the load conditions within the mill. Acoustic emissions are transient elastic waves within a material that are generated by an external

stimulus such as mechanical loading. The acoustic emissions can provide a measure of the characteristics of the charge or its motion within the mill. In the past, microphones have been used to measure the sound intensity generated from charge impacting onto the liners with the intention of using this measurement in controlling industrial mill feed rates (Harding, 1939). Here, the control philosophy would be the emptier the mill the noisier it is and vice versa. Jaspan et al (1986) used multiple microphones to control the pulp density and viscosity in a mill equipped with load cells and found the system suitable for mill power draft maximisation and water addition control. Recent interests in this area are analysing the acoustic emission spectrum produced by mills subsequently relating it to mill control variables (Watson, 1985). This involves the acquiring of data from a microphone in time domain and converting it into frequency domain using Fast Fourier Transforms (FFT). In frequency domain the spectrum contains information related to the grinding process and mechanical process occurring in a mill. Further analysis of this frequency spectrum is done using a range of spectroscopic techniques. Pax (2001) preferred the use of multiple sensors over a single sensor to acquire time domain data due the sensors individually providing spatial information related to the load condition at their location and likewise he was able to average the coincident signals.

The challenge faced with acoustic emission measurement techniques is that the analysis of the sound frequency spectrum must be able to isolate

the frequencies due to the grinding process from other background sources. The identification of the unique conditions of the charge prevalent within the mill to the sound frequency spectrum is not straight forward and more work has to be done. Any changes to the mill internals (i.e. liner profile and grinding media shape) or operating conditions (i.e. wet or dry mill, overflow or grate discharge, mill speed, ball filling etc) will have an impact on the acoustic emission intensity. Thus the recalibration of the sensor will have to be done to correct for these changes.

2.1.2 Conductivity Measurement Technique

This technique explores the use of the ability of the load to conduct an electric current when the probe is in contact with the load. The technique relies highly on the successful contact of the steel balls, wet autogenous load or slurry with the probe's assembled members. For a load comprised of particles and balls in a dry mill, continuous current conduction between the load and the probe is highly unlikely thus making the conductivity probe not an attractive option for measuring load parameters in a dry mill. Conductivity varies with temperature and should be kept in mind as the probe shall experience drift in the value being measured as the load temperature varies.

Moys (1985) pioneered the use of conductivity probes for analysing load behaviour in a pilot ball mill. This probe was mounted into the mill and the length of the probe's sensing face was parallel to the mill axis. The long

head of the probe allowed it to provide sharp changes in conductivity as it enters and leaves the load. The probe was isolated from the bolt and reinforcing channel by epoxy putty thus eliminating any chance of electrical conductance between them (Figure 2.4). Successful continuous contact between the balls, wet autogenous load or slurry and the probes assembled members enabled a probe's response.

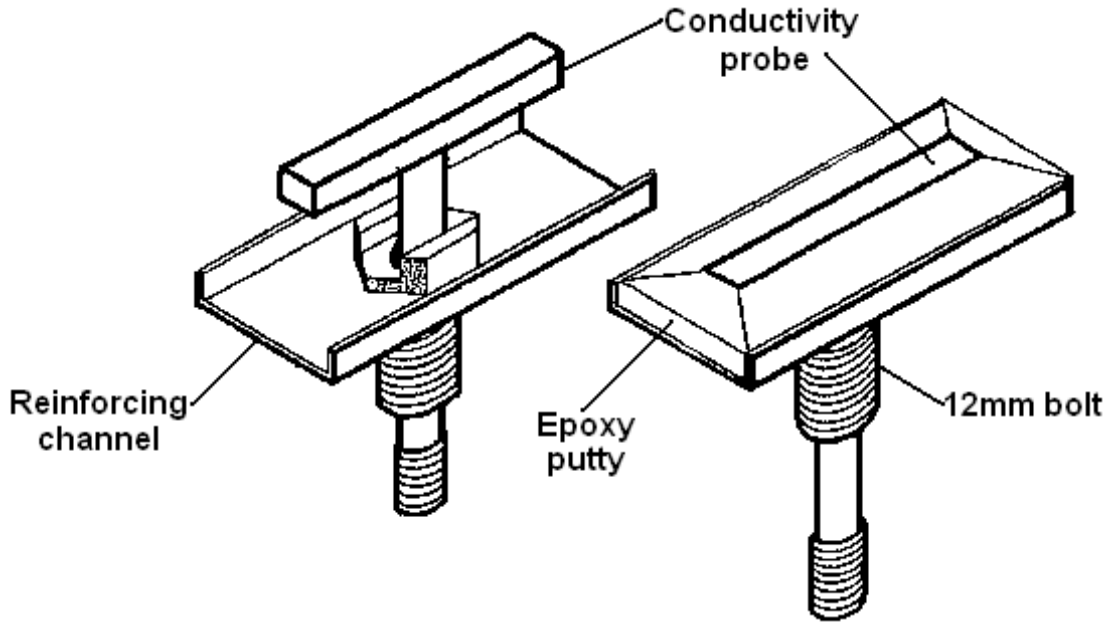


Figure 2.4: Assembly diagram for the conductivity probe

For a ball only load, sharp changes were detected by the conductivity probe at the toe and shoulder of the load. In the case of an autogenous load, the rate of change in signal at the shoulder is governed by the rate at which slurry drains of the probe and the slurry viscosity.

At the University of the Witwatersrand a comprehensive study using conductivity probes brought about an understanding of how the behaviour of autogenous loads are affected by the slurry rheology, mill speed and the load volume in a pilot mill (Smit, 2000). Furthermore, this technique has been used in an industrial mill and conditions such as overloading, premature centrifuging, off the grind and excessive slip were easily detected by the conductivity probe (Moys, Van Nierop and Smit, 1996). In this study premature centrifuging in the industrial mill occurred at the feed end rather than the discharge end where it was expected that a higher slurry percents solid would give rise to a high slurry viscosity. Not only has this technique been used to measure load behaviour in ball or AG/SAG mills but also in a HICOM nutating mill (Nesbit and Moys, 1998).

The conductivity measurement technique has not yet been developed into a tool for mill control though it has proven itself in being able to provide useful information that improves the understanding of load behaviour in a mill. Measurements from the conductivity probe have been used to improve mill power modelling capabilities which will lead to improved mill control strategies and design (Van Nierop and Moys, 2001).

2.1.3 Vibrations Measurement Technique

Intense mechanical vibrations occur on the mill surface and machine components attached to the mill mainly due to collision events occurring

within a mill. The flexing of the mill shell and other external vibration sources such as the drive motor, girth gear and surroundings also contribute to mill vibrations. These later contributing factors are normally assumed to be randomly distributed and give a constant contribution to the mill vibrations. Thus process variables will mainly affect the occurrence of collision events in the mill likewise the intensity of the vibrations. These vibrations avail a good opportunity of discerning the mill condition as affected by operating parameters through the use of accelerometers. An accelerometer is an electromagnetic device that measures static or dynamic acceleration forces. Accelerometers can either use the piezoelectric effect or changes in capacitance to obtain an output signal that varies with the intensity of the vibrations. Accelerometers can either be attached on the mill shell or assemblies associated with the mill.

Similar to the acoustic emission technique, the vibration signal obtained in time domain offers little information related to the condition of the charge. It then becomes necessary to convert the signal into its frequency domain. Vermeulen et al (1984) made use of piezoelectric sensors to measure mill vibrations. Their novel technique of placing the sensor into a liner bolt proved that physical information from within a mill could be continuously obtained. Studies on laboratory scale (Zeng and Forssberg, 1992) and industrial scale mills (Zeng and Forssberg, 1993) using accelerometers mounted on bearings (i.e. the pinion bearing for the industrial mill) revealed that the mill speed, powder filling, pulp density, pulp temperature

and batch-wise grind time can be strongly correlated with a few frequency bands in the power spectra. Similarly, Behera, Mishra and Murty (2007) have made the use of accelerometers mounted on a bearing in a pilot mill. Their signal processing method uses the amplitude of the dominant peak obtained from a FFT spectrum and simply relates this to various mill variables.

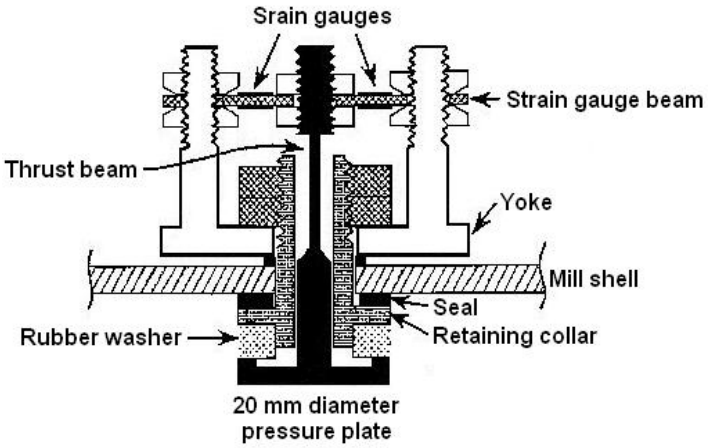
CSIRO (Commonwealth Scientific and Industrial Research Organisation – Australia) patented the technique of using accelerometers fixed on the moving surface of a mill to measure vibrations on industrial mills (Campbell et al, 2003). In the various tests conducted on pilot and industrial scale mills, they were able to calculate the toe and shoulder positions of the load and compare them with actual photos of the load. Important outputs from the system can also be used as soft sensors for mill load and charge size though they are mill specific.

An interesting approach in this technique was the use of two accelerometers mounted 180^{o} apart on a mill shell coupled with the use of a dynamic neural network (Gugel et al, 2003). The neural network acts as a non linear classifier such that the current spectral signatures along with other key parameters are used to output a fill level measurement for the mill. The lack of proper training of the neural network to the various vibration signatures as process variable are manipulated can lead to a wrong output of the mill fill level.

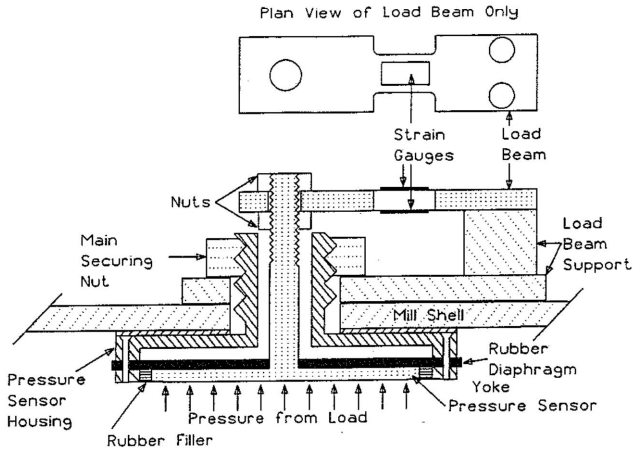
The challenge in this technique of load behaviour measurement lies in the method that one uses to relate the frequency domain signal to the conditions prevailing in the mill. The technique still holds much promise for further research and industrial use.

2.1.4 Movement, Pressure or Force Measurement Technique

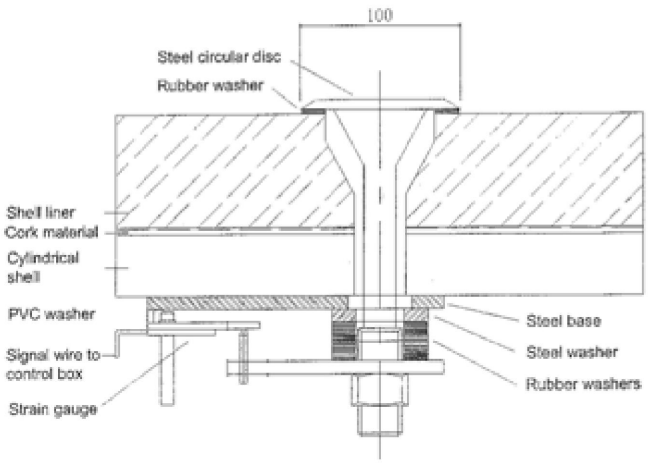
The forces exerted by the load on the liners can be resolved into transverse and tangential forces. In order to measure the forces independently the probe has to be designed such that it is able to resolve the forces. Typically the probes will have a portion that is resident in the mill (i.e. pressure plate, force plate or mill liner) so as to have a direct contact with the load. The forces exerted by the load will be transmitted via a thrust beam which is connected to a load beam. Mounted on the load beam are strain gauges that are configured as a Wheatstone bridge and connected to the appropriate circuits to provide the required output signal. The movement probe will measure the resultant forces of the load on the liners as the probe is not designed to measure the transverse or tangential forces independently. The pressure or force probe both measure the transverse forces exerted by the load on the liner. The value of this measurement technique is that not only does it measure the load behaviour it also gives a quantitative account of the forces exerted by the load on a liner (Skorupa & Moys, 1993). These forces have a direct and quantifiable effect on the wear mechanism and power drawn by mills.



a) Section through a pressure probe for a pilot mill

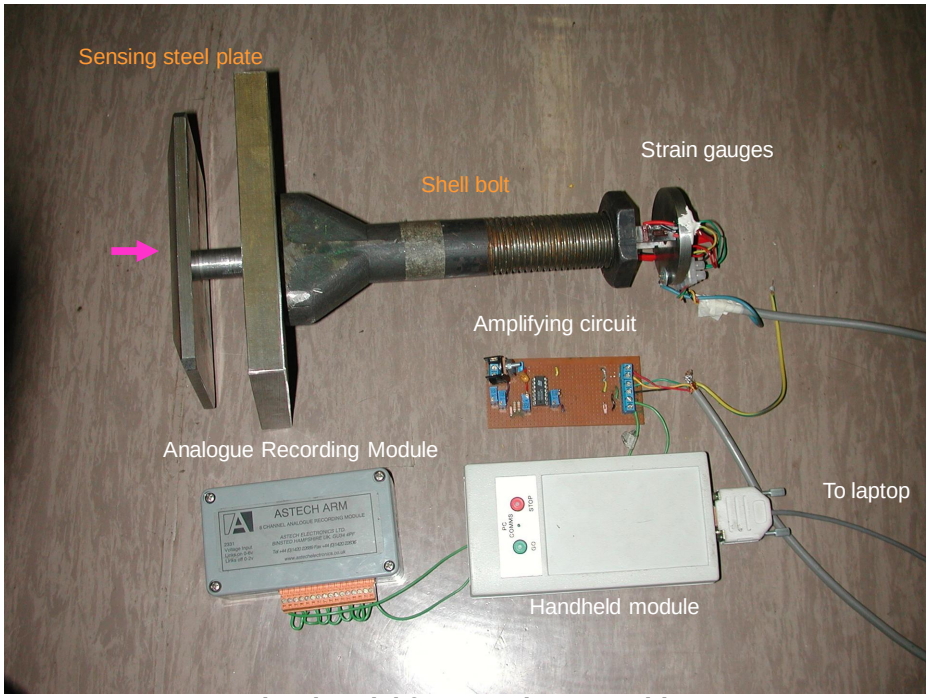


b) Section through a improved variant of the pressure probe for a pilot mill



c) Section through a movement probe to be installed in an industrial mill

Figure 2.5: Illustrations of movement and pressure probes



a) Industrial force probe assembly



b) Probe head designs **c) Load beam**

Figure 2.6: Force probe installed in an industrial mill

For load behaviour measurements the pressure probe exhibits a rapidly rising response in its signal when it goes under the toe of the load but has a poorly defined response for the shoulder position. This makes the probe quite accurate and reliable in measuring the toe's angular position.

Various designs of these probes can be seen in Fig. 2.5 & 2.6. Wits University has dedicated a lot of time and resources in the improvement of the pressure probe. One of the first designs of the pressure probe, which was installed in a pilot mill, can be seen in Fig. 2.5a with subsequent improvements leading to a new design to be used in wet mill is seen in Fig. 2.5b. A force probe prototype for installation in industrial mills as seen in Fig. 2.6 has been developed and tested in a coal mill of diameter 4.74m and length 7.4m. Two different pressure plates (i.e. circular and square) were tested (Fig. 2.6b). The thrust beam runs though a liner bolt and is connected to the load beam (Fig. 2.6c) that seats outside the mill.

Tano et al (2005), reported of the development of a probe that is influenced by the grinding charge motion and has the ability to collect relevant information and used it for process control. The probe uses strain gauges mounted inside rubber lifters. The sensor picks up the deflection of the lifter when it moves through the grinding charge with a resolution of 1^{o}. Clear correlations between the signal profile and different charge properties such as load volume, angle of repose and charge position exist (Tano et al., 2005; Dupont and Vien, 2001b). The sensor has been developed and integrated into a complete measurement system (Dupont and Vien, 2001a) and was marketed by Metso minerals under the name of Continuous Charge Measurement (CCM) sensor.

The force measurement technique has also been applied to a Hicom nutating mill using the tri-axial force sensor in Fig. 2.7 (Nesbit & Moys, 1998). The tri-axial force sensor measures the normal, tangential and axial forces exerted by the load. Here the tri-axial force probe brought about an understanding of the behaviour ball mass in the nutating mill.

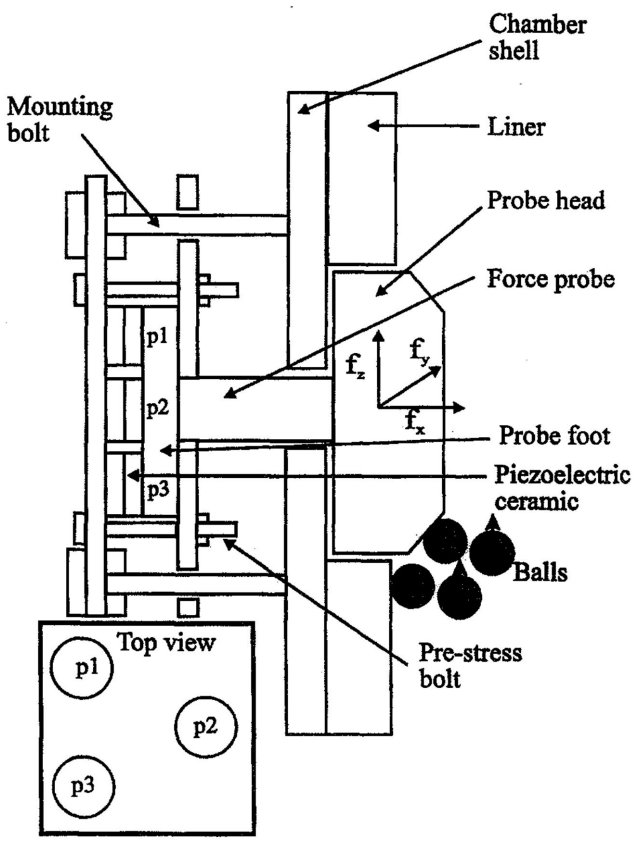


Figure 2.7: Tri-axial force sensor installed in a Hicom nutating mill

2.1.5 X-ray Measurement Technique

This is a novel method developed at the University of Cape Town by Powell and Nurick (1996a) that tracks the motion of balls deep within the charge. Unlike other techniques that can either measure the balls at the

periphery of the load or only the balls apparent at the end window of a mill with this technique a more realistic and useful picture of the charge motion can be obtained.

In order to overcome the challenges of viewing motion of balls deep within the charge a bi-planar angioscope was used to film the ball motion using an experimental Perspex mill. The bi-planar angioscope uses high energy X-rays emitted in short pulses to stimulate a scintillating screen which are then detected by a TV camera and relayed to an external monitor. Permanent records are filmed in two planes simultaneously with cine cameras resulting in a film of excellent resolution. Plastic beads were used to make up the ball load with 4 opaque balls used for tracking. To track rotation of a ball, one of the beads was fitted with a lead rod. The study revealed several phenomena such as non-rotation of balls, charge dilation that increases with mill speed, longitudinal migration of balls, insight into charge segregation, spiralling action of balls and the smooth paths of balls in the bulk of the charge. This technique can only be used for research purposes and can be quite useful in obtaining experimental data that can be used to verify the DEM model so that confidence can be given to its predictive capabilities. Govender et al (2002) reported on an automated 3D mapping and space parameterisation technique of the images obtained. Subsequently the accuracy has been further enhanced to be able to track balls within 0.15mm (Govender et al, 2004).

2.2 MODELS FOR MILL POWER

In milling, a feed of a known weight size distribution is to be milled to a product of a finer weight size distribution at a desired rate of production. The specification of the product size depends on the liberation characteristics of the ore and the size requirements for optimal operations of the downstream process. It is important to know the power requirements to effect this size reduction and the corresponding size of the mill that would carry out the duty. A commonly used method is to conduct grindability tests (i.e. Bond's Method) in a laboratory scale mill so as to obtain the specific energy required to effect the required size reduction and hence the industrial mill power can eventually be obtained. Various power models and factors based on past experiences are then used to calculate the overall size of the industrial mill. Another method is to use the rates of breakage of a specific ore type or combination of ore types for a known mill operating condition to determine the internal dimensions of the mill. The power requirements for driving the mill are then obtained from the internal dimensions by using a power model. This method accounts for the breakage action in each size class and tracks the sizes and corresponding masses through the mill. The method is appropriate for both mill design and optimisation.

In the above methods for sizing mills it is important to have a good model to either determine the power requirements of the industrial mill or to

calculate the mill's internal dimensions. Traditionally there have been two major approaches used to develop mill power models. These are the empirical approach (Rose & Sullivan, 1958; Bond, 1961b; Fuerstenau et al, 1990; Moys, 1993 and Morrell, 1993) and the theoretical physics based approach (White, 1905 and Mishra & Rajamani, 1992). The review of power models will focus on the uniqueness of the load behaviour models used by various researchers to develop their power models. It does not serve as an exhaustive list of all power models proposed in literature.

2.2.1 Empirical Mill Power Models

The empirical approach approximates the shape of the load to be a segment of a circle inclined a certain angle to the centre of the mill and treats the load as a solid body (Fig. 2.8). In this case, the turning moment of the frictional force balances the turning moment of the centre of gravity of the bed around the mill's centre. This method only accounts for the energy required to raise the balls from the toe to the shoulder against gravity. This approach does not account of energy recovered by the mill shell due to cataracting balls striking it and also does not account for internal friction of the load due to balls sliding over each other. The torque-arm method calculates the mill's torque (**T**) and power (**P**) using the following models:

$$T = mgr_c \sin\alpha \qquad \textbf{2.1}$$

$$P = \frac{2\pi NT}{60} \quad \textbf{2.2}$$

Where **m** is the mass of the load, **g** is the acceleration due to gravity; $\mathbf{r_c}$ is the radial distance from the centre of the mill to the centre of gravity, α is the angle of repose and **N** is the mill's speed in rpm.

The general form for the empirical power models based on the torque-arm approach is:

$$P = f_p(\rho_L) f_\alpha(\alpha) f_J(J) f_L(L) f_D(D) f_N(N) \quad \textbf{2.3}$$

Where ρ_L is the load density, α is the angle of repose, **J** is the load filling, **L** is the mill's length, **D** is the mill's diameter and **N** is the mill's speed.

In literature the diameter of the mill in power models is normally varies exponentially with power and the exponent normally varies from 2.3 to 2.5. The model assumes that the mill power is directly proportional to the mill's length and that the end walls of the mill have a negligible effect upon the mill's power. Further, it assumes that the tumbling action of the mill is independent of the size of the mill provided that the ball diameter is much less than the mill's diameter.

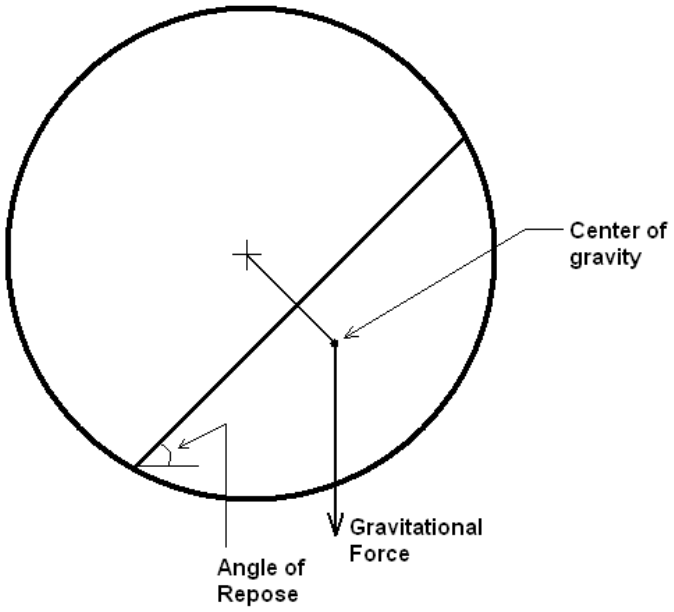


Figure 2.8: Illustration of the torque-arm load shape

An interesting alternative in describing the load shape for empirical power models is the C-model proposed by Morrell (1993) and its variant the D-model.

2.2.1.1 Rose and Sullivan's Power Model

Rose and Sullivan (1958) used the functional relations between dimensionless groups, as seen in equation 2.4, to obtain a mill power model for determining the net mill power for dry grinding as seen in equation 2.5. The relationships between the various dimensionless groups were obtained through experiments as dimensional analysis alone cannot give a form of the relationships for these groups. In equation 2.4 the functions enclosed in the first square brackets relate to the mill and ball

load system while those in the second set of brackets relate to the characteristics of the powder.

$$\frac{P}{D^5N^3\rho} = \left[\left(\frac{L}{D}\right) \times \emptyset_1'\left(\frac{N_c}{N}\right) \times \emptyset_3(J) \times \emptyset_4\left(\frac{D}{d}\right) \times \emptyset_5(n) \times \emptyset_6\left(\frac{h}{D}\right)\right] \times \left[\emptyset_9\left(\frac{D}{b}\right) \times \emptyset_{10}\left(\frac{\sigma}{\rho}\right) \times \emptyset_{11}(V) \times \emptyset_{12}\left(\frac{H}{D^6N^2\rho^2}\right) \times \emptyset_{13}(f)\right] \quad \textbf{2.4}$$

$$P_{net} = K(LD^{2.5}\rho_b)(\emptyset_c)\left(1 + \frac{0.4\sigma U}{\rho_b}\right)F(J) \quad \textbf{2.5}$$

For equation 2.5, it is assumed that the mill's net power is proportional to the mill speed up to 80% of the critical beyond this the model cannot be used. The term (1+ $0.4\sigma U/\rho_b$) is a correction factor for the power to take into account the powder tumbling with the balls. Here it is assumed the powder occupied the void spaces between the balls at a certain particle filling (U) and that the power is proportional to the weight of the balls plus the powder. This correction factor holds for cases where the ratio of the mill's diameter to the particle diameter is less than about 400 or if the particles are so small that segregation occurs. The empirically determined function F(J) accounts for the effect of ball filling on the power. Rose and Sullivan (1958) proposed the following parabolic function in equation 2.6 for ball fillings less than 50%.

$$F(J) = 3.045J + 4.55J^2 - 20.4J^3 + 12.9J^4 \quad \textbf{2.6}$$

The function was obtained by measuring the power drawn by a small laboratory mill at known ball fillings. This function causes the maximum net power drawn by a mill to occur at a ball filling of 40%.

2.2.1.2 Bond's Power Model

Bond's (1961b) model which is the most widely accepted model was obtained empirically by collating data from mills of various designs. Equation 2.7 gives the power draw (**P**) for conventional ball mills using make-up balls larger than one-eightieth of the mill's diameter.

$$P = K_1 \rho_L \sin(\alpha)\, J(1 - \beta J) L D^{2.3} N_c \left(1 - \frac{0.1}{2^{(\gamma - \zeta N_c)}}\right) \qquad \textbf{2.7}$$

Where $\mathbf{K_1}$ is a constant strongly affected by liner design and slurry properties, ρ_L is the bulk density of the load, α is the dynamic angle of repose of the load, **J** is the ball filling fraction, **L** is the mill's length, D is the mill's diameter and $\mathbf{N_c}$ is the mill speed expressed as a percentage of the critical mill speed. B is a factor which is normally given the value of 0.937 and implies that the maximum power drawn by the mill would occur at a ball filling of about 53%. The last factor in brackets accounts for the effect of mill speed when close to the critical speed on the power drawn by the mill. The parameters γ and ζ normally have the value of 9 and 0.1 respectively. Bond's model as seen in equation 2.7 treats all the variables separately thus for example it does not allow for the fact that variations in

the ball filling (J) affect the nature of the dependence of the mill's power draw on the mill's speed.

2.2.1.3 Fuerstenau, Kapur and Velamakanni's Power Model

Fuerstenau et al (1990) studied the effects of polymeric grinding aids on the grinding of dense slurries by changing the ball size, media charge, mill's speed and slurry holdup. Grinding in the presence of dense slurries tends to cause the ball media to adhere to the mill wall and experience an increase in cataracting or the balls are completely centrifuged. The addition of polymeric dispersants tends to keep the load fluid and thus the normal cascade – cataract behaviour dominates. To be able to describe the effect of addition and non addition of polymeric dispersants on the power in a ball mill a model which describes the load behaviour for both cases had to be proposed.

The load shape model seen in Figure 2.9 attempts to describe the dynamics (i.e. both cascading and cataracting) as well as a variable partition of the charge between the two regimes as the pulp viscosity changes with time. In this load behaviour model it is assumed that the cataracting mass sticks uniformly on the mill shell and is lifted up before dropping down on the cascading mass.

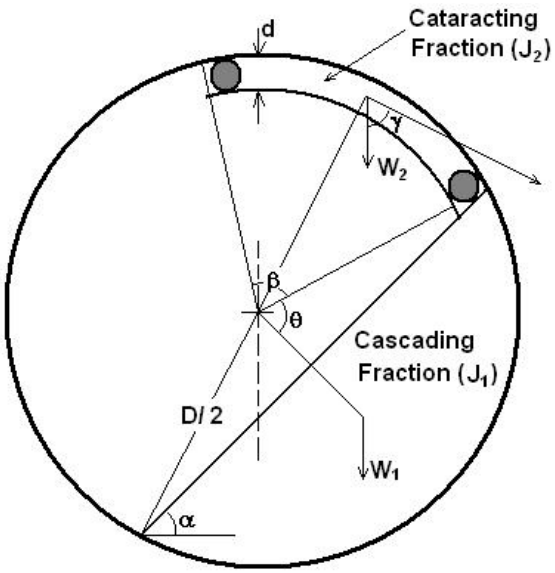


Figure 2.9: Illustration of Fuerstenau et al simplified load shape

In drawing up the power model Fuerstenau et al (1990) considered the power required by a mill to be the sum of the power drawn by the cascading load (**P_{cs}**), the power drawn by the cataracting load (**P_{ct}**) and power due to a minor frictional component (**P_f**). The equations below give a mathematical description of these power components:

Power drawn by cascading load (P_{cs}):

The cascading power can be drawn from any existing model. Fuerstenau et al (1990) used the Hogg and Fuerstenau (1973) power model to estimate the power drawn by the cascading charge.

$$P_{CS} = \frac{2NWg(D-d)}{3J} \emptyset(J_1) \sin\alpha \qquad \textbf{2.8}$$

The function ϕ depends on the filling of the cascading fraction of the load ($\mathbf{J_1}$) in the following manner:

$$\emptyset(J_1) = \begin{cases} 4J_1(1-J_1), & 0.35 \leq J_1 < 0.5 \\ 4J_1(1.05-1.33J_1), & 0.2 \leq J_1 < 0.35 \end{cases} \quad \textbf{2.9}$$

Where: **N** is the mill's rotational rate (rpm), **D** is the mill's internal diameter, **W** is the mass of grinding charge, **g** is the acceleration due to gravity, $\mathbf{J_1}$ is the ball filling of the cascading charge and α is the angle of repose of the load.

Power drawn by the cataracting load (P_{ct}):

The power of the cataracting mass is estimated from the arced portion of the load on the mill's inner surface above the cascading load as illustrated in Fig 2.7.

$$P_{Ct} = \pi N g (D-d) W_2 \sin\left(\alpha + \theta + \frac{\beta}{2}\right) \quad \textbf{2.10}$$

$$W_2 = \frac{\pi}{4} s D^2 L J \rho \quad \textbf{2.11}$$

$$s = Z\left(1 - e^{[-X(t-t_0)]}\right) \quad \textbf{2.12}$$

Where: **d** is the ball diameter, $\mathbf{W_2}$ is the mass of cataracting charge, **J** is the total mill filling, **L** is the mill's length, **ρ** is the load density, **s** is a time dependent parameter that is a function of the slurry viscosity, **X** is a function of the mill material system and is affected by addition of polymeric dispersants and **Z** is a lumped parameter.

Power drawn by the minor frictional component (P_f):

This small power component is due to friction in the charge, its dilation, slippage, de-mixing and percolation of particles in the voids between the balls.

$$P_f = Ce^{-Kt} \qquad \textbf{2.13}$$

Where: **C** and **K** are constants.

Thus the power model can track the mills power draw as a function of changing pulp viscosity with time, it permits estimations of the charge split between the cascading and cataracting-centrifuging regimes of load behaviour and also explains the occurrence of a peak torque value as the slurry viscosity increases.

2.2.1.4 Moys Power Model

Moys (1993) developed a semi phenomenological power model based on the understanding of the mill load behaviour. The load behaviour model,

as seen in Fig. 2.10, is a compromise of the two extremes of load behaviour that is a cascading load to cater for power draws at low speeds and a centrifuging load component is introduced that caters for the observed power loss as mill speeds increases. This simplification of the mill load behaviour does not include the cataracting portion of the charge but can account for the loss in power through cataracting balls striking the exposed mill shell through its centrifuging load component. As a result this model cannot give an indication of the fraction of load that is cataracting, the onset of centrifuging or the thickness of the centrifuged layer.

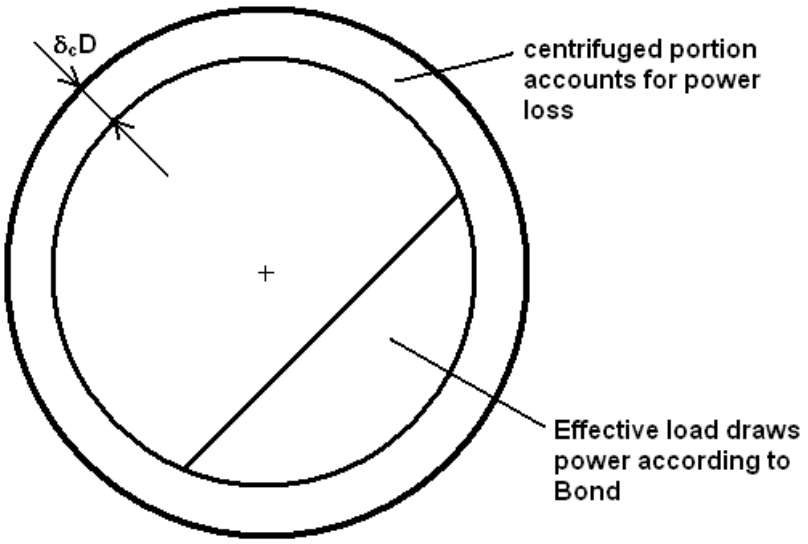


Figure 2.10: Illustration of Moys simplified charge shape

Moys assumed that the power drawn by the active portion of the charge was adequately described by Bond's model and dropped out the term that models the power as mill speeds nears 100% of the critical. When substantial cataracting occurs coupled with a loss in power the centrifuged

load model is activated and a portion of the load is assumed to be centrifuged. This leads to a reduction in the mill's effective diameter, mill speed and likewise a reduction in the active load mass.

Thus the power model for a reduced active charge is given by:

$$P = KD_{eff}^{2.3} \sin\alpha\, \rho_L J_{eff}\left(1 - \beta J_{eff}\right) N_{eff} L \qquad \textbf{2.14}$$

The effective diameter of the mill (**D_{eff}**) is given by:

$$D_{eff} = (1 - 2\delta_c)D \qquad \textbf{2.15}$$

Here it is assumed that the thickness of the centrifuged layer is $\boldsymbol{\delta_c D}$.

The effective mill filling (**J_{eff}**) is given by:

$$J_{eff} = \begin{cases} \frac{J - 4\delta_c(1-\delta_c)}{(1-2\delta_c)^2}, & \delta_c < 0.5[1 - (1-J)^{0.5}] \\ 0, & \delta_c \geq 0.5[1 - (1-J)^{0.5}] \end{cases} \qquad \textbf{2.16}$$

A simplification of equation 2.16 was proposed by Moys and its suitability assessed. The simplification is:

$$J_{eff} = \begin{cases} J - 2\delta_c, & \delta_c < J/2 \\ 0, & \delta_c \geq J/2 \end{cases} \qquad \textbf{2.17}$$

A model that relates the thickness of the centrifuged layer to the mill's operating variables is seen in equation 2.18.

$$\delta_c = J^{\Delta_J} e^{\left[-\frac{N^* - N}{\Delta_N}\right]} \qquad \textbf{2.18}$$

Where $\mathbf{N^*}$ and $\mathbf{\Delta_N}$ are parameters that are strong functions of liner profile and slurry viscosity and $\mathbf{\Delta_J}$ is a parameter that governs the strength of the dependency of $\boldsymbol{\delta_c}$ on the load filling **J** and will be a strong function of liner profile.

For low mill speeds it is expected that no power loss will occur thus no centrifuging (δ_c = 0). As the speed is increased a drop in power begins due to cataracting and at higher speed due to centrifuging this will correspond with a rapid increase in δ_c. This phenomenon is reflected in the exponential dependency of the mill's speed (**N**) on $\boldsymbol{\delta_c}$. For a low mill filling, minimal cataracting will be experienced if the liner allows substantial slip and thus it is expected that δ_c = 0 but as the mill filling is increased and slip reduced $\boldsymbol{\delta_c}$ will become significant. If the liner does not allow for slip then $\boldsymbol{\delta_c}$ becomes independent of the load filling (**J**).

This proposed model does reflect the complex interactions of load volume and speed on the power drawn by the mill. Certainly it could be quite useful in determining the mill power drawn by South African style run-of-

mine (ROM) mills as they are operated at high speeds at which liner profile and slurry rheology have significant effects on the load behaviour. These mills suffer from viscous slurry causing the grinding media to stick on the liners causing premature centrifuging. Van Nierop and Moys (2001) used a modified version of the Moys model to model an industrial AG mill's power after having insight into the nature of the load behaviour using conductivity probes. The model could track the AG mill's power quite well.

2.2.1.5 Morrell's Power Model

Through a photographic study of the evolving shape of a mill's charge as mill speed and charge filling increased for three liner profiles Morrell proposed a new description of the charges shape as seen in Figure 2.11. The crescent like shape was obtained through considering the portion of the charge that exerts a force on the mill shell. The rest of the charge was ignored by assuming that the cataracting portion has no direct effect on the mill and that the eye of the load is stationary and of relatively small mass thus having a negligible effect on the mill's power draw. The simplified charge description below was used to derive Morrell's C power model. The physical limits of the charge were defined by radial lines that extend from the toe (θ_T) and shoulder (θ_{Sh}) to the mill's centre, the charge inner surface radius (r_i) and the mill's internal radius (r_m). The physical limitations of the charge had to be defined mathematically through analysing the photographs of the load behaviour so that they would be incorporated in the power model.

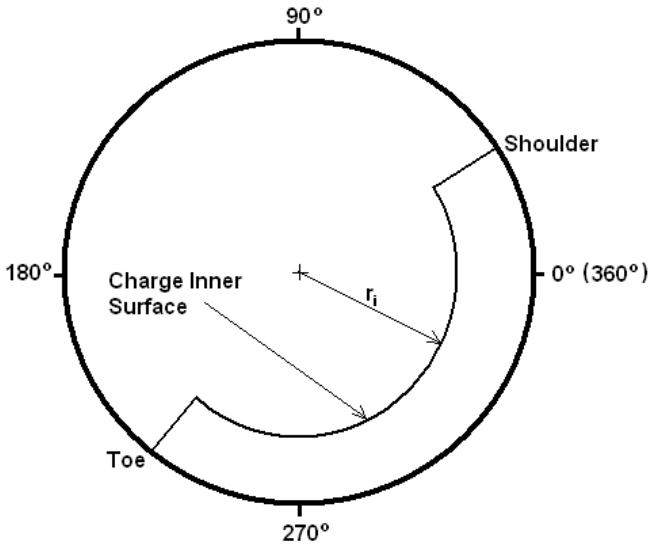


Figure 2.11: Illustration of Morrell's simplified charge shape

The mathematical descriptions are of the form:

Toe's angular position (θ_T):

$$\theta_T = A\left(1 - e^{-B(\emptyset_c - \emptyset)}\right) + \frac{\pi}{2} \qquad \textbf{2.19}$$

Where **A** and **B** are parameters determined by regression analysis, ϕ_c is the experimentally determined critical speed and ϕ is the mill's fraction of critical speed.

Shoulder's angular position (θ_S):

$$\theta_S = \frac{\pi}{2} - \left(\theta_T - \frac{\pi}{2}\right)(E + FJ_t) \qquad \textbf{2.20}$$

Where **E** and **F** are parameters determined by regression analysis, θ_T is the shoulders angular position in radians and J_t is the mill filling.

Charge inner surface (r_i):

$$r_i = r_m \left[1 - \left(\frac{2\pi\beta J_t}{2\pi+\theta_{Sh}-\theta_T}\right)\right]^{0.5} \quad \textbf{2.21}$$

Where r_m is the mills internal radius and β is an empirical model that is defined as the fraction of charge bound by the toe, shoulder and charge inner surface. It is assumed that β was related to the time it takes for a particle to move between the toe and shoulder within the charge and between the shoulder and toe when in free flight.

Morrell derived his power model, seen in equation 2.22, using an energy balance approach. The model considers the rate at which potential and kinetic energy are generated within the charge.

$$P_{net} = \left[\frac{\pi g L \rho_c N_m r_m}{3(r_m - z r_i)}\{2r_m^3 - 3z r_m^2 r_i + r_i^3(3z-2)\}\{\sin\theta_S - \sin\theta_T\}\right] + \left[L\rho_c\left\{\frac{N_m r_m \pi}{(r_m - z r_i)}\right\}^3\{(r_m - z r_i)^4 - r_i^4(z-1)^4\}\right] \quad \textbf{2.22}$$

Where: $z = (1 - J_t)^{0.4532}$

In its current form the model can only account for the power drawn by the belly length of a mill and can be used only for grate discharge mills. To use the model to approximate a wide range of industrial mill powers, Morrell

further modified the model to account for power losses due to the presence of a slurry pool in an overflow mill (equation 2.23) and the power drawn by the charge in the conical ends of a mill (equation 2.24) and the no load power (equation 2.25).

Net Power for the cylindrical section of an Overflow mill:

$$P_{net} = \left[\frac{\pi g L \rho_c N_m r_m}{3(r_m - z r_i)}\{2r_m^3 - 3z r_m^2 r_i + r_i^3(3z-2)\}\{\sin\theta_S - \sin\theta_T\}\right] + \rho_P(\sin\theta_T - \sin\theta_{TO}) + \left[L\rho_c\left\{\frac{N_m r_m \pi}{(r_m - z r_i)}\right\}^3\{(r_m - z r_i)^4 - r_i^4(z-1)^4\}\right] \quad \textbf{2.23}$$

Where: $\boldsymbol{z} = (1 - J_t)^{0.4532}$

Net power for an overflow mill with cone ends (P_C):

$$P_C = \left[\frac{\pi g L_d \rho_c N_m}{3(r_m - r_t)}\{r_m^4 - 4r_m r_i^3 + 3r_i^4\}\{\sin\theta_S - \sin\theta_T\}\right] + \rho_P(\sin\theta_T - \sin\theta_{TO}) + \left[\frac{2\pi^3 N_m^3 L_d \rho_c}{5(r_m - r_t)}\right](r_m^5 - 5r_m r_i^4 + 4r_i^5) \quad \textbf{2.24}$$

No load power (P_{NL}):

$$P_{NL} = 2.62(D^{2.5} L \emptyset)^{0.804} \quad \textbf{2.25}$$

Where $\boldsymbol{\rho_c}$ is the density of the charge, $\mathbf{N_m}$ is the mills speed in rpm, $\mathbf{r_m}$ is the mill's internal radius, $\mathbf{r_i}$ is the radial distance from the mill's centre to

the charge inner surface, $\mathbf{r_t}$ is radius of the trunnion and $\mathbf{L_d}$ is the length of the conical end.

The C-model was applied to a database of 76 mills (38 ball mills, 28 SAG mills and 7 AG mills) of various sizes and a wide range of power draws so as to find the accuracy of its predictions. The C-model provided predictions with a relative precision of 10.6% at the 95% confidence interval. Despite the accuracies of this model one drawback for its application is the complexity of the model and the number of empirical equations that are required. Knowledge of the model form and its implementation has to be sought in Morrell's well documented thesis. Morrell's model has further been developed to a discrete shell model (D-Model) that is even more complex than the C-model. The D-model attempts to approximate the charge more realistically by sectioning the C-model into discrete shells so as to represent the distinct layers present in the charge. Morrell chooses the width of each of these discrete shells to be approximated by the average particle size of the load. The physical boundaries of the D-model are defined by equation 2.19, 2.20 and 2.21. The model has surely built its reputation as a good model to predict industrial SAG/AG mill power draws.

2.2.2 Mechanistic Mill Power Models

Through the empirical load behaviour models illustrated in section 2.2.1 that are used to develop various power models it can be seen that they are a gross simplifications of the actual load behaviour. Despite the models

being easy to use they describe the load's shape as a solid body thus not reflecting the actual discrete nature of the load. The load behaviour models fail to account for the recovery of energy by balls cataracting on to the exposed mill shell thus they cannot be used as a diagnostic tool to assess or optimise the ball or rock trajectories. The load behaviour models are not capable of incorporating the effects of mill internals design (i.e. lifter design, number of lifters, steel or rubber liners etc) on the load behaviour. The importance of having a model that would treat the load as discrete particles was realised quite early (White, 1905; Davis, 1919). Furthermore models developed by McIvor (1983) and Powell (1991) try to describe the influence liner profiles have on a single ball in the outermost trajectory that is in contact with a liner.

2.2.2.1 The Discrete Element Method (DEM)

The Discrete Element Method (DEM) was developed and applied to granular material by Cundall and Strack (1979). The application of this technique to studying the load behaviour in ball mills was done by Mishra and Rajamani (1992) and has been a great benefit in the design and optimisation of grinding mills.

The Discrete Element Method is a way of modelling the motions and interactions of a set of individual particles and their environment as affected by gravity, models for particle interaction and Newton's laws of motion. Collisions between particles are cleverly modelled by using the

contact force law that consist of the linear spring, dashpot and slider as seen in Figure 2.12.

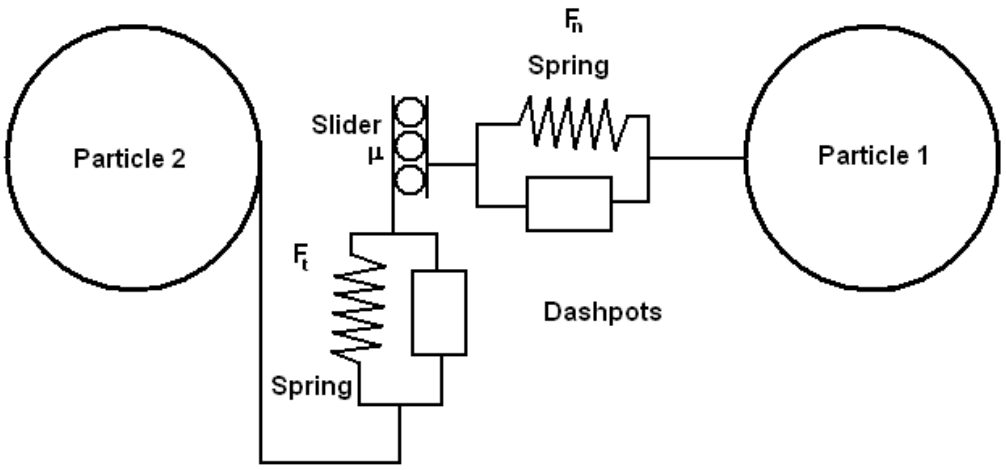


Figure 2.12: Spring-slider-dashpot model for interactions between two particles

The normal force is given by:

$$F_n = -k_n \Delta x + C_n V_n \qquad \textbf{2.26}$$

The tangential force is given by:

$$F_t = min\{\mu F_n,\ k_t \int V_t dt + C_t V_t\} \qquad \textbf{2.27}$$

The particles are allowed to overlap by small amount (**Δx**) typically between 0.1- 0.5%. The normal ($\mathbf{V_n}$) and tangential ($\mathbf{V_t}$) relative velocities determine the collision force by using the contact force law. The normal

force has a linear spring that provides the repulsive force and dashpot to dissipate a portion of the kinetic energy. The maximum overlap between the particles is determined by the stiffness ($\mathbf{k_n}$) of the spring in the normal direction. The normal damping coefficient ($\mathbf{C_n}$) is chosen to give the required coefficient of restitution (ε). The tangential force ($\mathbf{F_t}$) model has an integral term that represents an incremental spring that stores energy from the relative motion of the particles and the elastic tangential deformation of the contacting surface. The dashpot in the tangential force model dissipates energy from the tangential motion and models the tangential plastic deformation of the contact. The force is limited by the coulomb frictional limit $\mu\mathbf{F_n}$ at which the surface contact shears and the particle begins to slide over each other. The structure of the DEM model can further be coupled with Discrete Grain Breakage models (DGB), Computational Fluid Dynamic (CFD), Smoothed Particle Hydrodynamics (SPH) and Multi-Phase Flow models (MPF). Discrete Grain Breakage models are used to define the breakage of particles in a comminution device. Computational Fluid Dynamic models are used to compute the fluid phase flow, interactions and transport within equipment. Smoothed Particle Hydrodynamics is used to model non-Newtonian fluids such as slurry as an assemblage of pseudo-particles with interactions related to shear at any point in the slurry and provides a link between fluid transport and fine particles in the slurry. Multi-Phase Flow models are used to model particle and gaseous phases contained within the fluid.

To account for the arbitrary particle shapes, sizes and density distributions that are encountered in the mineral processing industry super-quadrics can be used to define the particle.

The super-quadrics 3D geometric shapes are defined by the equation:

$$\left(\frac{X}{A}\right)^n + \left(\frac{Y}{B}\right)^n + \left(\frac{Z}{C}\right)^n = S^n \qquad \textbf{2.28}$$

Where: **A**, **B** and **C** represents the aspect ratio of the shape in its various axes, **S** is the semi major axis of the shape and the power **n** determines the angularity of the grinding media shape

The DEM requires intensive computing power especially when many particles are involved and the level of complexity of the system being modelled is high. The time required in simulating a full mill with balls, rocks, slurry transport, rock breakage etc would take a couple of weeks on a super computer or several months on a top of the range Pentium or AMD desktop. Despite this the DEM is quite a versatile tool and has been used to quantitatively predict the load behaviour (2D and 3D) in mills, predictions of collision forces, energy spectra and power consumption (Mishra and Rajamani, 1992 and Cleary, 1998); liner wear and its effect on load behaviour (Kalala et al, 2007; Cleary, 1998 and Qui, 2001); Particle breakage, grinding rates, liberation, and mill throughput (Cleary, 2001;

Bwalya and Moys, 2003; and Potapov et al, 2007). Various mineral processing equipment have been simulated with the intention of optimising throughput through the equipment or just understanding the equipment better. For this technique it is absolutely important to verify and test the model against experimental results and not to perceive the simulation results as reality. The lack of good experimental data for testing and verifying DEM codes further limits the accuracy of the DEM predictions.

2.3 CONCLUSION

The basic purpose of milling of ores remains as a method of imparting sufficient energy onto a rock to subsequently cause damage or breakage of particles to some specified size distribution so as to expose the valuable mineral for further downstream processes. Several measurement techniques exist that are capable of measuring the extent of liberation from a breakage action such as optical image analysers, scanning electron microscopy analysers and x-ray micro-tomography analysers and have improved in speed, accuracy and quality of information that one can obtain. Depending on the mill's operating conditions; a mill can contain a wide range of breakage actions such as impact, chipping and abrasion. Establishing the mode(s) of breakage that would lead to the optimum damage and subsequent breakage of particles is the key in obtaining the most efficient way of energy utilisation in any mill. Optimising the load behaviour to target the mode of breakage required would be most

important. Subsequently these broken particles need to be transported out of the mill through a discharge mechanism with water or air acting as the conveying agent. The discharge mechanism should also be designed in such a way that it would encourage the exit of these particles out of the mill. Discrete Element Method offers the best framework in which to carry out such a study for an existing mill or when designing a new mill. Through load behaviour measurement techniques one can then control the load behaviour or use data from load behaviour measurements to calibrate a DEM model.

CHAPTER 3

MEASUREMENT TECHNIQUE

Measurement of the Load Behaviour in a Dry Pilot Mill Using an Inductive Proximity Probe

Load behaviour in a dry pilot mill has been successfully measured as a function of mill speed and load filling using an inductive proximity probe. The inductive proximity probe detects the presence of metallic objects in the proximity of its sensing face. Static and dynamic test demonstrate that it is suitable for measuring load behaviour. The shoulder position is measured more reliably by the inductive proximity probe due to this region being well behaved and less variable as compared to the toe region. The shoulder and toe angular positions of the inductive proximity probe signal vary with mill speed and load filling. Cataracting of balls onto the mill shell at high mill speeds is detected. The probe is sensitive to changes in mill operating conditions and load packing. A comparison between the force probe and the inductive proximity probe reveals that the inductive proximity probe is superior in measuring load behaviour.

3.0 INTRODUCTION

Research into the load behaviour in grinding mills has been carried out to give a better understanding of the effect various parameters (i.e. liner profile, mill speed, mill loading etc) have on the load behaviour. This insight can be used to optimise the load behaviour by using mill speed or liner design, which can lead to significant improvements in production capacity, energy efficiency and mill control. Vermeulen et al (1984) and Moys (1985) showed that important information relating to the load behaviour could be obtained from within a mill. The first ever reported study on quantitative forces (radial and tangential) exerted by the load on the liner as a function of operating variables of a pilot scale mill brought about a better understanding of the load-liner interface interactions (Skorupa and Moys, 1993). Powell & Nurick (1996a & 1996b) studied particle motion in an experimental mill by using diagnostic x-rays from a bi-planar angioscope. This novel method is an accurate technique for tracking particle motion anywhere within the charge of a laboratory mill. Kolacz (1997) successfully made use of strain transducers placed on the mill shell to measure the mill load of a dry grinding industrial mill.

This research focuses on the use of an inductive proximity probe in measuring the load orientation in a dry laboratory mill. The need to use the inductive proximity probe in measuring load behaviour came about due to the fact that the force probe measured earlier shoulder positions as

compared to a conductivity probe when used to measure load behaviour in a wet environment (Moys, Smit and Stange, 1996). The probe can also measure the behaviour of the steel balls independent of particles present in the mill.

3.1 THE INDUCTIVE PROXIMITY PROBE

The inductive proximity probe is a solid state electronic device that detects the presence of metallic objects at its sensing face. The probe's principle of operation is based on the induction coil. It is made up of a coil of copper wire wound around a ferrite core, an oscillator, a detection circuit and an output circuit. The oscillator circuit generates a fluctuating current through the copper wire and induces a symmetrical, oscillating low energy electro-magnetic field at the probe's sensing face. When a metallic object moves into this magnetic field, eddy currents are induced and begin to circulate within the object. This eddy current magnetically pushes back and dampens the probe's magnetic field. The probe's detection circuit monitors this dampening effect and when the magnetic effect is sufficiently damped the output circuit is triggered and gives an output.

A 30mm diameter inductive proximity probe with a measuring range of 3 – 8mm from its sensing face was used. A special housing was designed and machined to support and mount the probe into the mill shell as seen in Figure 3.1. The probe was mounted in the mill shell 50mm away from the

front plate. No side sensing of the metallic mill shell occurs as a result of the probe being mounted into the mill shell. The 3mm PVC protection plate bolted on the inside of the mill protects the probe's sensing face from impacts and abrasion caused by balls. A 6.4^{o} angle is subtended by the probe with the centre of the mill thus leading to an uncertainty of $\pm 3.2^{o}$ on the load behaviour measurements. The positioning of the probe relative to the lifters will cause the shoulder's angular position measurements to be detected earlier than expected. This is due to the fact that balls depart from the lifter last.

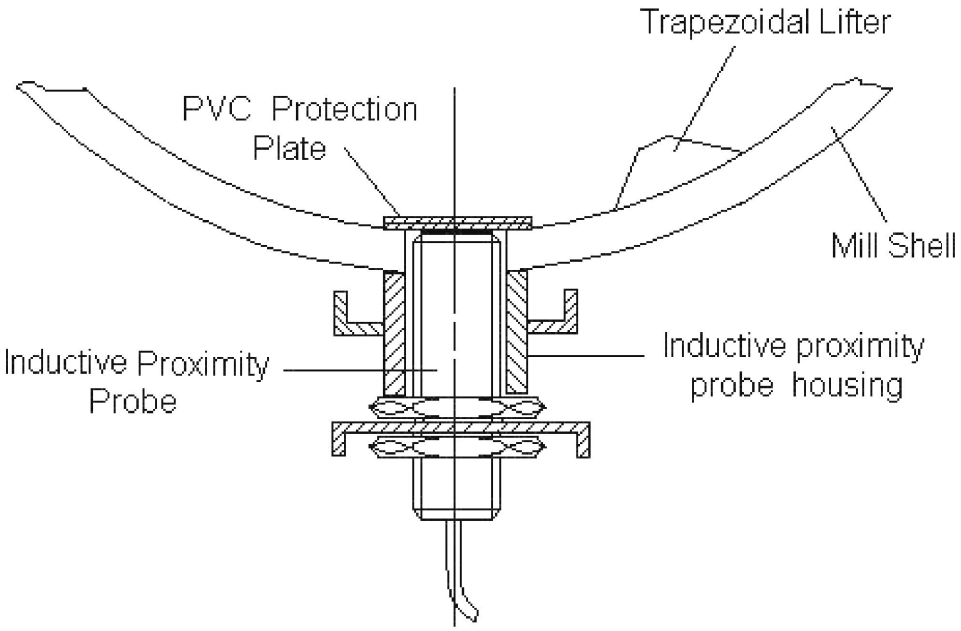


Figure 3.1: Inductive proximity probe's assembly

The inductive proximity probe only detects the outer layer of balls close to the mill shell in its 5mm sensing range from the surface of the PVC

protection plate. Balls beyond this range are not expected to have any influence on the signal.

3.2 EXPERIMENTAL EQUIPMENT AND METHOD

The mill used in these experiments has an internal diameter of 0.54m, length of 0.15m and is equipped with 12 trapezoidal lifters each having a height of 20mm and a 45^{o} face angle. A front glass plate facilitated the taking of still photographs and videos of the tumbling load. An inductive probe and force probe were inserted into the mill. A marker signal made up of an Infra-Red Light Emitting Diode, a spectrally matched phototransistor and a 15mm wide mirror was aligned to the centres of all probes. The inductive and marker signals were combined together to produce a single signal. All signals were sent to a computer-based data acquisition system via slip rings. The mill load comprised of a ball size mix of 6, 7, 8, 9 and 10mm steel balls mixed together in equal proportions by number. The mill filling was varied from 15 - 45% while the mill speeds explored ranged from 60 – 105% of the critical mill speed.

3.3 INDUCTIVE PROXIMITY PROBE SIGNAL ANALYSIS

Preliminary test were conducted on the inductive probe so as to bring about a better understanding of the type of signal that was expected from the probe and to assess the probes suitability in measuring load

behaviour. In the first test a 30mm steel ball was moved across the probe's sensing surface at a distance of 0 to 8mm away from the surface. The grey shaded area in Figure 3.2 indicates the distance covered by the PVC protection plate and the area shaded yellow represents the probe's measuring range.

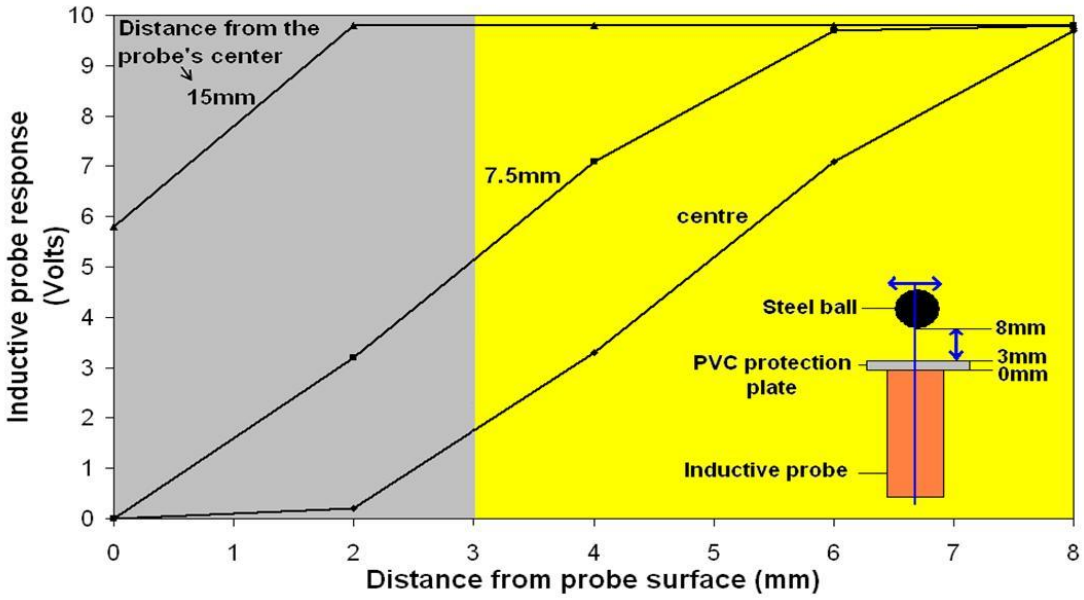


Figure 3.2: Inductive proximity probe's static response curves for a 30mm steel ball at various distances away from the probe's centre.

As the steel ball approaches the probe; the probe's signal drops from a high voltage to a low voltage. The extent of the drop in the signal is affected by the objects shape, size, material and position within the sensing range. The signals obtained from the centre and at a distance of 7.5mm away from the probe's axis vary linearly with an increase in distance of the steel ball away from the probe's sensing face. At a distance

of 15mm away from the probe's centre the steel ball was not detected in the measuring range. The next test characterised the probe's response to a dynamic stimuli. A steel plate 5mm thick was placed on top of the probe and a steel rod was used to knock it off. Figure 3.3 represents the probe's response.

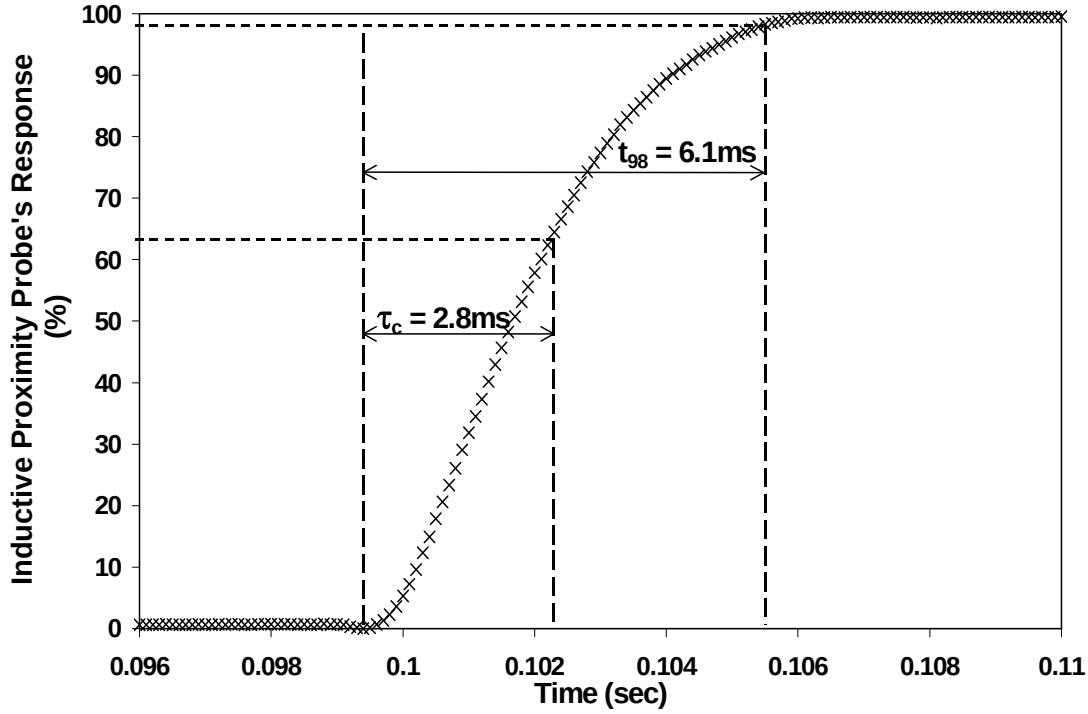


Figure 3.3: Dynamic response of the inductive proximity probe.

The time it takes the signal to rise to 98% of its final value (t_{98}) was 6.9ms. This rise time causes an error of 2.54^{o} on the load behaviour measurements at the highest speed (i.e. 60.87rpm). The time constant (τ_c) was 2.8ms.

3.3.1 Description of the Inductive Proximity Probe's Signal

In Figure 3.4 a typical signal for five mill revolutions (data points) and the average signal of the five mill revolutions (solid line) for a load filling of 35% and mill speed 75% is presented. The different regions of the load behaviour in the photograph and that of the signal from the inductive probe are labelled. An analysis of the bulk toe and shoulder for each individual revolution can be seen in Table 3.1. The load behaviour signals are relatively regular shaped and reproducible for each mill revolution. Impacts prior to the bulk toe are detected between the 90-120^{o} angular position this is due to balls jumping in and out of the toe region. The data from each individual revolution in the toe region (i.e. between 120-160^{o}) show a lot of scatter and a variable drop in the average signal. This occurs as a result of the balls continuously rearranging themselves and trying to pack themselves so as to attain the smallest possible voidage. As balls pack better and are locked into circular paths that move with the same angular velocity of the mill shell (i.e. between 160-290^{o}) the average signal tends to become less variable and the data points from individual revolutions exhibit less scatter. The variation in the signals of some individual revolutions is a result of the ball packing not being the same during each revolution. The rising signal in the shoulder region for individual revolutions as well as the average signal (i.e. between 290-310^{o}) are less scattered as compared to the signal in the toe region.

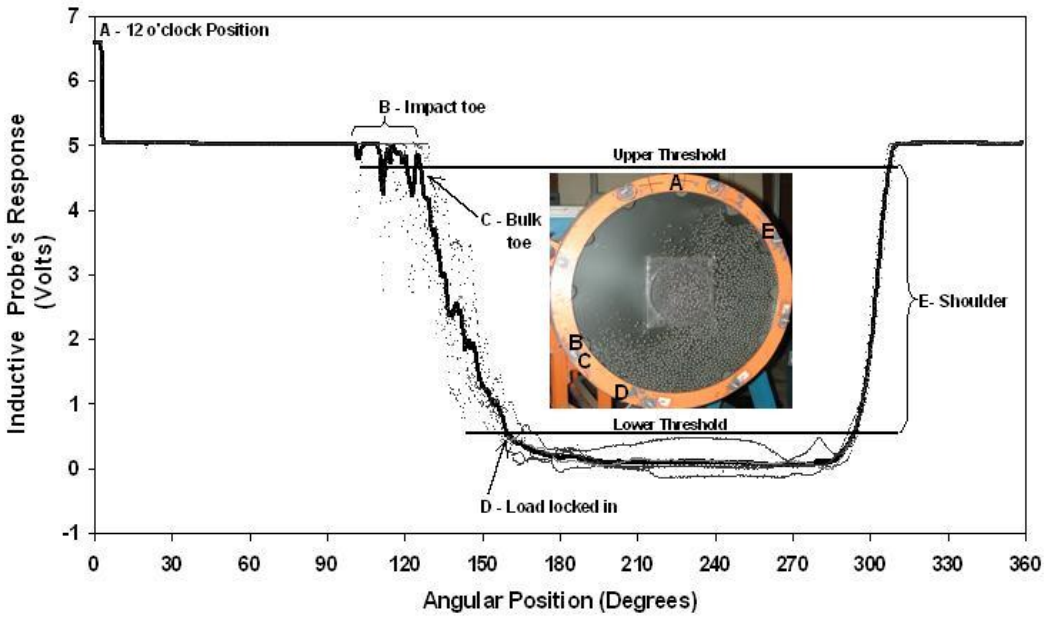


Figure 3.4: Typical signal from the inductive proximity probe for a mill filling of 35% and a mill speed of 75% of the critical mill speed

Table 3.1: Bulk toe, Load locked in and Shoulder angular positions for a mill filling of 35% and a mill speed of 75% of the critical

Mill Revolution	Upper Threshold		Lower Threshold	
	Bulk Toe (Degrees)	**Shoulder** (Degrees)	**Load Locked in** (Degrees)	**Shoulder** (Degrees)
1	125.3	308.4	157.2	294.9
2	119.5	309.3	159.8	292.2
3	125.8	307.0	168.0	294.2
4	126.7	310.0	152.1	295.8
5	129.0	308.7	165.1	294.5
Average	125.3	308.7	160.4	294.3
Standard Deviation	3.5	1.1	6.3	1.3

To process the raw data obtained from the inductive probe meaningfully one has to clearly define the different regions of the load as detected by the inductive proximity probe. Upper and lower thresholds were chosen to analyse the signals obtained as seen in Figure 3.4. The following regions were then defined:

Impact toe: This is the part of the signal where the probe first comes in contact with steel balls. It is labelled as B in Figure 3.4. There is an abrupt, momentary drop in the signal and then it instantly returns to its original high-level voltage state of non-metal detection. It is located just before the bulk toe although for higher mill speeds it is detected much earlier than the bulk toe due to cataracting balls impacting on the down coming side of the mill shell.

Bulk toe: This is the portion of the signal where it drops continuously from its high-level voltage state of non-metal detection eventually reaching the low-level voltage state of the signal. It is labelled as C in Figure 3.4. The upper threshold is used to obtain a quantitative measure of the bulk toe.

Load locked in: This is the point just before the variable dropping signal reaches its low-level voltage state. It is obtained from the lower threshold. It is labelled as D in Figure 3.4.

Shoulder: Due to the measuring range of the inductive proximity probe being 0 – 5mm from the PVC protection plate the shoulder can either be chosen as when the signal just starts to rise from the low level voltage state (i.e. the lower threshold) or when it is close to the high level voltage state (i.e. the upper threshold). In the former case the shoulder position can be viewed as the time when some balls are just leaving the surface of the PVC protection plate and most of the balls still lie within the measuring range. In the latter case most balls have just left the upper limit of the measuring range and definitely no balls are in contact with the PVC plate. It is labelled as E in Figure 3.4.

3.4 EXPERIMENTAL RESULTS AND ANALYSIS

3.4.1 Inductive Proximity Probe's Signal as a Function of Mill Speed

The average signals for five revolutions were plotted as a function of mill speed for a ball filling of 35% as in Figure 3.5 and the corresponding photographs of the load are seen in Figure 3.6. For mill speeds up to 90% of the critical mill speed the inductive probe's signal displays an increase in abrupt momentary drops in the toe region as mill speed is increased indicated as A in Figure 3.5. At low speeds balls jumping in and out of the toe cause the brief drops in signal and as the speed increases cataracting of balls onto the toe and the mill shell are the major cause. The signals from shoulder region indicate a small but gradual change to higher angular positions as mill speed is increased. For mill speeds greater than 90% of

the critical mill speed distinct drops in the inductive proximity probe's signal are detected close to the 60^{o} angular position (indicated as B in Figure 3.5); this is caused by cataracting balls impacting on the mill shell.

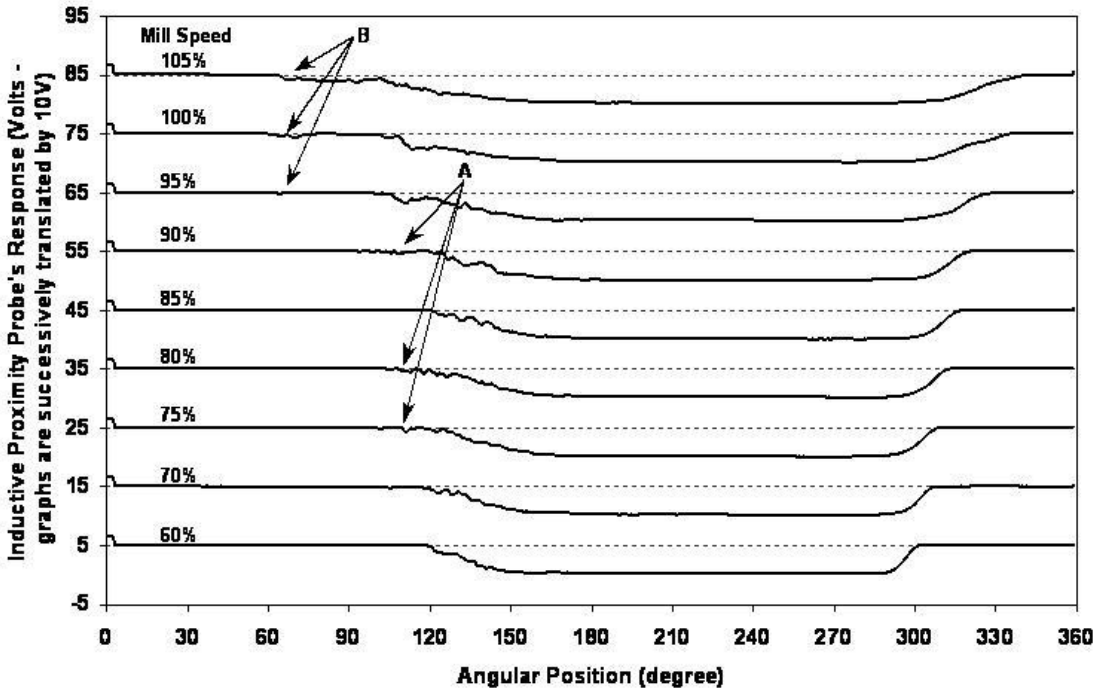


Figure 3.5: Inductive probe's signal as a function of mill speed for a load filling of 35%

This sort of behaviour is also reflected in Figure 3.6 for mill speeds of 95%, 100% and 105%. The signal from the shoulder region becomes less steep at high speeds and covers a wider angular range. After the balls in contact with the PVC plate and within the measuring range of the inductive probe are projected into space they follow a trajectory that lies within the probe's measuring range and travel a wider angular range before leaving the upper limit of the probe's measuring range. This behaviour is clearly

reflected by comparing the balls in the shoulder region in Figure 3.6 as mill speed is increased.

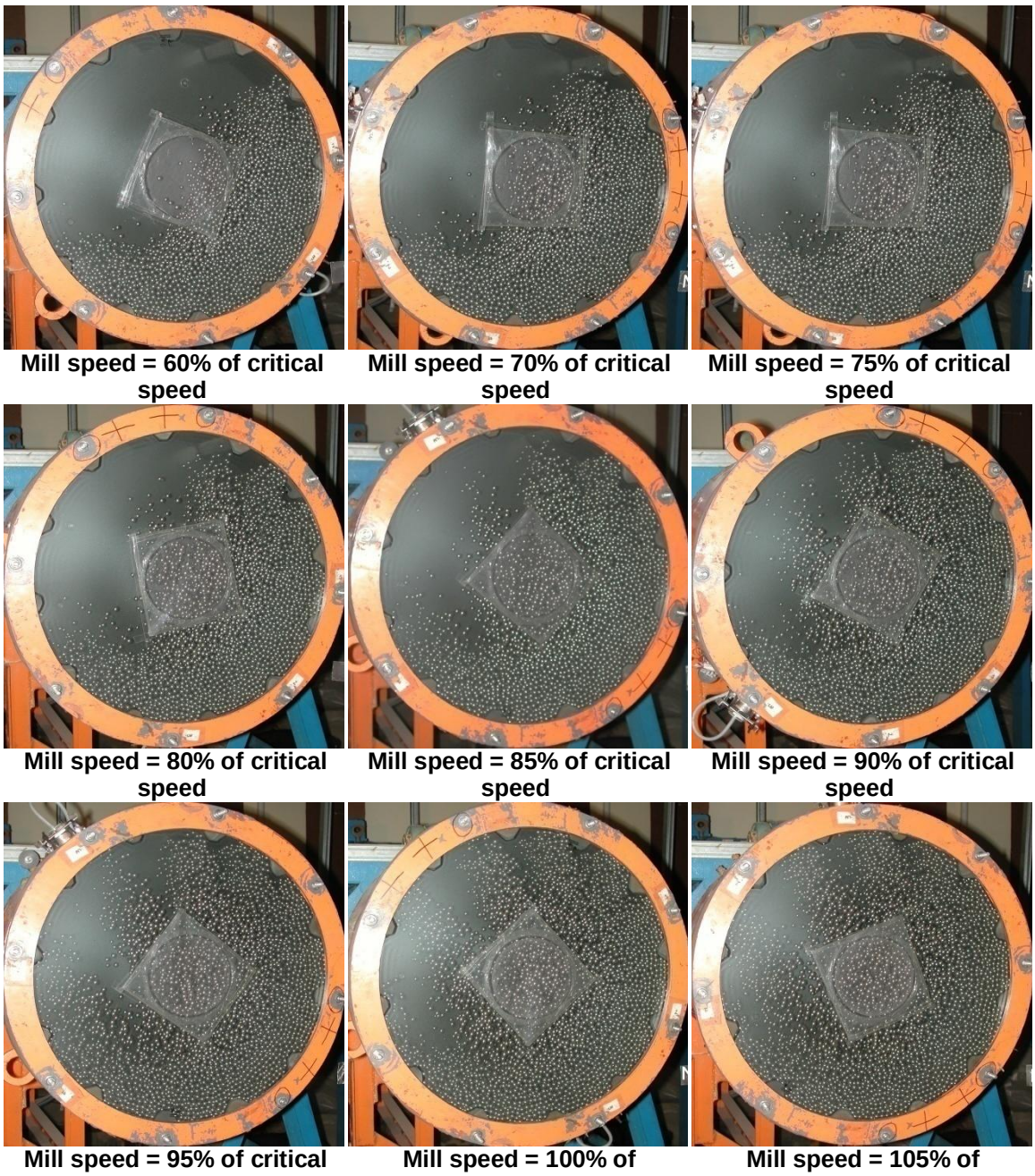


Figure 3.6: Photographs of the load behaviour as a function of mill speed for a load filling of 35%

3.4.2 Inductive Proximity Probe's Signal as a Function of Mill Filling

The average signals for five revolutions were plotted as a function of ball filling at 75% of the critical mill speed. The average signal at low mill fillings (J = 15%) is noisier than signals for higher mill fillings (J > 25%) as seen in Figure 3.7.

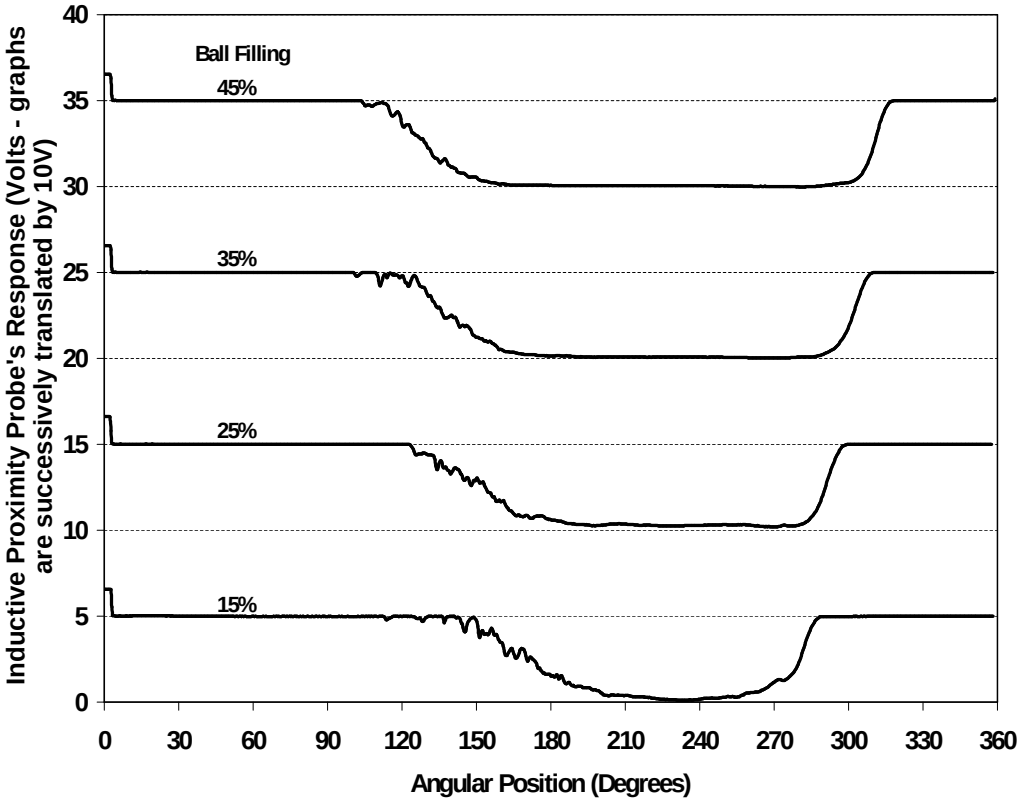


Figure 3.7: Inductive proximity probe's signal as a function of mill filling for a mill speed of 75% of the critical mill speed

This is due to the pressure exerted by the mill load on the liner being low thus causing the balls to loosely slide over the probe's sensing surface thus causing fluctuations in the signal. For higher mill fillings the inductive

proximity probe's signal at the toe region is less noisy than that of low mill fillings. This is due to the charge surface forming a tri-linear saddle shape as explained by Dong and Moys (2003). This shape of the charge causes more balls to be consolidated at the toe region therefore improving their packing at high mill fillings despite the turbulent nature of the toe region as seen in Figure 3.8. The shoulder position moves to higher angular positions as mill filling is increased.

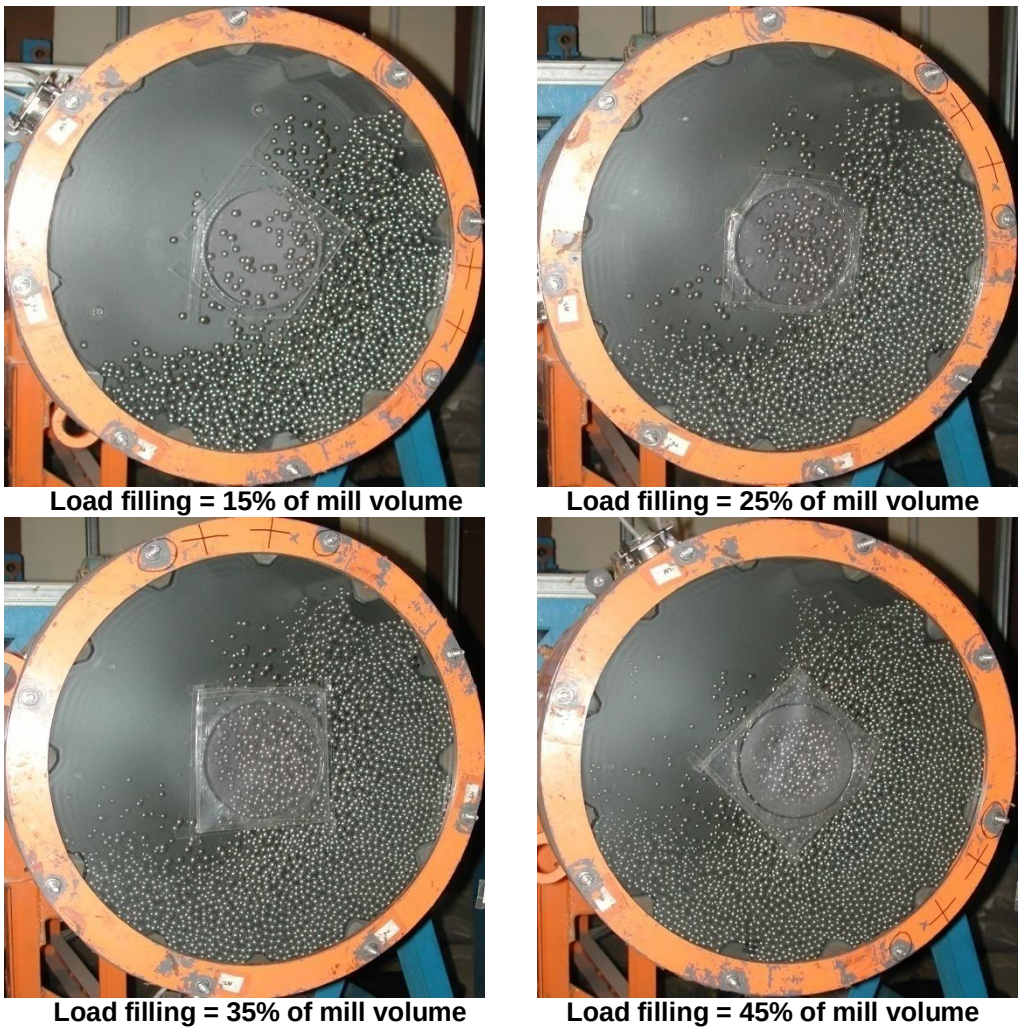


Figure 3.8: Load behaviour as a function of load filling for a mill speed of 75% of the critical mill speed.

3.4.3 Load Orientation as a Function of Mill Speed and Mill Filling

The load orientation as a function of mill speed and filling is represented in Figure 3.9. The error bars represent ±1 standard deviation calculated from the measurements of the toe and shoulder positions of five mill revolutions. The toe of the load remains relatively constant up to 90% of the critical mill speed after which it moves rapidly to lower angular positions. This is due to the increased cataracting of balls onto the mill shell close to the toe region at high mill speeds.

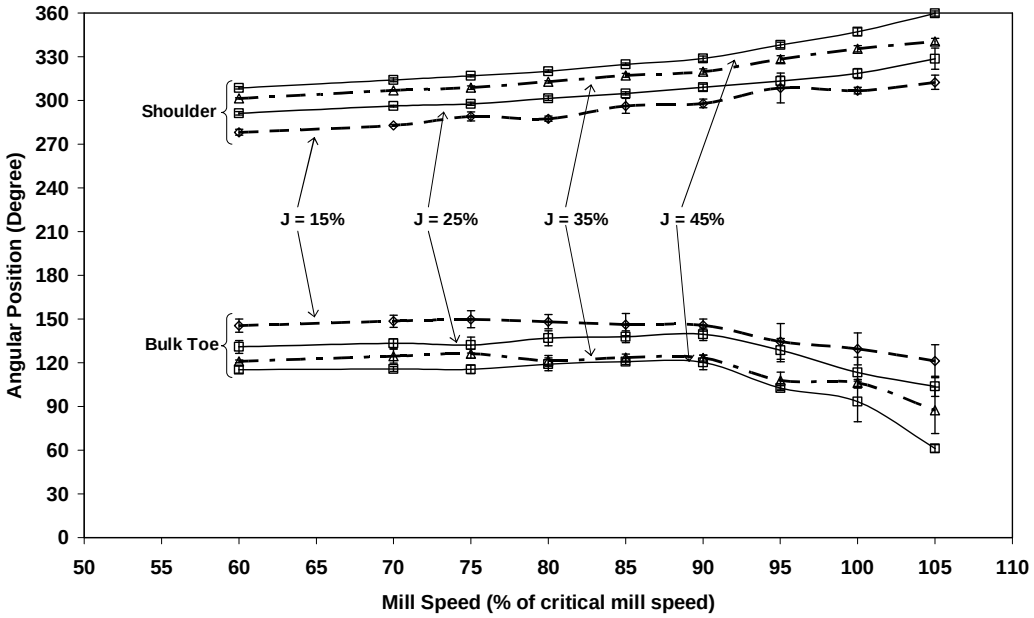


Figure 3.9: Load orientation as a function of mill speed and filling measured by the inductive proximity probe

The toe position for higher mill fillings is at a lower angular position than that of lower mill fillings. The shoulder of the load increases gradually to higher angular positions as mill speed is increased to 90% of the critical

mill speed due to more lift being imparted to the load as mill speed is increased. At speeds greater than 90% of the critical mill speed the tendency of the load to start centrifuging causes the shoulder position to move rapidly to higher angular positions. The shoulder's angular position is higher for higher mill fillings than for lower mill fillings, and the toe position is earlier. Higher mill fillings tend to result in cataracting earlier than low mill fillings.

3.4.4 Comparison of the Inductive Probe with the Force Probe

An experiment was performed so as to obtain a comparison between a force probe that measures the radial forces exerted by the load on the mill shell and an inductive proximity probe. The results of this experiment can be seen in Figure 3.10 and a quantitative analysis in Table 3.2. The ball filling was 15% and the mill was run at 75% of the critical mill speed. The toe position of the force probe signal was obtained by assuming it to be the point where there is an evident sudden increase in the force signal and the shoulder position was determined as the intersection of a two straight lines fitted to the decreasing force signal and the no load force signal as described by Moys, Smit and Stange (1996).The force probe measured the location of the shoulder of the load earlier than the inductive proximity probe. In this case it is actually at an angular position 12.6^{o} earlier than that measured by the inductive proximity probe at the lower threshold ($\theta_{sh,\ Ind,\ 2}$) and 27.4^{o} earlier than that measured at the upper threshold ($\theta_{sh,\ Ind,\ 1}$).

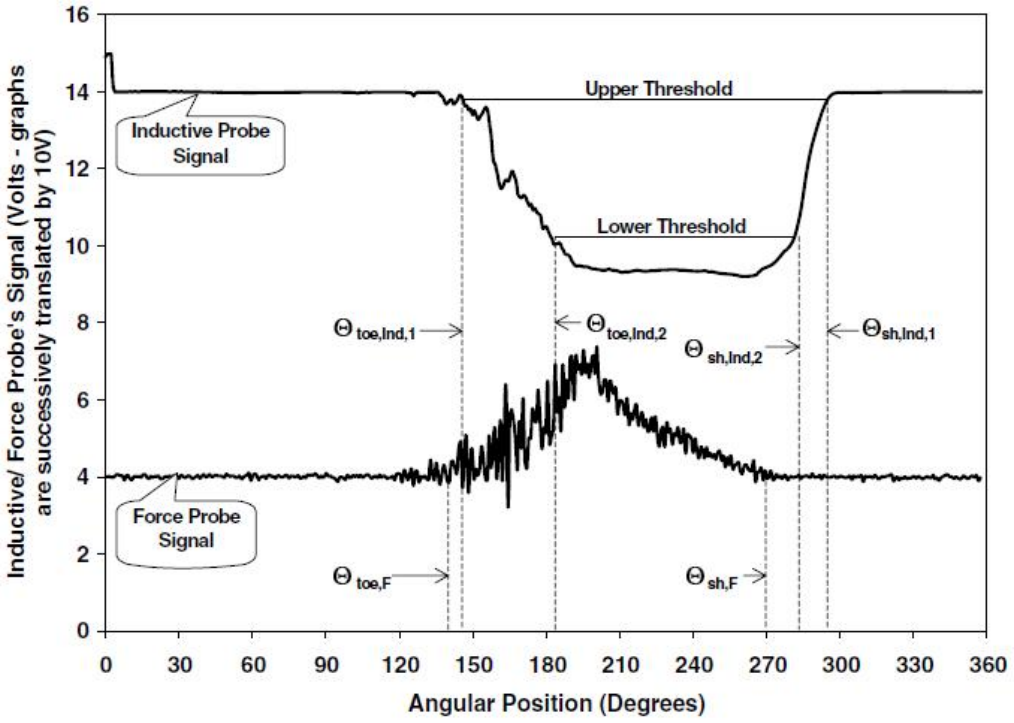


Figure 3.10: Inductive proximity and force probe signals for J = 15% and N = 75%

Table 3.2: Analysis of the inductive and force probe signals for five revolutions for J = 15% and N = 75%

	Inductive Proximity Probe				Force Probe	
	Upper Threshold		Lower Threshold			
Mill Revs.	**Bulk Toe**	**Shoulder**	**Load Locked In**	**Shoulder**	**Bulk Toe**	**Shoulder**
1	138.8	296.0	185.8	279.8	142.8	270.9
2	145.5	298.8	178.8	282.6	134.3	264.0
3	147.2	296.0	181.9	280.6	142.0	268.6
4	149.0	295.6	179.2	284.0	142.8	270.9
5	147.6	298.2	177.7	283.5	141.3	273.2
Average	145.6	296.9	180.7	282.1	140.6	269.5
Standard Deviation	4.0	1.5	3.2	1.8	3.6	3.5

The force probe cannot measure the shoulder position accurately because at angular positions greater than 270^{o} the balls in contact with the force probe exert little or no radial force and are held in contact with the force

probe by their own momentum and support from balls below. Thus the inductive proximity probe is more suitable than the force probe in measuring the shoulder's angular position. A 5^o difference is seen between the measurements of the toe position from both probes. The force probe registers an earlier toe as compared to the inductive proximity probe.

3.5 CONCLUSION

An inductive proximity probe was employed in this study and has been shown to be suitable in measuring the load orientation within the mill as a function of operating conditions prevailing. A reliable measure of the shoulder position can be obtained from the inductive proximity probe due to the well-behaved nature of this region as compared to the toe region, which is a turbulent and variable region. Direct impacts onto the mill shell by the cataracting balls were also detected. The load lock-in position can also be located. Comparisons between the inductive proximity probe and the force probe reveal that inductive probe is superior in measuring the shoulder position. The nature of the signal from the inductive probe for different mill speeds and fillings differ. A change in ball packing and the tendency of the load to slip at low mill fillings is also detected. This shows that the probe is sensitive to changes in operating conditions prevailing in the mill and also changes in load structure.

CHAPTER 4

EXPERIMENTAL STUDY

Particle filling and size effects on the ball load behaviour and power in a dry pilot mill: Experimental Study

The ball load behaviour in a pilot mill is studied under conditions of increasing particle filling, for coarse silica feed (0.8-1.8mm) and fine silica feed (0.075-0.3mm), at the mill speeds of 63, 78, 88 and 98% of the critical. An inductive probe is used to obtain the ball load behaviour independent of particles present in the mill. The difference in mill power draw obtained from the coarse and fine particle charges are explained via their load behaviour signals. The effect of particle filling and size on the ball load behaviour is quantified through the toe and shoulder angular positions. Radial segregation of the coarse silica particles to the periphery of the charge occurs. A radial segregation index related to the extent of drop in the inductive probe's signal has been defined and used to quantify radial segregation as a function of particle filling and mill speed.

4.0 INTRODUCTION

Ball mills are typically operated close to their maximum power draw. At the maximum power draw, it is assumed that the ball charge is well mixed and void spaces between the balls are filled with particles. But, in reality, particles can influence the ball charge in various ways causing the maximum power draw to shift depending on the nature of the influence. The ball load contributes to the bulk of the charge mass; consequently a change in the location of its centre of gravity significantly affects the power drawn by the mill. It is therefore worthwhile to study the behaviour of the ball charge and the influence particles have on it. From such a study, one can infer the conditions within the charge that lead to maximum power draw and optimal throughput.

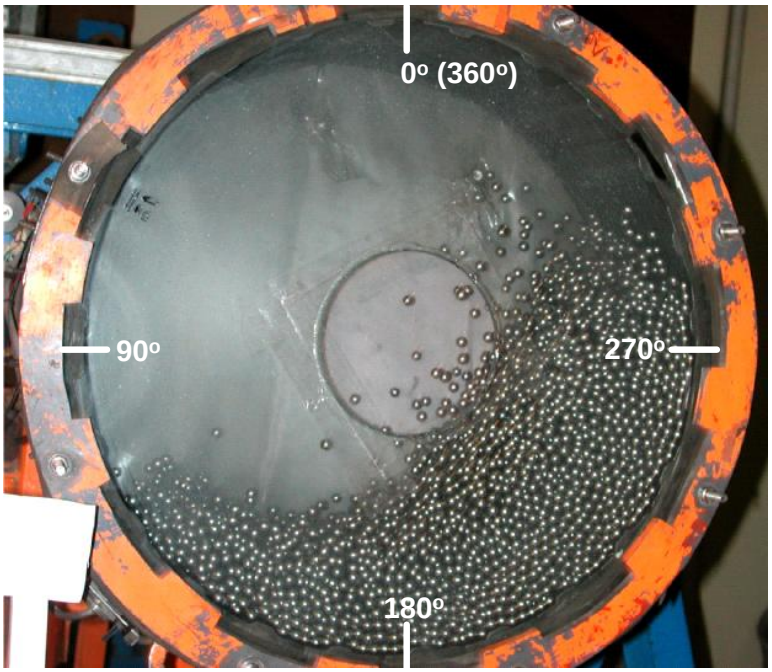
Several intrusive and non-intrusive techniques have been developed to measure the dynamic behaviour of a mill's charge in order to improve the understanding, optimisation and control of mills. These techniques include strain (Kolacz, 1997; Tano et al, 2005), acoustic emissions (Pax, 2001), vibration (Zeng & Forssberg, 1992; Campbell et al, 2001; Behera et al, 2007), x-rays (Powell & Nurick, 1996a & 1996b), conductivity (Moys, 1985), force (Moys & Skorupa, 1993) and inductivity (Kiangi and Moys, 2006). The following study uses a novel technique that measures ball load behaviour with an inductive proximity probe. The probe has been shown to be capable of obtaining useful information directly related to the ball load

behaviour in a pilot mill (Kiangi and Moys, 2006); including an industrial mill (Dong et al, 2005). It's intended use however, is not to be developed as a tool for mill control, but rather to be used to obtain useful information that can help one better understand the ball load behaviour and the variables that affect it. This chapter presents an experimental study of the effect that both particle filling and size have on the ball load behaviour and net power in a dry batch pilot mill.

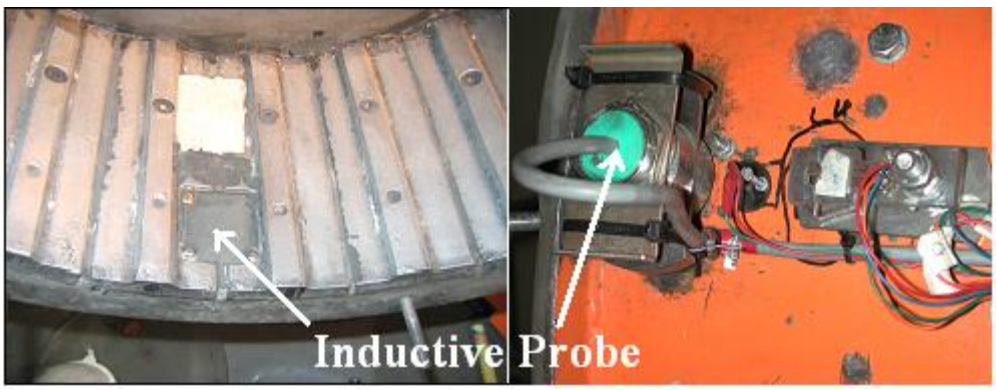
4.1 EXPERIMETAL EQUIPMENT AND METHOD

A mill of diameter 0.526m and length 0.18m was used (Figure 4.1a). The mill rotates in an anticlockwise direction i.e. in the direction of increasing angular displacement. The mill was fitted with 24 trapezoidal lifters, each with a height of 5mm and a face angle of 45^{o}. The lifters are scaled down versions of Eskom's Matimba power station's worn liners. The ball load was filled to 20% (36.08kg) of the mill's internal volume, similar to that found in Eskom's coal mills and comprised of 6,7,8,9 and 10mm balls mixed together equally in number. The inductive probe was placed between two lifters 20mm from the front end plate and a grey PVC protection plate was bolted on the inside of the mill over the probe's sensing surface so as to protect the probe from the harsh conditions prevailing in the mill (Figure 4.1b). The probe senses the presence of steel balls within a 5mm range from the surface of the PVC protection plate (i.e. equivalent to the height of the lifters). As a result, the inductive probe could

only sense balls in the outer 5mm layer of the charge in contact with the mill shell. The net torque was measured via a calibrated load beam after subtracting the mill's no-load torque from the gross torque obtained.



a) Photograph of the mill and axis of orientation of the load



b) Inductive probe installation on the mill

Figure 4.1: Photograph of the mill and the installation of inductive proximity probe.

Silica sand with a bulk density of 1480kg/m^3 was used as feed material. The coarse silica sand particle size was 0.8-1.8mm (50% passing

1102μm) as seen in Figure 4.2a and the fine silica sand particle size was 0.075-0.3mm (50% passing 173μm) as seen in Figure 4.2b. The silica sand was coned, quartered and riffled in order that a representative feed sample could be obtained. Particle filling was defined as the fraction of void spaces within the resting ball load that are filled with particles. Coarse particle fillings of 20-150% (0.92-6.87kg) and fine particle fillings of 20-160% (0.92-7.33kg) were used during experimentation.



a) Coarse particles **b) Fine particles**

Figure 4.2: Photographs of the coarse and fine particles

For each particle filling, four different mill speeds were used; they were varied from 63-98% (37-57.6rpm) of the critical. The inductive probe and load beam signals were sampled for each particle filling and mill speed used. The sampling time for each particle filling at a specific mill speed was 22.6s which yielded about 10 to 13 mill revolutions at the lowest speed used. The signals were sampled twice per degree at the highest mill speed used and translated to a sampling frequency of 708Hz. Consecutive

particle fillings were attained by adding fresh silica onto the charge containing ground silica sand from the previous particle filling. The total grinding time for the coarse and fine particle experiments were about 15 minutes each. Performing the experiment in this manner would lead to an increasing amount of fines generated within the load as particle filling is increased. The particle size distribution at the end of the experiments was 50% passing 711μm for coarse particles and 50% passing 61μm for fine particles. It was deemed reasonable to perform a short experiment at a single speed so as to reduce the extent of change in particle size distribution as particle filling is increased and deduce the effect it has on load behaviour and power.

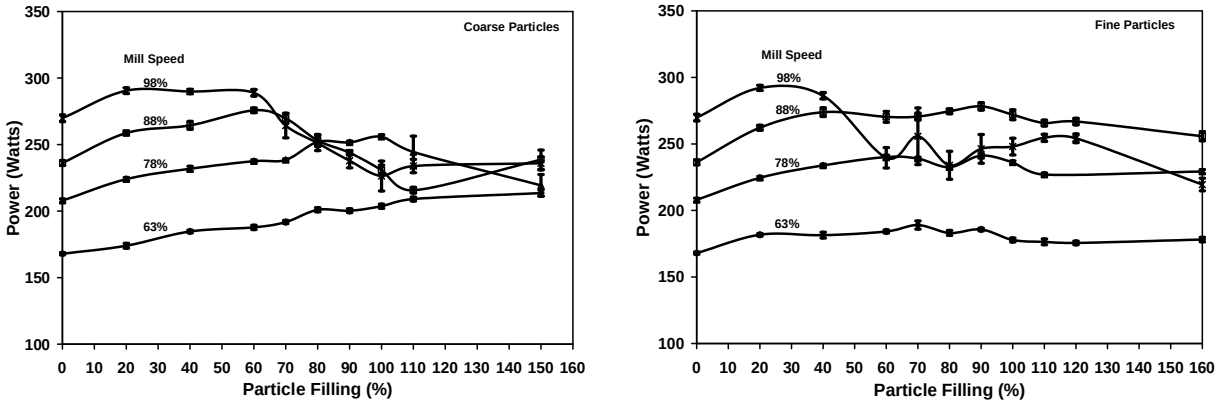
4.2 RESULTS AND DISCUSSIONS

The data yielded various power curves, which are analysed below with respect to their corresponding load behaviour signals. All power and load behaviour signals plotted for each individual particle filling at a specific speed are an average of ten mill revolutions. Additionally, error bars included in graphs represent one standard deviation from the average value.

4.2.1 Effect of particle filling and particle size on the net power

There is a notable difference in the variation of net power with increasing particle filling for both coarse and fine particles as illustrated in Figure 4.3.

For coarse particle fillings at 63% of the critical speed (Figure 4.3a), the power increases gradually as particle filling is increased to 150%. Increasing the mill speed to 78% of the critical causes the mill power to peak between the particle fillings of 70-110%. Further increasing the mill speed shifts the peak power to lower particle fillings between 40-70% for 88% of the critical speed and between 20-60% for 98% of the critical speed. A rapid decrease in the power is experienced following the peak in power for 78, 88 and 98% of the critical speed. Mills are operated close to where the peak power occurs and at this power it is assumed that the void spaces between the balls are fully occupied with particles. If the maximum power drawn shifts to lower particle fillings as the mill speed increases it can cause increased ball and liner wear rates for that period of operation as they will be fewer particles present in the mill at high mill speeds than at low mill speeds.



a) Coarse particles **b) Fine particles**

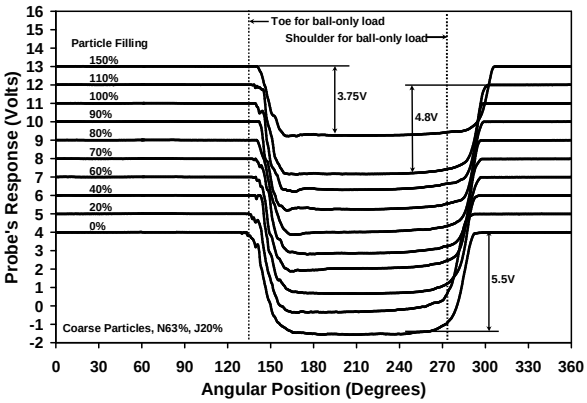
Figure 4.3: Variations in net power draw with particle filling at different mill speeds for a ball filling of 20%.

For the fine particle curves (Figure 4.3b), the power drawn at 63, 78 and 88% of the critical speed are relatively flat compared to those obtained for the coarse particles (Figure 4.3a). Additionally, the peak in power for the fine particle filling occurs between particle fillings of 80-110%. At the mill speed of 98% of the critical, the peak power shifts to lower particle fillings between 20-40% and rapidly drops at higher particle fillings. Similar results have been found where the maximum power draw occurs when the powder filling fraction is about 0.6 and 0.5 for rod and ball mills respectively (Zeng & Forssberg, 1991). Likewise, in a wet mill where the net mill power depends on the slurry concentration and powder filling there is an optimum powder filling for each slurry concentration that gives a maximum in power (Tangsathitkulchai, 2003).

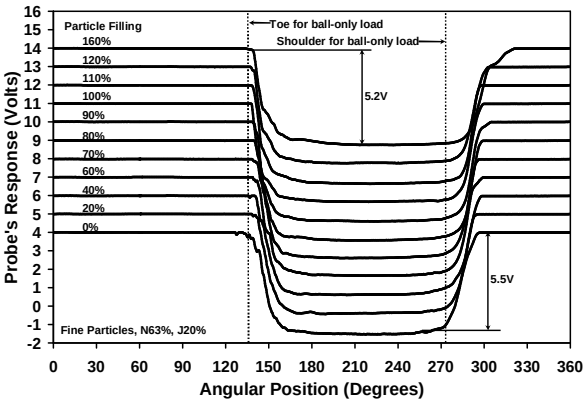
4.2.2 Effect of particle filling and particle size on the ball load behaviour

Figure 4.4 illustrates the inductive probe's signal and ball load orientation as a function of particle filling at a mill speed of 63% of the critical. The load behaviour signals for each particle filling are translated by one volt along the probe's response axis so as to improve their visibility (Figure 4.4a and 4.4c).Vertical dotted lines indicate the toe and shoulder angular positions for the ball-only load. Addition of coarse particles to the ball load causes a gradual rise in the shoulder's angular position from 280^{o} to 297^{o} (Figure 4.4b). The power at this mill speed rises continuously despite the charge's density dropping at particle fillings greater than 100%. A rise in

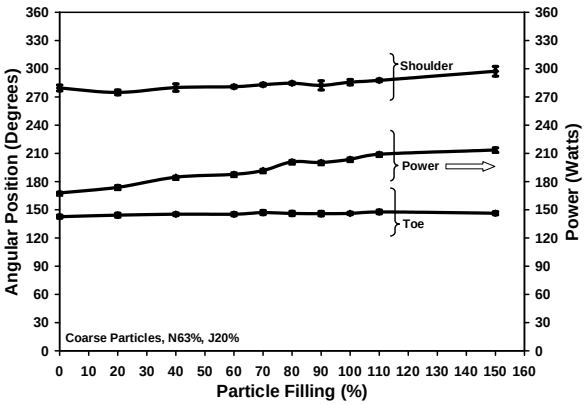
the shoulder's angular position from 280^o to 295^o is experienced with increasing fine particle filling (Figure 4.4d). For fine particles the power drops slightly after a particle filling of 90% despite the shoulder's angular position rising to 295^o. In both cases, the toe's angular position remains constant. In the inductive probe's response for coarse particles (Figure 4.4a), the voltage drop changes gradually from 5.5V for the ball-only load to 4.8V at a particle filling of 110%.



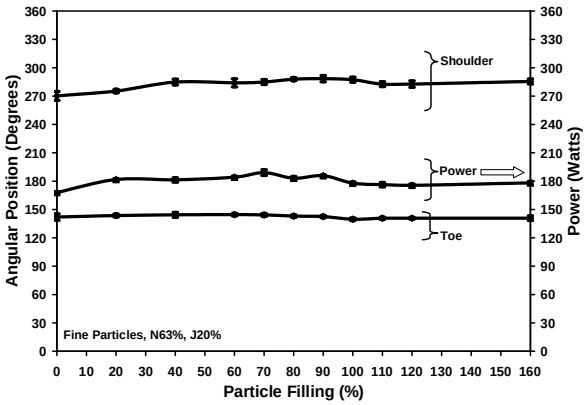
a) Inductive probe signal - coarse particles



c) Inductive probe signal – fine particles



b) Load orientation and Power – coarse particles

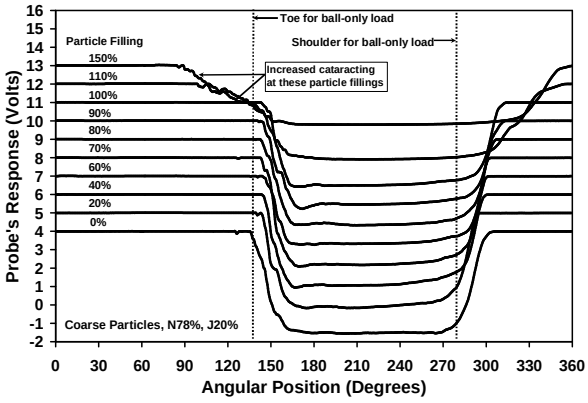


d) Load orientation and Power – fine particles

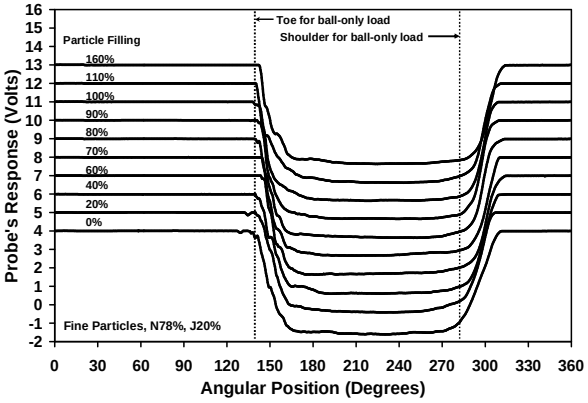
Figure 4.4: Inductive probe's signal, ball load orientation and Power draw as particle filling increases at 63% of the critical speed for a ball filling of 20%.

A further increase in the particle filling to 150% leads to a substantial voltage reduction to 3.75V. Most likely radial segregation is occurring within the coarse particle charge. Here, the particles are preferentially segregated to the periphery of the load in contact with the mill shell. To determine radial segregation, a comparison of the extent in voltage drop from signals obtained in a ball-only load versus a combined ball-particle load was made. A detailed discussion on radial segregation within the load is dealt with in greater depth further on in this chapter. In the fine particle charge segregation of particles to the periphery of the charge did not occur. Fine particles do not interfere with ball behaviour because they are more likely to occupy the void spaces and be effectively fluidised as compared to coarse particles.

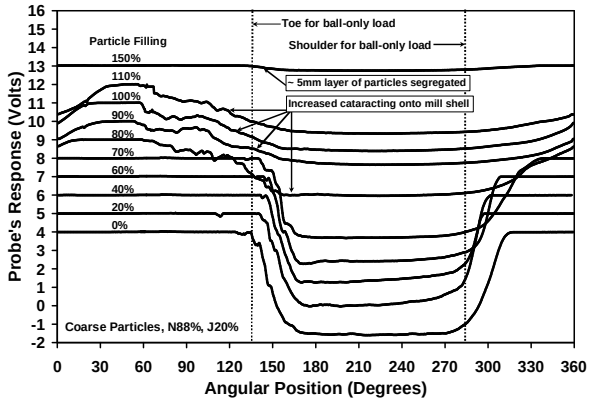
At 78% and 88% of the critical speed, the inductive probe's signal and load orientation as a function of particle filling are shown in Figure 4.5. Increasing the coarse particle filling from 20% to 100% at 78% of the critical speed (Figure 4.5c) causes the toe and shoulder's angular position to remain relatively constant. At particle fillings greater than 100%, the shoulder rapidly rises to higher angular positions while the toe moves to lower angular positions. The toe's angular position is affected by balls cataracting onto the mill shell (Figure 4.5a), leading to a rapid loss in power at particle fillings greater than 100% (Figure 4.5c). Upon increasing the speed to 88% of the critical, cataracting onto the mill shell commences after a particle filling of 70% (Figure 4.5b).



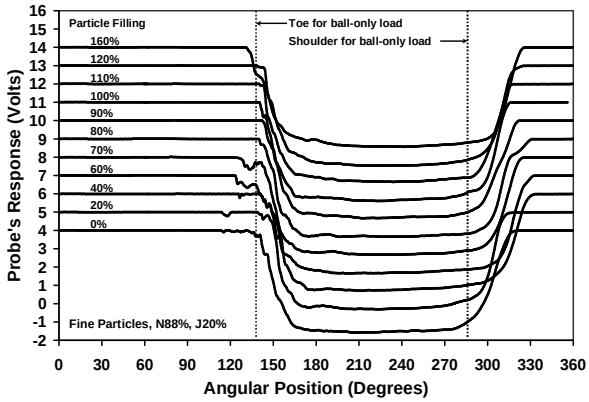
a) Inductive probe signal - coarse particles (Mill speed = 78%)



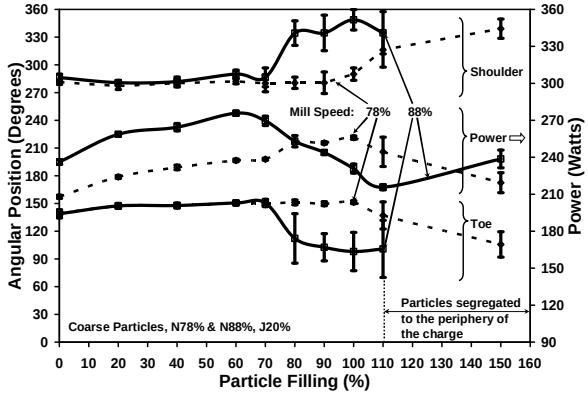
d) Inductive probe signal – fine particles (Mill speed = 78%)



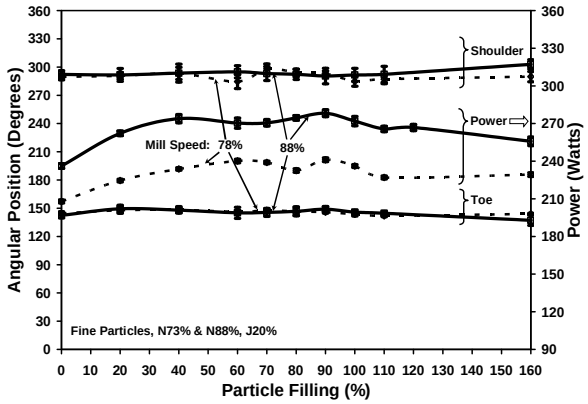
b) Inductive probe signal - coarse particles (Mill speed = 88%)



e) Inductive probe signal – fine particles (Mill speed = 88%)



c) Load orientation and Power - coarse particles



f) Load orientation and Power - fine particles

Figure 4.5: Inductive probe's signal, ball load orientation and Power as particle filling increases at 78 and 88% of the critical speed for a ball filling of 20%

At the particle filling of 150%, the inductive probe signal dropped by 0.27V between 138^{o}-307^{o} (Figure 4.5b). This is due to 5mm of coarse silica particles segregating to the periphery of the load. For fine particles at 78% of the critical speed, the shoulder's angular position gradually rises from 289^{o} to 300^{o} at the particle filling of 70% (Figure 4.5f) then proceeds to drop slightly. Increasing the mill speed to 88% produced a higher shoulder angular position compared to that seen at 78% of the critical. The shoulder rises from 289^{o} to 306^{o} at a particle filling of 60% then drops slightly at higher particle fillings. The toe's angular position for both mill speeds remains constant as the fine particle filling is increased.

Variations in the inductive probe's signal and ball load orientation with particle filling at 98% of the critical speed are shown in Figure 4.6. The average inductive probe's signal of ten mill revolutions for a ball-only load exhibits a dominant drop between the angular positions of 30^{o} and 60^{o} (Figure 4.6a and Figure 4.6c). This drop is caused by balls cataracting and impacting the exposed mill shell, eventually bouncing off again to rejoin the load at an angular position greater or equal to 120^{o}. The error bar at the valley of the signal drop is equivalent to one standard deviation of the signal strength at the angular position 44^{o} and indicates the variation in signal strength due to cataracting balls striking the exposed mill shell. This variation shows that the amount of balls striking the mill shell varies per mill revolution. Addition of silica sand to the ball load results in a drop in

the shoulder's angular position for coarse particle fillings of 20% and 40% (Figure 4.6b) and fine particle filling of 20% (Figure 4.6d). This drop in shoulder position eliminates the tendency of balls to impact the mill shell.

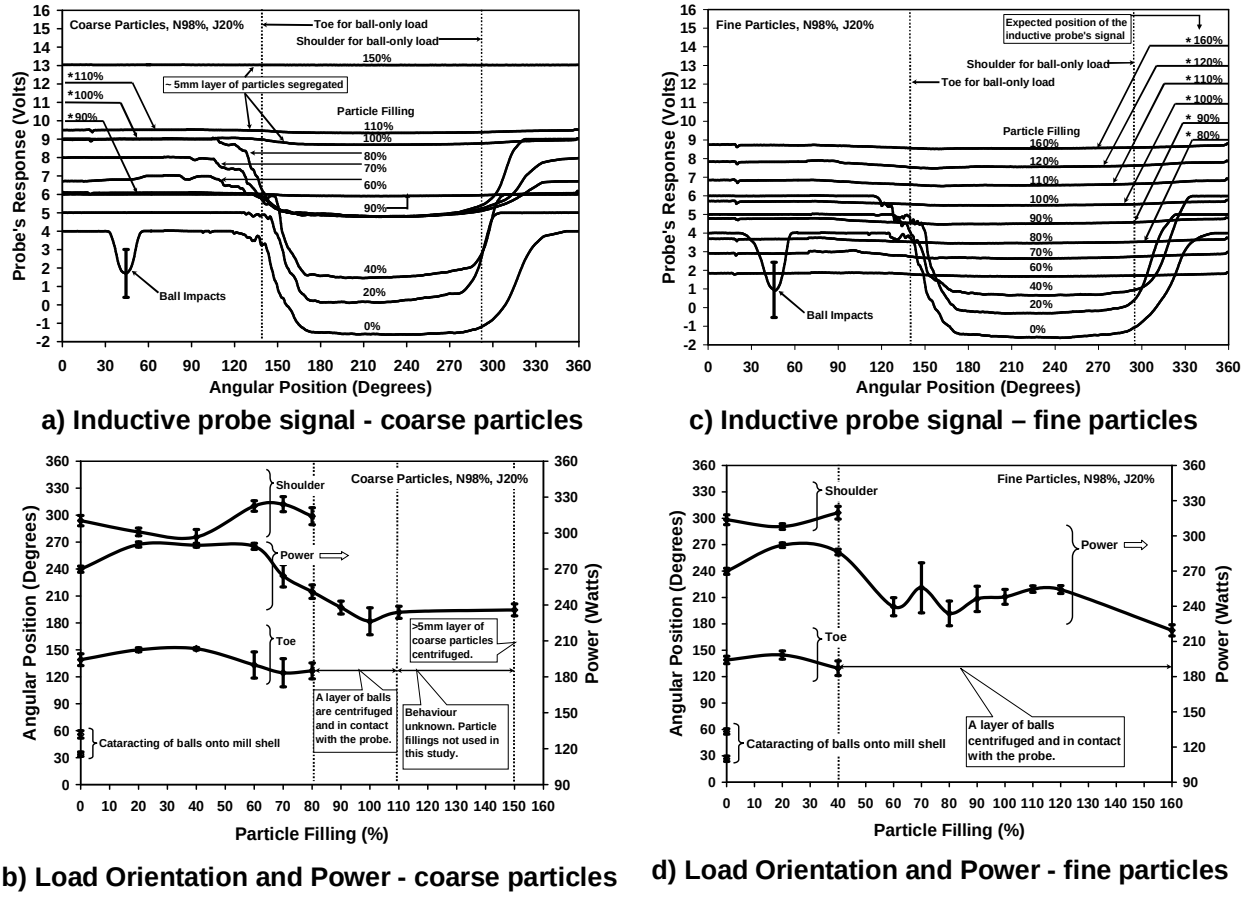


Figure 4.6: Inductive probe's signal and ball load orientation as particle filling increases at 98% of the critical speed for a ball filling of 20%.

For coarse particle fillings of 60, 70 and 80%, a layer of coarse silica sand is segregated to the periphery of the load. At the shoulder, the segregated coarse silica sand is projected into the open cavity of the mill and will most

likely occupy the outermost trajectory of the cataracting material. This will shield the steel balls from impacting onto the exposed mill shell and will have no contact with the inductive probe's sensing face. The arrows in Figure 4.6a and 4.6c identified by an asterisk beside their particle fillings show the expected position of the inductive probe's signal (as if no balls were in contact with the probe) and its subsequent drop during the mill revolution. A drop in the inductive probe's signal to a low voltage state over a full mill revolution indicates that some balls have centrifuged. For coarse particle fillings between 90-110% (Figure 4.6a) and fine particle fillings greater than 40% (Figure 4.6c), the inductive probe's signal dropped to a low voltage state over a full mill revolution. For coarse particles in Figure 4.6a, the extent of drop in the signal changes from 4V for a particle filling of 90% to 2V for particle fillings of 100% and 110%. This change indicates that as particle filling is increased from 90-110%, either fewer steel balls centrifuge for particle fillings between 100-110% than at 90% or more of the coarse silica sand centrifuged. For the particle fillings of 150%, no balls were detected suggesting that a layer of particles at least 5mm thick was either segregated or centrifuged. From the previous particle fillings of 90-110% all indications lead to the preference of coarse silica particles to centrifuge thus it is most likely that at a coarse particle filling of 150% a layer of coarse particles was centrifuged. A layer thicker than 5mm would shield the balls away from the sensing range of the inductive probe thus not activating it.

4.3 RADIAL SEGREGATION WITHIN THE LOAD

Intuitively one would always view that the addition of particles to a ball load would result in a well mixed charge. In this well mixed charge the particles would somehow be caught up in the void spaces within the ball load, most likely by percolation, and move with the motion of the load. However, a load comprised of particles of different sizes and densities can lead to radial segregation within the load (Jain et al, 2005; Powell & Nurick, 1996b; Cleary, 1998). The inductive probe detects the presence of steel balls within its sensing range. The strength of the inductive probe's output signal depends on the volume of metal presented to it, the shape of the metallic object and the type of metal. In the case of a ball only load, the probe's output signal is expected to be at a maximum voltage drop when the probe is under the ball load and slight variations in signal will be caused by balls packing differently per mill revolution as explained in detail in Chapter 3. By introducing silica sand into the mill it was expected that the silica sand would interfere with the ball load and hence result in a reduction in the inductive probe's voltage drop. For fine particle addition, at high particle fillings it was expected that the excess particles would reduce the charge density and hence the volume of metal (steel balls) presented into the probe's sensing range thus affecting the probe's output signal. No substantial change in the inductive probe's signal occurred even at high fine particle fillings (> 100%). For the coarse particles the probe's voltage drop decreased as a function of particle filling and mill speed. A reduction

of balls (i.e. metal volume) from within the probe's sensing range can only occur when there is an increased amount of silica particles within the sensing range in conjunction with the subsequent displacement of some or all balls. This can occur either by a layer of particles being present beneath the balls thus displacing them or a few balls being trapped in a particle bed formed within the probe's sensing range. Either way they must be a process causing coarse particles to be preferentially located at the periphery of the load in contact with the mill shell even at low particle fillings (< 100%). The intensity of this process increases with particle filling and mill speed to an extent where a 5mm layer of particles can be formed e.g. mill speed of 88% and particle filling of 150% in Figure 4.5b. This process is radial segregation occurring within the load when coarse particles are added.

It is beneficial to study and quantify the segregation process in terms of particle filling and mill speed. Having quantified the segregation process one can determine its effects on power consumption and mill capacity. In the case of power consumption, Morrell's model (Morrell, 1993) can be used to establish the effect radial segregation has on the mill power draw. The presence of a segregated layer of silica particles will most likely alter the efficiency with which energy is transferred from the mill shell to the load. The segregation of particles to the periphery of the charge will lead to a reduction in breakage rates of particles as fewer opportunities arise for the segregated particles to receive breakage action from the steel balls.

The core of the load being depleted of particles will also cause an increased chance of ball to ball contacts and hence increase the ball wear rate.

To quantify radial segregation using the inductive probe's signal the radial segregation index (σ) was defined as follows:

$$\sigma = 1 - \frac{\Delta V_{D,U}}{\Delta V_{D,O}} \qquad \textbf{4.1}$$

Where: $\Delta \mathbf{V_{D,U}}$ is the voltage drop in the inductive probes signal for a ball load with a specific particle filling and $\Delta \mathbf{V_{D,U}}$ is the voltage drop in the inductive probes signal for a ball-only load.

This index depends on the measuring range of the probe, in this case 5mm. For a ball displacement greater than or equal to 5mm from the probe's sensing surface, the radial segregation index will be 1. Otherwise, if no displacement occurs, the radial segregation index is about 0. Figure 4.7 shows the average radial segregation index variations with particle filling and mill speed for both coarse and fine particles. The error bars shown are equivalent to one standard deviation from the average. For purpose of clarity, the data points for mill speeds of 78% and 98% of the critical speed have been translated by 1% along the particle filling axis. The radial segregation index increases with coarse particle filling at a

constant mill speed. Similarly, the radial segregation index increases as the mill speed is increased at a constant coarse particle filling. At the mill speed of 98% of the critical, and for particle fillings between 60-80%, the segregation index drops. This is due to an increase in the amount of steel balls within the probe's sensing range. At particle fillings greater than 80%, the segregation index continues to rise to 0.97. This high segregation index signifies that a layer of particles 5mm thick was formed. No radial segregation occurred in the fine particle charge as the segregation index was below 0.1 for all particle fillings and speeds.

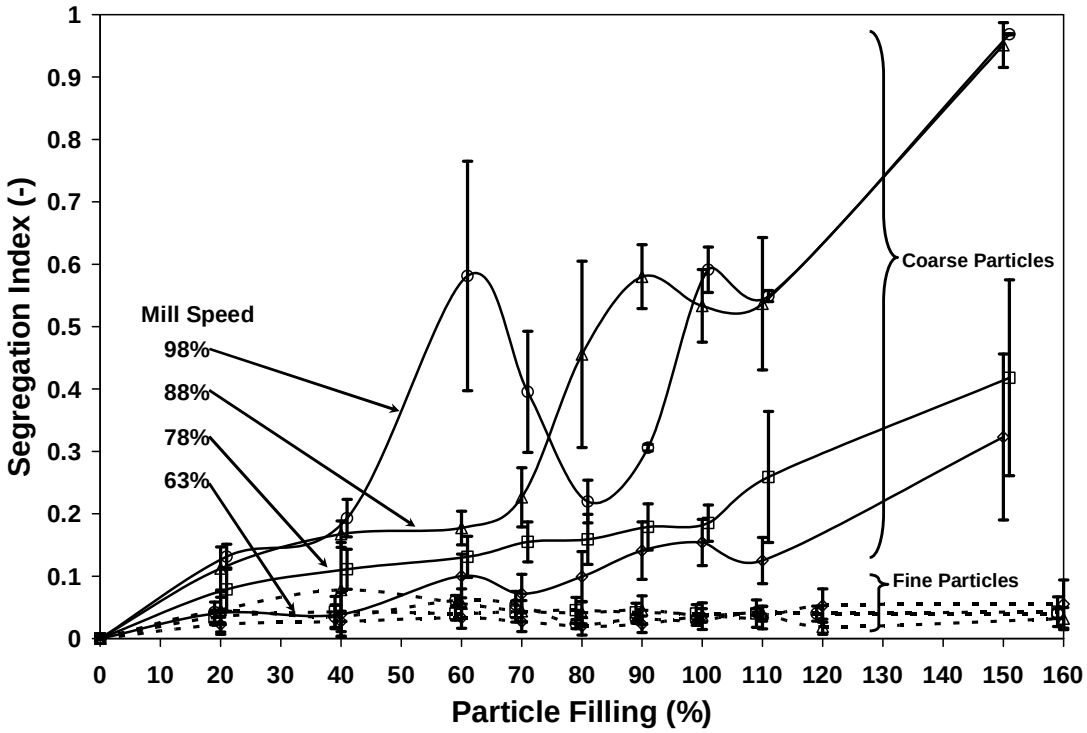


Figure 4.7: Effect of particle filling and mill speed on radial segregation

4.4 EFFECT OF REDUCING THE CHANGE IN PARTICLE SIZE DISTRIBUTION

In the above experiments, the particle size distribution changed considerably due to the grinding time being 15 minutes long despite fresh feed being added to attain the consecutive particle filling. An experiment was performed at 76% of the critical while maintaining the ball and particle filling as in the previous experiments. The total grinding time was 4mins for this experiment. The particle size distribution for the coarse silica sand changed from 50% passing 1102μm in the feed to 50% passing 1011μm at the end of the experiment. For fine silica sand it changed from 50% passing 173μm to 50% passing 141μm at the end of the experiment. The power draw, load orientation and inductive probe signal dependency on particle filling for both coarse and fine particles are seen in Figure 4.8. Shortening the grinding time causes the load behaviour trends (Figure 4.8b and 4.8d) and net power draw (Figure 4.8a) for both coarse and fine particle loads to be quite different from those obtained in previous experiments (Figure 4.3, 4.5a and 4.5d) at a similar mill speed. For coarse particles (Figure 4.8a) the power rises as the particle filling increases to 110% despite the shoulder's angular position remaining fairly constant at about 280^{o} (Figure 4.8b and 4.8c). The power then plateaus up to a particle filling of 160%. For fine particles, the power peaks between the particle fillings of 70-90% then drops rapidly due to excessive cataracting of balls on to the mill shell (Figure 4.8c and 4.8d).

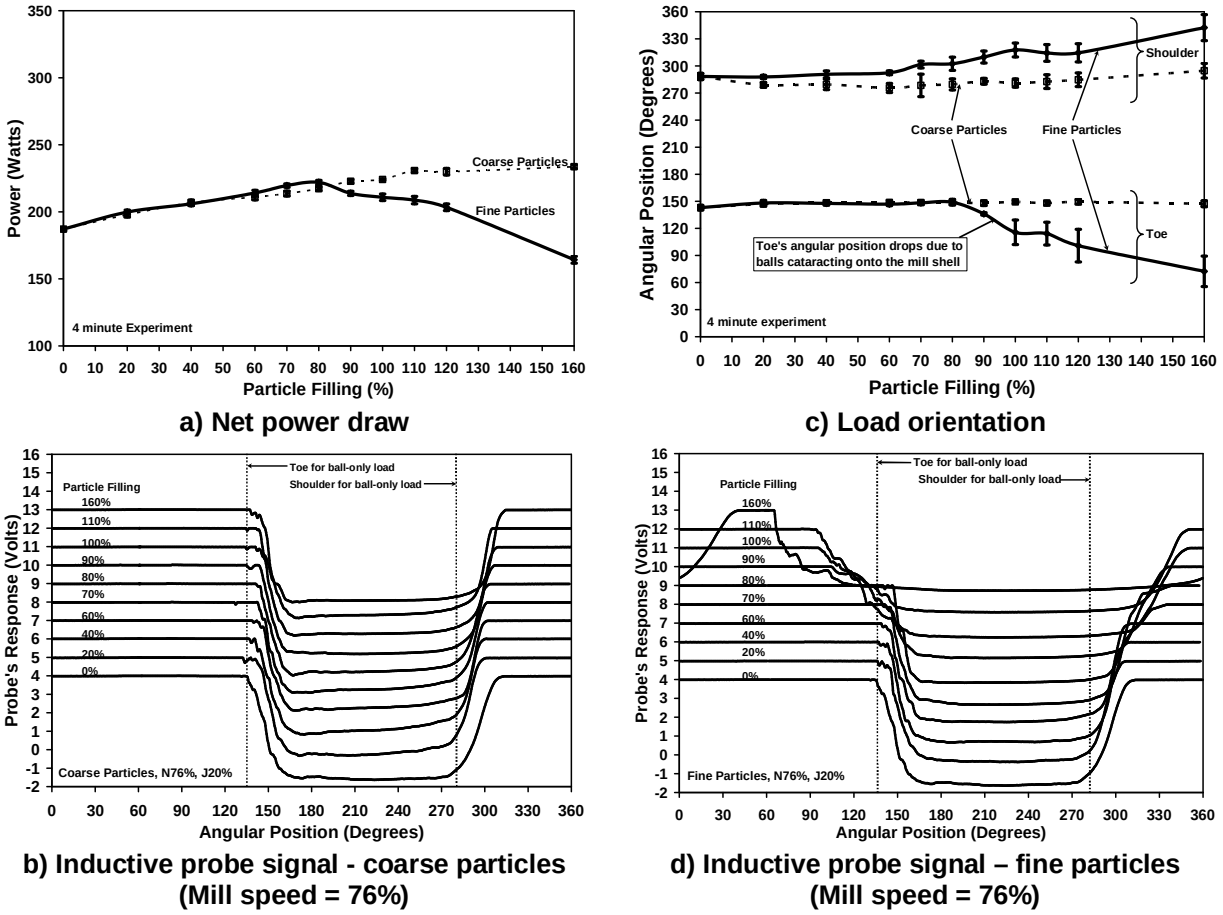


Figure 4.8: Net power, ball load orientation and Inductive probe signal as particle filling increases at 76% of the critical and a ball filling of 20%.

4.5 CONCLUSION

Increasing the coarse particle filling within the ball load without allowing for a considerable change in the particle size distribution due to grinding, does not cause the particles to have a great influence on the ball load orientation as seen in Figure 4.8b. In this case, the power increases as a result of the additional particle mass within the charge and lift imparted to

the ball charge by the particles. No substantial power loss was obtained for high particle fillings. Once a significant change in the coarse particle size distribution within the charge is experienced, the particles begin to interfere with the normal ball load behaviour as seen in Figure 4.4a, 4.5a, 4.5b and 4.6a. As deduced in this study, the shoulder position rises gradually with increasing particle filling until the onset of intense cataracting; after which the shoulder position increases rapidly to higher angular positions with rising mill speed and particle filling. Power will increase due to an increase in the charge mass and a rise in the shoulder's angular position. However, the power peak moves to lower particle fillings with increasing mill speeds. The primary source of power loss following a peak in power is the cataracting of balls onto the exposed mill shell. Strong radial segregation within the charge is experienced, where the silica particles segregate to the periphery thus allowing for easy measurement of this phenomenon. Radial segregation intensifies with increasing mill speed and particle filling.

A small change in the fine particle size distribution while increasing the particle filling causes fine particles to influence the ball load behaviour as seen in Figure 4.8d. There is a notable increase in cataracting of the charge onto the mill shell accompanied with a drastic drop in the mill's power. If a substantial change in the fine particle size distribution is allowed, the shoulder position tends to slump slightly with increase in the mill speed and particle filling as seen in Figure 4.4c, 4.5d and 4.5e. No

cataracting of the charge onto the exposed mill shell is observed. At high mill speeds, the load centrifuges at low particle fillings accompanied by a decrease in the mill power draw as seen in Figure 4.6c and 4.6d respectively. No radial segregation is detected for a load containing fine particles.

The measurements obtained using the inductive probe demonstrates its ability to detect various conditions that arise within grinding mills such as cataracting, centrifuging and segregation. This technique of measuring load behaviour holds much promise in becoming a tool to validate computer aided load behaviour models such as the Discrete Element Model (DEM) using experimental data.

CHAPTER 5

MODELLING STUDY 1

Modelling of particle filling and size effects on the load behaviour and power in a dry pilot mill: Morrell's C Model

Morrell's C model was used to simulate the experimental data obtained from the experimental study of the effects of particles on the ball load behaviour and power. A further understanding of the effects that coarse particles and fine particle have on the mill power has been realised. For coarse particles it was necessary to modify Morrell's definitions of the toe and shoulder angular positions to account for their variations with particle filling. Furthermore, the effects of redial segregation, centrifuging of the coarse particles have been incorporated into Morrell's model to form the segregated charge model and the centrifuged charge models. While for fine particles beyond fillings of 100%, neither the load expansion models nor the particle pool formation model could account for the power loss at these particle fillings. A compromise between the two models brought about an improved model for the mill power.

5.0 INTRODUCTION

Mill power has a complex non-linear relationship with most of the factors that affect it such as mill speed and load filling etc. Having good power models to predict a mill's power draw has been the focus of many researchers in the past century. Accurate power models can be used in mill design, mill control and optimisation.

The basis of most power model development is the description of the load behaviour. The more realistic the load behaviour description is to reality the more accurate the power model becomes and likewise the more complex it becomes as it will involve more details on the internal mechanics of the load. Power models based on simplified load behaviour shapes such as Bond's (1960b), Fuerstenau et al (1990), Moys (1993) and Morrell (1993) have been used to estimate power draws of various mills. The simplified load behaviour shapes represent the load as a solid mass that is well mixed and cannot account for all the factors affecting the load mass e.g. liner profile, slurry viscosity, segregation etc. These power models are empirical. The development of the Discrete Element Method (DEM) in milling (Mishra & Rajamani, 1992) has led to a more robust model that is capable of simulating a mill's load behaviour based on the internal mechanics of the load as affected by various factors and has enhanced mill power predictions. The load is treated as a discrete mass of particles interacting with each other and their environment. Each particle

in the simulation is tracked and relevant information of the particle stored per unit time. The particle interactions are modelled using Newton's laws of motion and the linear spring-slider-dashpot model used for particle contact modelling. The DEM can be coupled with other models such as Computational Fluid Dynamics, Discrete Grain Breakage, Multi-Phase flow and Finite Element Methods to enhance the realism of the simulations. Validation data for the DEM is always scarce thus caution should be taken when using invalidated simulation data.

The study below makes use of Morrell's C-model to model the various conditions that arose in the experiment conducted in Chapter 4.

5.1 MORRELL'S MODEL

Morrell (1993) conducted an experimental study on the evolving load behaviour as a function of mill speed, mill filling and lifter type in a laboratory mill of diameter:300mm and length:150mm. Morrell approximated the shape of the load to be equivalent to a C shape as seen in Figure 5.1. The physical limits of the charge are defined by radial lines that extend from the toe (θ_T) and shoulder (θ_{Sh}) to the mill's centre, the charge inner surface radius (r_i) and the mill's internal radius (r_m). Morrell assumed his load to be well mixed.

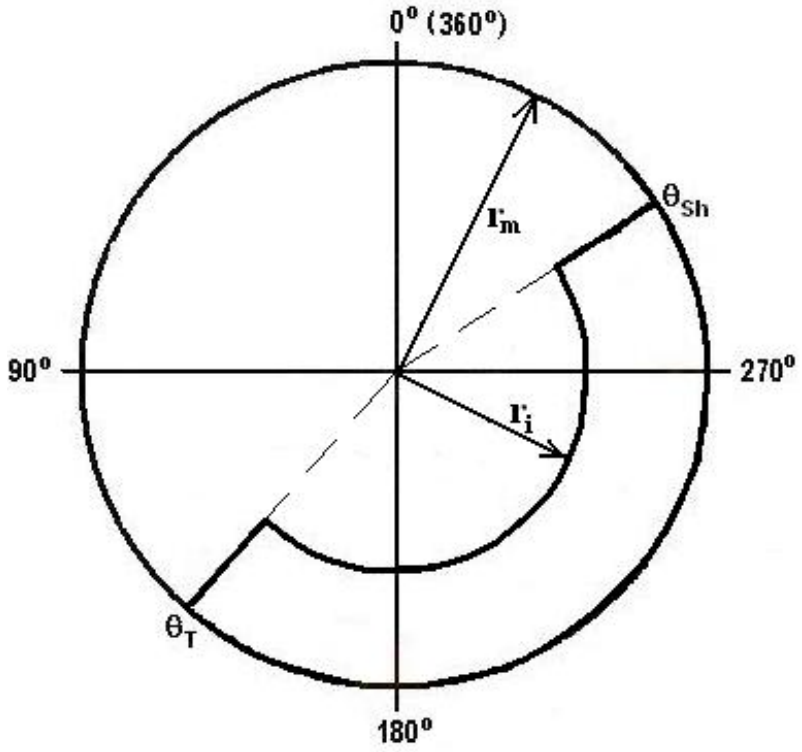


Figure 5.1: Morrell's C load behaviour model description

Morrell's C model incorporated the definition of the shape and motion of the charge through an empirical definition of the toe and shoulder angular positions which are functions of the load filling (J) and mill speed (N). The approach used to derive Morrell's model is based on the rate at which potential energy and kinetic energy are generated within the charge. Morrell's power model and the physical limits of the load can be summarized as follows:

Net power draw (P_{net}):

$$P_{net} = \left[\frac{\pi g L \rho_c N_m r_m}{3(r_m - z r_i)}\{2r_m^3 - 3z r_m^2 r_i + r_i^3(3z-2)\}\{\sin\theta_S - \sin\theta_T\}\right] +$$

$$\left[L\rho_c\left\{\frac{N_m r_m \pi}{(r_m - z r_i)}\right\}^3\{(r_m - z r_i)^4 - r_i^4(z-1)^4\}\right] \qquad \textbf{5.1}$$

Where: $z = (1 - J_t)^{0.4532}$

Toe's angular position (θ_T):

$$\theta_T = A\left(1 - e^{-B(\emptyset_c - \emptyset)}\right) + \frac{\pi}{2} \quad \textbf{5.2}$$

Where A and B are parameters determined by regression analysis.

Shoulder's angular position (θ_S):

$$\theta_S = \frac{\pi}{2} - \left(\theta_T - \frac{\pi}{2}\right)(E + FJ_t) \quad \textbf{5.3}$$

Where E and F are parameters determined by regression analysis.

Charge inner surface (r_i):

$$r_i = r_m\left[1 - \left(\frac{2\pi\beta J_t}{2\pi + \theta_{Sh} - \theta_T}\right)\right]^{0.5} \quad \textbf{5.4}$$

Where: **g** is the acceleration due to gravity (m/s^2), **L** is the mill's belly length (m), ρ_c is the density of the charge (Kg/m^3), N_m is the mill's speed (rpm), r_m is the mill's radius (m), J_t is the mill's filling and β is the fraction of charge bound by the toe, shoulder and the charge inner surface.

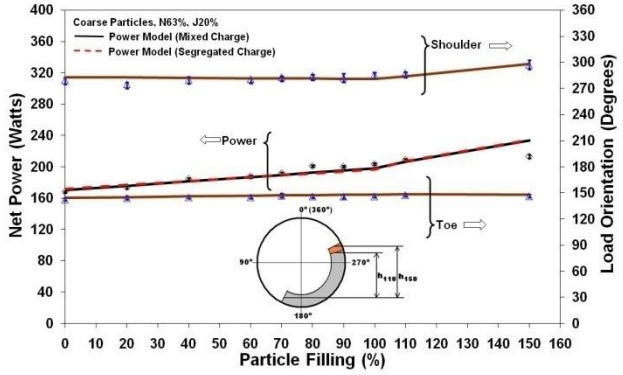
5.2 ANALYSIS AND DISCUSSIONS

Morrell's C model was used to model the experimental data (Morrell, 1993). The attractiveness of this model is that it incorporates empirical

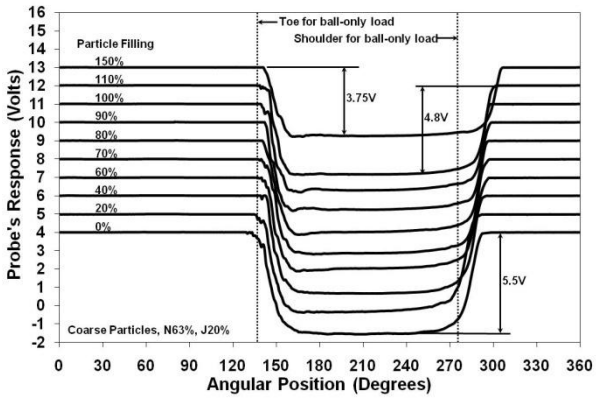
definitions of the load behaviour via its toe, shoulder and the charge inner surface models. The model has been modified so as to be used in situations where segregation and centrifuging of the load occur. No attempts were made to account for loss in power due to the cataracting charge striking the exposed mill shell. As a result the model is not expected to fit all of the experimental data. It is anticipated that this modelling exercise will result in a further understanding of how particles affect the load behaviour and subsequently the mill power draw.

5.2.1 MODELLING OF THE COARSE PARTICLE EFFECTS

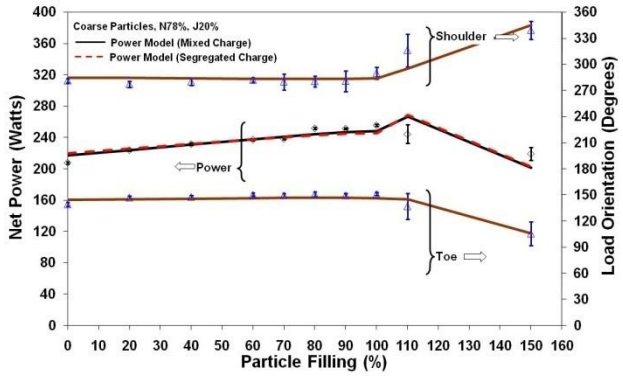
The load orientation, power and the inductive probe average signal for the mill speeds of 63% and 78% of the critical speeds are shown in Figure 5.2. Initially all the experimental results were modelled based on Morrell's mixed charge model that has been described in detail in Appendix A2.1. The toe's angular position for a mill speed of 63% of the critical speed remains constant (Fig. 5.2a) while that of 78% of the critical varies with particle filling increment (Fig. 5.2c). The shoulder's angular position varies with an increase in coarse particle filling for both the mill speeds of 63% and 78% of the critical. An account of this variation of load behaviour with particle filling increment has to be included in Morrell's toe and shoulder model.



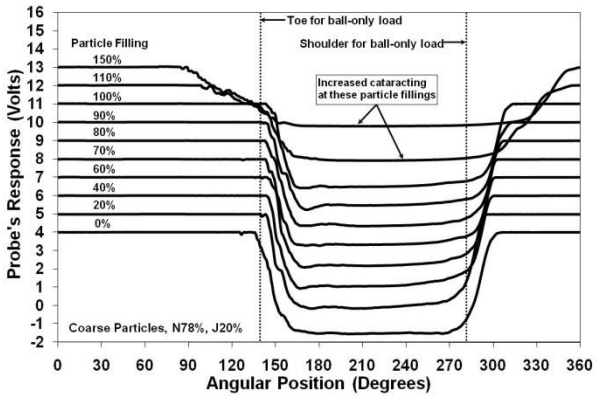
a) Load orientation and power model – Coarse Particles (Mill speed = 63%)



b) Inductive probe signal - Coarse Particles (Mill speed = 63%)



c) Load orientation and power model – Coarse Particles (Mill speed = 78%)



d) Inductive probe signal - coarse particles (Mill speed = 78%)

Figure 5.2: Load orientation, power and the inductive probe average signal for the mill speeds of 63% and 78% of the critical

The proposed definition of the toe and shoulder are as follows:

Toe (θ_T):

$$\theta_T = (A + BN + CU)\left(1 - e^{-\beta((D+EN)-U)}\right) \quad \textbf{5.5}$$

Shoulder (θ_{Sh}):

$$\theta_{Sh} = 2\pi - (F - GU)\theta_T \quad \textbf{5.6}$$

Where: **A**, **B**, **C**, **D**, **E**, **F** and **G** are parameters determined by regression analysis, **U** is the particle filling (%), **N** is the mill's speed (%).

Equations 5.5 and 5.6 have been adapted to be compatible with a coordinate system that has 0^o at the 12 o'clock position and increments anticlockwise to 360^o. Morrell's coordinate system had 0^o at the 3 o'clock position and increments anticlockwise to 360^o. Equations 5.5 and 5.6 predict the toe and shoulder angular positions adequately for the mill speed of 63% and 78% of the critical speed (Fig. 5.2a and Fig. 5.2c).

For the mill speed of 63% of the critical speed, the mixed charge power model was capable of modelling adequately the power draw up to a particle filling of 110% as seen by the black solid line in Fig. 5.2a. Above the particle filling of 110% the model overestimates the power draw due to the shoulder's angular position rising while the toe's angular position remains constant. The picture insert in Fig. 5.2a shows the potential energy states of the charge at the particle filling of 110% (gray) and 150% (red). The increase in the shoulder's angular position for the particle filling of 150% causes an increase in the potential energy calculated via Morrell's model by 15% thus causing an increase in the simulated power by a similar amount.

Significant radial segregation of the coarse silica sand occurred at the particle filling of 150% as compared to the particle filling of 110%. Radial

segregation is detected by the inductive probe when a significant difference in the probe's voltage drop results as particle filling increases (Fig. 5.2b). The inductive probe response for the particle filling of 110% drops by 4.8V which corresponds to a 13% less drop in the voltage signal when compared to a balls only load while for a particle filling of 150% the voltage drops by 3.75V and corresponds to a 32% difference in voltage drop. It is possible that at the particle filling of 150% the segregated silica particles have more influence on the outermost ball layer close to the mill shell and in contact with the segregated silica sand layer thus causing an increased lift of the balls in this layer as compared to the inner layers hence a higher shoulder position. If this is the case then the angular position measured by the probe is not an accurate representation of the shoulder's angular position for the bulk of the charge. As a result of this segregation occurring in the charge, Morrell's model had to be modified to reflect a more realistic situation. The segregated charge power model shall be discussed in more detail under the section 5.2.2.

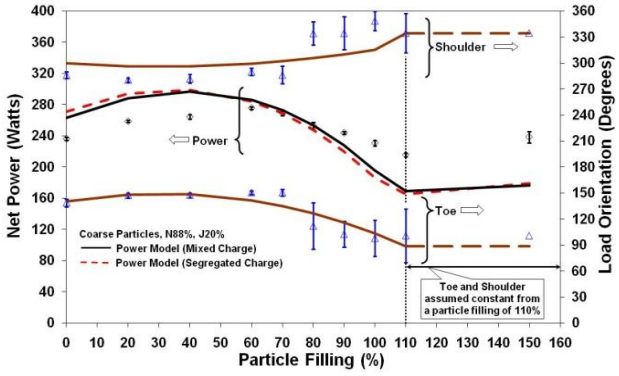
At 78% of the critical speed the mixed charge model was capable of modelling adequately the mill's power draw up to a particle filling of 100%. Beyond the particle filling of 100%, the model does not model the power drawn by the mill accurately despite the toe and shoulder angular positions being predicted within one standard deviation (Fig. 5.2c). Above a particle filling of 100% an increase in cataracting is experienced by the load (Fig. 5.2d). The increase in cataracting is due to an increase in the influence of

silica sand particles on the outermost ball layer close to the mill shell thus leading to a higher shoulder angular position. The toe's angular position is affected by the cataracting of balls thus making it difficult to measure the correct angular position for the toe. The angular position of the load's bulk toe represents the angular position of the majority of balls in the toe and is the correct value to be used to calculate the power draw using Morrell's model. Moreover, no attempts were made to include the energy given up by the cataracting portion of the load to the exposed mill shell in Morrell's power model. This energy would decrease the net power required to drive the mill.

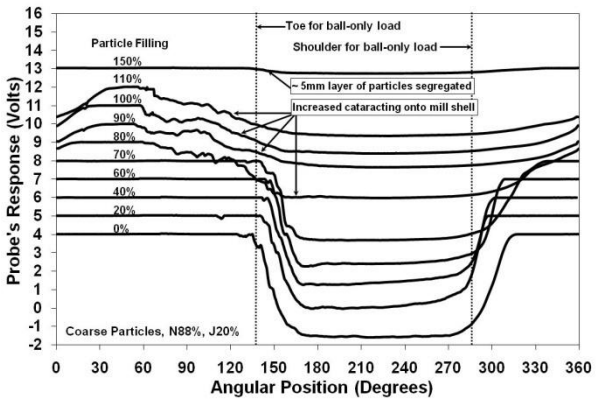
The inductive probe signal, load behaviour and power modelling for the mill speeds of 88% and 98% of the critical speed can be seen in Figure 5.3. For 88% of the critical mill speed, as in Figure 5.3a, Morrell's model was capable of modelling adequately the toe's angular positions. The toe and shoulder angular positions for both the experiments and model at the particle filling of 150% are assumed to be equal to that obtained for the particle filling of 110%, as shown in Figure 5.3a, due to the fact that a 5mm layer of segregated silica sand shields the inductive probe from detecting the steel balls.

The trend of the mixed charge power model (solid line as seen in Figure 5.3a) with particle filling increment is in line with that of the experimental power variation with particle filling increment. For particle fillings less than

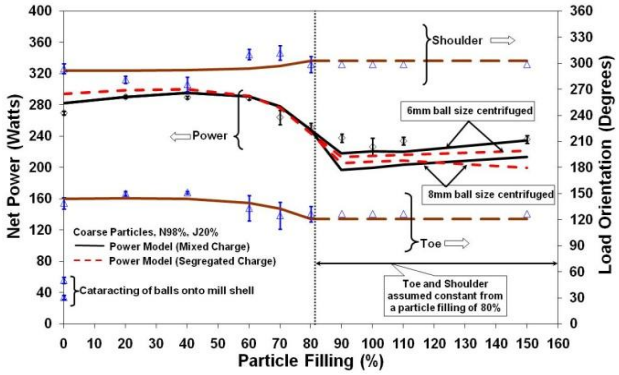
60%, the model over estimates the power by 11-14%. This is due to the model not being able to model adequately the experimental shoulder's angular position and thus over estimating it by 15 degrees. For particle fillings less than 60%, the potential energy obtained from Morrell's power model using the model's toe and shoulder values is on average 14.5% more than that obtained when using the experimental toe and shoulder values in the power model.



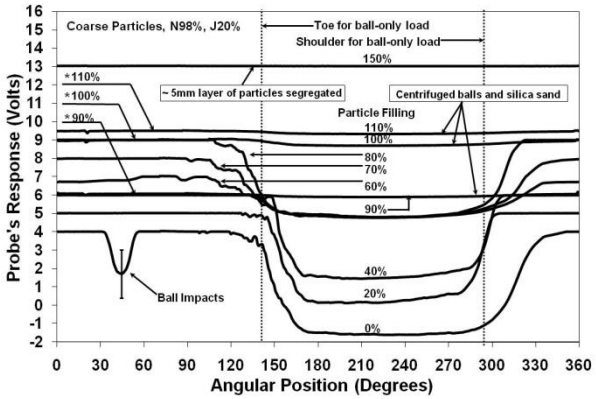
a) Load orientation and power model – Coarse Particles (Mill speed = 88%)



b) Inductive probe signal - Coarse Particles (Mill speed = 88%)



c) Load orientation and power model – Coarse Particles (Mill speed = 98%)



d) Inductive probe signal - coarse particles (Mill speed = 98%)

Figure 5.3: Load orientation, power and the inductive probe average signal for the mill speeds of 88% and 98% of the critical

For the particle fillings of 60 – 80%, Morrell's model was capable of modelling adequately the experimental power. At particle fillings greater than 80%, Morrell's model is 9-26% lower than the experimental power. Figure 5.3b shows significant cataracting experienced at the particle fillings between 80 – 110% hence this will have an impact on the inductive probe's accuracy in measuring the bulk toe position.

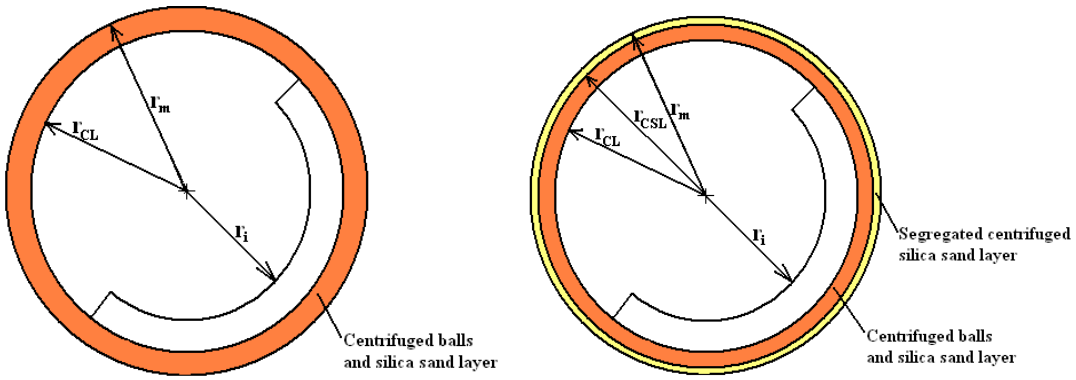
At 98% of the critical mill speed (Figure 5.3c) Morrell's toe and shoulder model was capable of modelling adequately the experimental load behaviour up to the particle fillings of 80%. For the particle fillings of 90-150% the toe and shoulder angular positions were assumed to be the same as the values for the particle filling of 80%. This assumption does not cause any deterioration to the model trend as it is quite similar to that of the experimental power trend (solid lines as seen in Figure 5.3c). For the ball only load (U = 0), the mixed charge power model (solid lines as seen in Figure 5.3c) over estimates the experimental power by 5%. The inductive proximity probe load behaviour response for these mill speeds (Figure 5.3d) shows that balls were detected in the 30-60^{o} angular positions indicating cataracting of balls onto the exposed down coming mill shell. This cataracting would be accompanied by a loss in mill power draw. Morrell's model does not account for this energy loss and thus would result in the model overestimating the power drawn by the mill. The power model for the mixed charge model (solid lines as seen in Figure 5.3c) was

capable of modelling the experimental power adequately up to a particle filling of 80%.

The arrows in Figure 5.3d identified by an asterisk beside the particle fillings of 90%, 100% and 110% show the expected position of the inductive probe's signal (as if no balls were in contact with the probe) and its subsequent drop during the mill revolution. A drop in the inductive probe's signal to a low voltage state over a full mill revolution indicates that some balls have centrifuged for these particle fillings. For the particle filling of 150% it is assumed that a 5mm layer of silica particles centrifuged with balls. Looking at the length of the arrows in Figure 5.3d it is evident that as particle filling increases more particles are centrifuged with balls up to the an extent of about a 5mm layer of particles is centrifuged at a particle filling of 150%.

A centrifuged charge model was drawn up using Morrell's C model as described in Appendix A2.2. Both the mixed and segregated centrifuged charge models were used. In the mixed centrifuged charge model it is assumed that the centrifuged layer contains well mixed balls and silica sand particles (Figure 5.4a) while for the segregated centrifuged charge model it is assumed that a segregated layer containing silica particles will centrifuge beneath the ball layer (Figure 5.4b). The power calculated here is only for the active charge while the centrifuged charge draws no power. The mill radius will be reduced by the thickness of the centrifuged layer.

The centrifuged layer also affects the load density, ball filling and particle filling. In the power modelling for the particle fillings of 90-150% a comparison was made between the assumptions that either a layer of 6mm balls (smallest ball size) or 8mm balls (average ball size) centrifuged. For the mixed charge model (solid lines as seen in Figure 5.3c) at the particle fillings of 90 – 110%, the model was capable of modelling adequately the experimental power under the assumption of a 6mm ball layer being centrifuged as compared to an 8mm ball layer.



a) Mixed centrifuged charge model **b) Segregated centrifuged charge model**

Figure 5.4: Centrifuging of the charge for both segregated and mixed charge conditions

5.2.2 MODELLING THE EFFECTS OF RADIAL SEGREGATION

Through the experimental study in chapter 4, it was shown that the intensity of radial segregation within the coarse particle charge increases with particle filling and mill speed. In this experimental study only one inductive proximity probe was used and this would result in the possibility that the radial segregation being detected was localised. Through studying the inductive probe's signal for individual mill revolutions it was seen that

the radial segregation occurred at various degrees of intensity per mill revolution. Since no load behaviour pictures were taken while conducting the experiments an investigation was initiated to study the occurrence of radial segregation within the coarse particle charge in a small plastic batch mill of diameter 246mm and length 45mm. Square lifters of height 10mm were installed in the plastic mill. Ball sizes of 6, 7, 8, 9 and 10mm were mixed together equally in number to a ball filling of 20% of the mills internal volume.



N:63%, U:40% **N:74%, U:40%** **N:85%, U:40%**

a) Radial segregation sensitivity with mill speed



N:85%, U:20% **N:85%, U:40%** **N:85%, U:100%**

b) Radial segregation sensitivity with particle filling

Figure 5.5: Variation of coarse particle radial segregation with mill speed and particle filling at the ball load of 20%.

It can be seen in Figure 5.5 that the segregation of the coarse silica particles occurs at the periphery of the load in contact with the mill shell. The intensity of the radial segregation increases with increasing mill speed (Figure 5.5a) and likewise with increasing particle filling (Figure 5.5b). A well mixed charge would result at the lower speeds where the charge falls onto the free surface of the charge and particles would then be trapped in between the balls in the fluidised free surface of the charge. A segregated charge comes about when most of the silica particles are thrown clear of the charge and build up between lifters before it enters the toe of the load. Interestingly enough one can see from Figure 5.5 that radial segregation of the steel balls by size did occur with most of the large 10mm balls being concentrated at the centre of the load.

Being able to detect segregation availed an opportunity to account for the effects that radial segregation had on the mill power draw through Morrell's model. Morrell's C model was split into two parts as seen in Figure 5.6. The outer portion of the charge was assumed to contain a uniform layer of silica sand while the inner layer was comprised of a charge of steel balls and silica sand with a reduced particle filling. The interface separating the two layers defines the physical limit of the outer segregated layer. This interface location can be determined by multiplying the radial segregation index with the measuring range of the inductive proximity probe in this case 5mm.

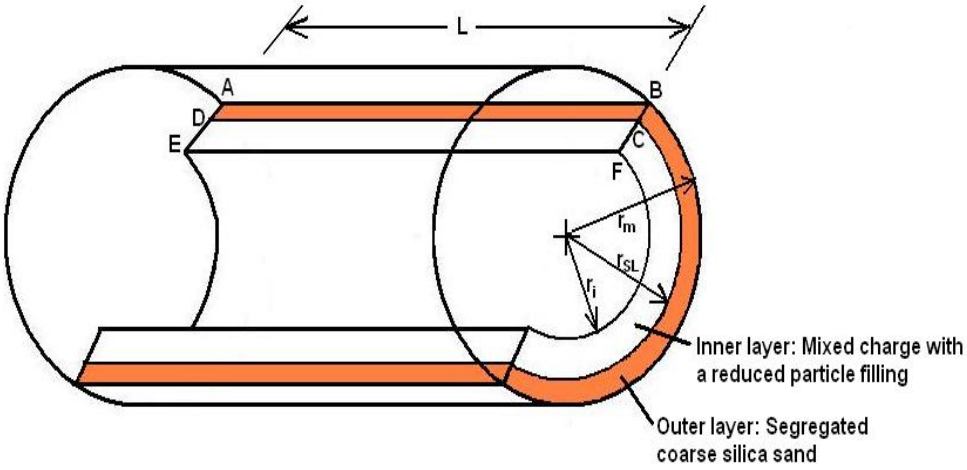


Figure 5.6: Illustration of the radial segregation charge model

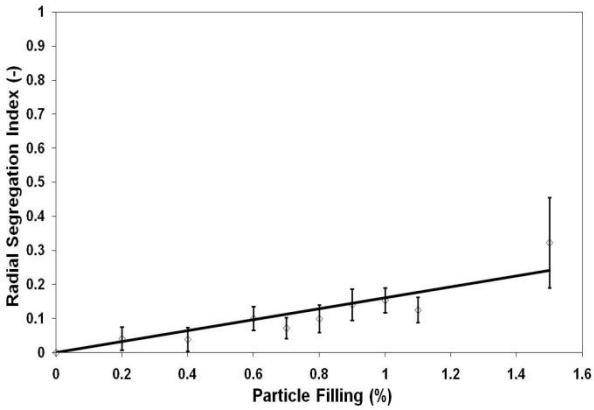
The radial segregation index is defined below as:

$$\sigma = 1 - \frac{\Delta V_{D,U}}{\Delta V_{D,0}} \qquad \textbf{5.7}$$

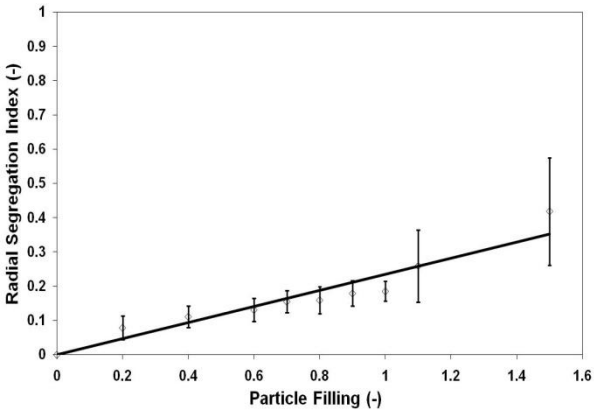
Where: $\Delta V_{D,U}$ is the voltage drop in the inductive probes signal for a ball load with a specific particle filling and $\Delta V_{D,U}$ is the voltage drop in the inductive probes signal for a ball-only load.

The plot of the radial segregation index as a function of particle filling and mill speed is seen in Figure 5.7. Here it is seen that the radial segregation index increases with particle filling and mill speed. A radial segregation index of 0 means that no segregation occurred while that of 1 means that a 5mm layer of segregated silica sand was formed. Linear models were fitted to the radial segregation index so as to obtain a mathematical

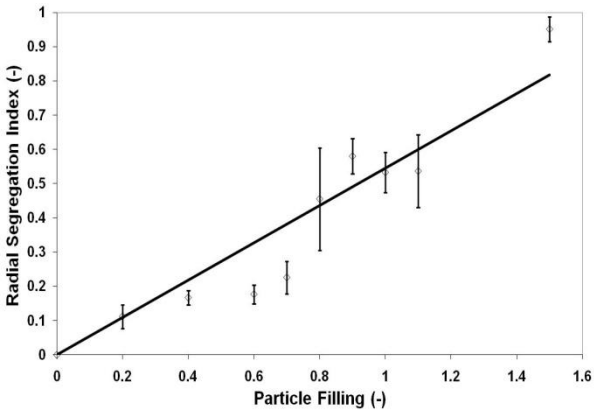
description of the segregation process. The error bars reflect the variation of the segregated layer. It can be seen that at the mill speeds of 63% and 78% of the critical (Figure 5.7a & Figure 5.7b) there was substantial variation in the thickness of the layer particularly at high particle fillings while for the mill speeds of 88% and 98% of the critical (Figure 5.7c & Figure 5.7d) less variation occurred at particle fillings greater than 100%. It is most likely that at the speed of 88% and 98% of the critical a more stable segregated layer is formed for high particle fillings.



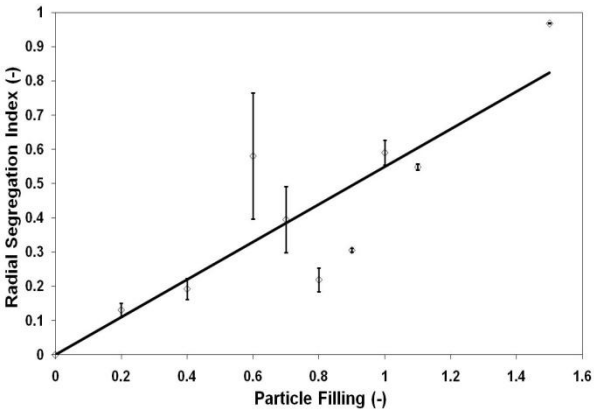
a) Radial segregation index (Mill speed = 63%)



b) Radial segregation index (Mill speed = 78%)



c) Radial segregation index (Mill speed = 88%)



d) Radial segregation index (Mill speed = 98%)

Figure 5.7: Modelling the variation of the radial segregation index with particle filling for various mills speeds

The relationship between the radial segregation index and particle filling for all speeds are defined below:

63% of critical mill speed:

$\sigma = 0.161U$ **5.8**

$r^2 = 0.824$

78% of the critical mill speed:

$\sigma = 0.235U$ **5.9**

$r^2 = 0.91$

88% and 98% of the critical mill speed:

$\sigma = 0.55U$ **5.10**

$r^2 = 0.761$

Calculating the model power was based on the summation of the power drawn by the two layers formed as described in Appendix A2.3 and it is assumed that they is no loss in rotational speed between the two layers. When calculating the power of the inner layer the amount of silica particles in this layer should be reduced by an equivalent amount of silica particles in the outer segregated layer. The density of the inner layer will have to be recalculated to take into account a lower particle filling in this layer. For all the mill speeds (63 – 98% of the critical) as seen in Figure 5.2a, 5.2c, 5.3a and 5.3c, the power drawn by the mill was modelled based on a mixed

charge model and a segregated charge model. The solid line corresponds to the mixed charge model while the broken line corresponds to the segregated charge model. At the lower mill speeds of 63% and 78% of the critical there is no difference between the powers calculated by either the mixed or segregated charge models. This is most likely due to the outer layer comprised of silica sand not being thick enough and of a lower density as compared to the inner layer thus the power calculated for this outer layer by the power model cannot cause a substantial difference in power when the two charge models are considered. For higher mill speeds of 88% and 98% of the critical there is an 8 and 11% difference respectively between the powers calculated by the mixed and segregated charge models.

Of importance to be learnt about radial segregation is that it can influence the load behaviour substantially. In this case increased cataracting came about partly due to the fact that the segregated silica sand encouraged more lift in the outer layer of balls at high particle fillings as seen in Figure 5.2d and 5.3b and for high mill speeds such as 98% of the critical centrifuging of the load resulted as seen in Figure 5.3d. Cataracting and centrifuging are known to be accompanied by a loss in power drawn in tumbling mills and for these experiments a shift in maximum power to a lower particle filling. If a mill was to operate at this low particle filling increased ball wear would result as most of the balls would be concentrated to the middle of the charge with very little particles presents

in the void spaces as seen in Figure 5.5b. The grinding kinetics will also be affected as they will be less breakage resulting due to reduced chances of ball-ore contact and most likely this would be accompanied by a loss in product throughput. Operating the mill at speeds where more mixing of the charge results is to be encouraged and possibly designing liners that would throw the charge onto the free surface of the load as this would encourage mixing.

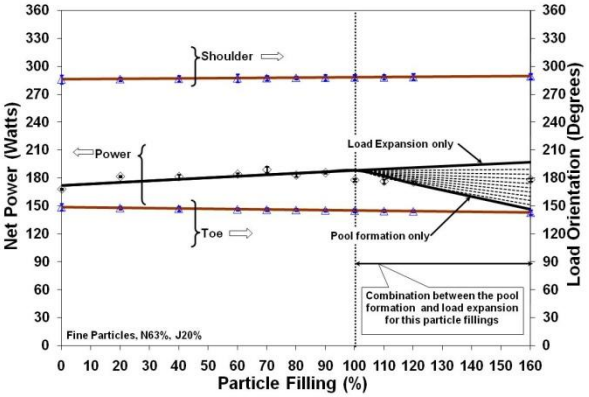
5.2.3 MODELLING OF THE FINE PARTICLE EFFECTS

The inductive probe signal, load behaviour and power modelling for the mill speeds of 63, 78% and 88% of the critical speed can be seen in Figure 5.8. For the fine particle case at the mill speeds of 63%, 78% and 88% of the critical speed as in Figure 5.8a, 5.8c and 5.8e respectively, the toe and shoulder angular positions do not vary with particle filling. The toe and shoulder models were left as defined by Morrell (1993).

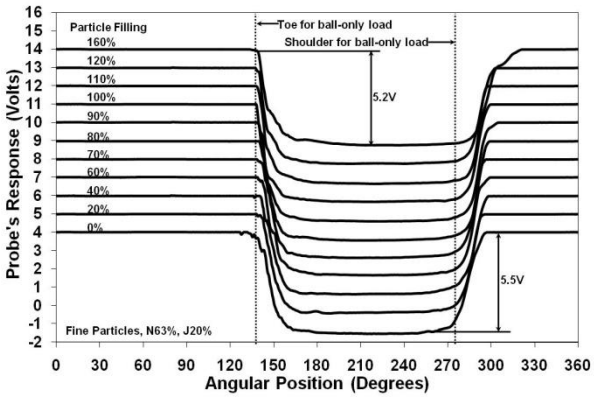
Essentially the form depicts that the toe and shoulder angular positions only vary with mill speed and load filling which is similar to the fine particle load behaviour case. In this case no radial segregation occurs in the load as the extent in voltage drop for a balls only load (particle filling = 0%) compared to a load with a particle filling of 150% are similar as indicated in Figure 5.8b. Morrell's mixed charge power model (Appendix A2.1) was capable of modelling adequately the mill's power draw up to a particle filling of 100% for the mill speeds between 63% and 88% as in Figure

5.8a, 5.8c and 5.8e. Beyond the particle filling of 100% the load expansion and pool formation models were incorporated into Morrell's model and used to account for power loss in the mill. In the modelling of power for particles greater than 100% it is assumed that the excess volume of particles above the volume that correspond to a particle filling of 100% can either go to expanding the load or forming a pool comprised of fine silica particles only or it can be split between pool formation and load expansion in some pre-defined ratio.

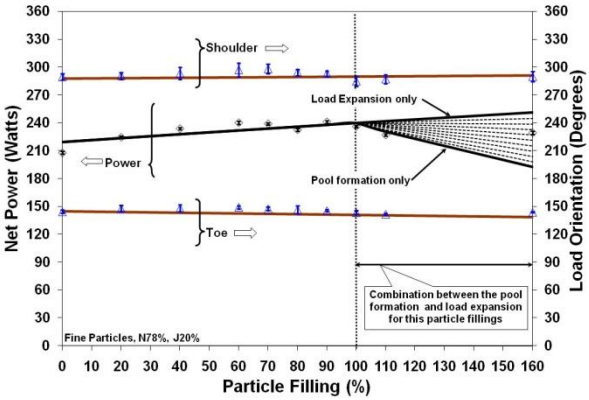
For **load expansion** the volume of the load increases thus this results in the total load filling increasing and a corresponding drop in the density of the load (Appendix A2.1). For ball mills operating under normal conditions it is usual to take the total mill filling to be equal to the ball filling though in the case where the mill was overfilled a total filling was considered which included the fractional volume of the mill that the balls occupied plus the excess volume of particles above a particle filling of 100%. Morrell's power model has a strong dependency on the mill filling and this is displayed by the mill power modelled by for the load expansion model increasing with particle filling (Figure 5.8a, 5.8c & 5.8e) despite a 16% drop in the load density from the particle filling of 100% to 160%. Under an exclusive load expansion model the mill's power draw was overestimated.



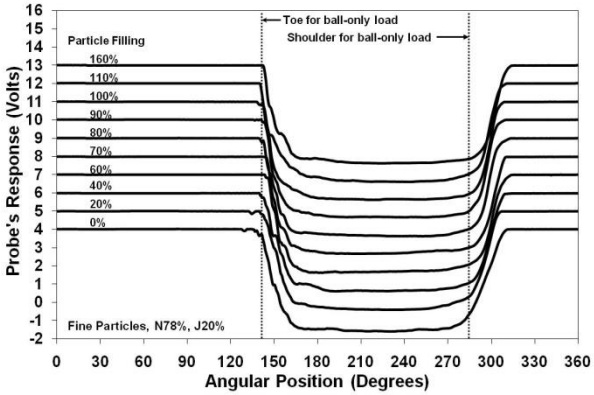
a) Load orientation and power model – Fine Particles (Mill speed = 63%)



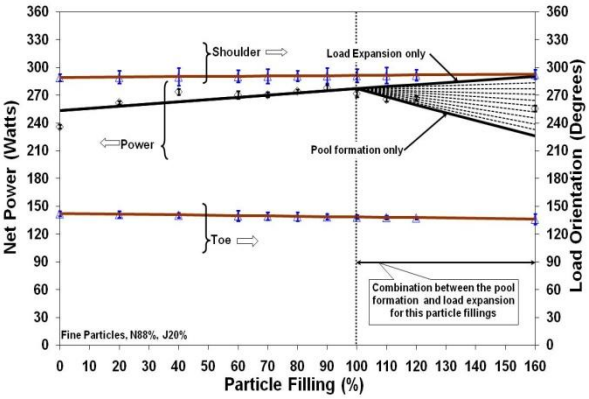
b) Inductive probe signal - Fine Particles (Mill speed = 63%)



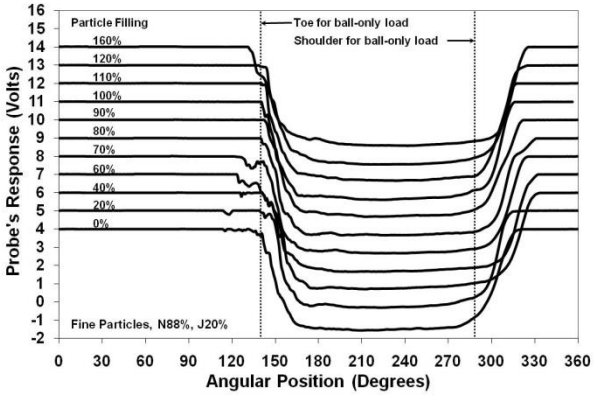
c) Load orientation and power model – Fine Particles (Mill speed = 78%)



d) Inductive probe signal - Fine Particles (Mill speed = 78%)



e) Load orientation and power model – Fine Particles (Mill speed = 88%)



f) Inductive probe signal - Fine Particles (Mill speed = 88%)

Figure 5.8: Load orientation, power and the inductive probe average signal for the mill speeds of 63%, 78% and 88% of the critical

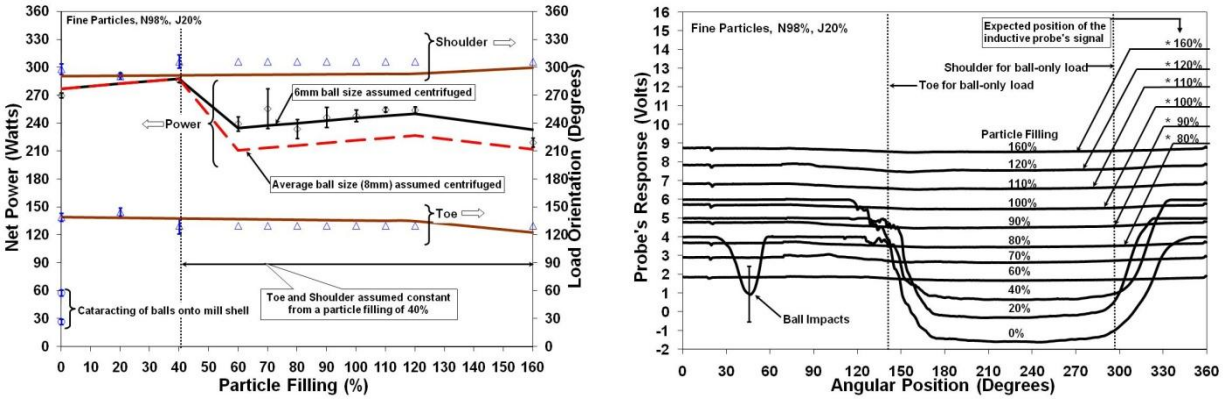
For the **pool formation** case a pool made up of silica particles only was generated using numerical methods as described in Appendix A2.4. The pool's volume is calculated by gradually incrementing the pool's height in the Simpson's method up to where the resulting pool volume is equal to the volume of excess particles above the particle filling of 100%. The location of the centre of gravity of the pool is then calculated from the resulting pool shape together with its corresponding torque and power draw. The pool's power draw is then reduced from the net power draw calculated by Morrell's power model for the rest of the load. Here the load is assumed to remain at a constant load volume of 20% and its density remains constant for the particle fillings of 100 – 160%. Under the pool formation model the mill's power draw is under estimated. As the mill speed is increased the experimental power tends to lean towards pool formation rather than load expansion. This then led to considering modelling a ratio split between load expansion and pool formation.

For the **ratio split between load expansion and pool formation** the excess volume of particles above a particle filling of 100% is split in increments of 10% between the volume of particles contributing to load expansion and the volume of particles that contribute to pool formation. A typical example would be 90% of the excess volume of particles going to load expansion and 10% going to pool formation and the percentage contribution is adjusted by 10% for the next power calculation (i.e. the next step would be 80% load expansion and 20% pool formation). At 63%

of the critical mill speed the experimental power at the particle filling of 150% lies between the ratio split of 40:60 and 30:70 (pool formation: load expansion) as seen in Figure 5.8a, while for the mill speed of 88% the experimental power lies between the ratio split of 60:40 and 50:50 (pool formation: load expansion) as seen in Figure 5.8e. Increasing the mill speed would most likely cause a larger pool to be formed. It can be seen that taking the ratio split into account one can model the power drawn by the mill more accurately than a model that is based on load expansion only or pool formation only.

Figure 5.9 shows the inductive probe signal, load behaviour and power modelling for the mill speed of 98% of the critical speed. Above the particle filling of 40% the load centrifuged as indicated in Figure 5.9b by the asterisk on the corresponding particle fillings. No toe and shoulder angular positions were obtained for these particle fillings thus it was assumed that for the purpose of power modelling the toe and shoulder angular positions will be the same as that obtained from the particle filling of 40%. For the particle fillings between 0 - 40%, Morrell's mixed charge model (Appendix A2.1) was used to calculate the power draw. The model estimates the power well. In the power modelling for particle filling greater than 40% the mill's power draw was modelled using the mixed centrifuged charge model described in Appendix A2.2 as no radial segregation of particles occurred. It was assumed that either a 6mm ball layer centrifuged that corresponds to the smallest ball size or an 8mm ball layer centrifuged that corresponds

to an average ball size. The solid line in Figure 5.9 corresponds to the 6mm ball layer centrifuging while the broken line corresponds to the 8mm ball layer centrifuging. Under the assumption of a 6mm ball layer centrifuging the experimental power draw was modelled adequately while under the assumption of an 8mm ball layer centrifuging the power draw was under estimated.



a) Load orientation and power model – Fine Particles (Mill speed = 98%)

b) Inductive probe signal - Fine Particles (Mill speed = 98%)

Figure 5.9: Load orientation, power and the inductive probe average signal for the mill speeds of 98% of the critical speeds

5.3 CONCLUSION

For coarse particle fillings it is important to modify Morrell's toe and shoulder models to account for their variations with particle fillings. The structure of Morrell's C model allows for the incorporation of radial segregation and centrifuging of silica particles. The effects of radial segregation on the power were studied through the comparison of a mixed

charge power model and the segregated charge power model. No difference between the estimated powers from the two models was seen at low mill speeds (i.e. < 88% of the critical speed) but increasing the mill's speed a difference was noticed. No attempt was made in incorporating the effects of cataracting into Morrell's C model thus for load behaviours where excessive cataracting occurred the model's ability of modelling adequately the mill's power was substantially degraded. Centrifuging of the load at high mill speeds and particle fillings was incorporated into Morrell's C model thus improving mill power estimation.

For fine particle fillings Morrell's mixed charge model was capable of modelling adequately the mill's power draw up to particle fillings of 100%. No modifications were made to the models of the toe and shoulder of the load as proposed by Morrell. Beyond particle filling of 100%, two models were compared to explain the loss in mill power at high particle fillings this are the load expansion and the particle pool formation models. Neither of the two models used independently could explain the power loss so a compromise between load expansion and pool formation models made it possible to model the power drawn by the mill at particle fillings beyond 100%.

CHAPTER 6

MODELLING STUDY 2

Modelling of particle filling and size effects on the load behaviour and power in a dry pilot mill: Torque Arm Model

Moys power model was used to model the power draw data from the experimental study on the effects of particles on the power. This model was chosen due to the fact that it was developed based on the semi phenomenological understanding of the mill's load behaviour and could relate the non linear dependency that a mill's power has on ball filling, mill speed and particle filling. In the model it was assumed that the charge was well mixed and that at particle fillings greater than 100% the load expansion model was valid. The parameter N* was used to model the effects particle filling has on the mill's power draw. Through the understanding of the load behaviour signals while modelling the power better estimation of the mill's power draw resulted.

6.0 INTRODUCTION

The torque-arm model has been widely used to develop power models that are empirical, simplistic and in many instances inadequate in properly relating the dependency of the mill filling on mill speed to the power especially at high mill fillings and mill speeds. Despite this Bond's power model has been used to size many mills and has worked relatively well (Bond, 1961). In instances where a knowledgeable individual would like to determine a mill's power; the Bond power model becomes an attractive option due to its simplicity. A more complex model does exist which is based on Discrete Element Methods and it can penetrate the non linear dependency that mill variables have on the mill power (Mishra & Rajamani, 1992; Cleary, 1998 and Potapov et al, 2007).

The aim of this chapter is to investigate the ability Moys power model has in modelling the effect of increasing coarse or fine particle fillings have on a mill's power draw.

6.1 MOYS POWER MODEL FRAMEWORK

Moys (1993) developed a power model based Bond's power model. With a departure from Bond's empirical outlook, Moys took on developing a power model that was based on the semi-phenomenological understanding of the load behaviour within a mill. Here the model structure reflected the complex non linear dependence of mill power on mill filling

and mill speed. Furthermore the effects of slurry viscosity and liner design could be related to model parameters.

In this model two extremes of load behaviour are coupled together so as to describe the mill power over a wide range of operating conditions. These extremes of load behaviour are:

- Cascading load: Dominant at low mill speeds and can be adequately described by the torque-arm model.
- Centrifuging load: Dominant at high speeds and responsible for the loss in power in mills.

It should be noted that by coupling these two extremes of load behaviour the model does not describe the energy recovered when cataracting media strike the descending mill shell and impart some of their energy. Thus in Moys model the non-centrifuged active portion of the load will draw power according to Bonds power model applied to a mill with a reduced effective diameter and the centrifuged portion of the load draws no power.

Moys power model for the active portion of the load is:

$$P = KD_{eff}^{2.3} \sin\alpha \, \rho_L J_{eff}\left(1 - \beta J_{eff}\right) N_{eff} L \qquad \textbf{6.1}$$

A model that relates the thickness of the centrifuged layer to the mill's operating variables is:

$$\delta_c = J^{\Delta_J} e^{\left[-\frac{N^*-N}{\Delta_N}\right]} \quad \textbf{6.2}$$

Where $\mathbf{N^*}$ and $\Delta_\mathbf{N}$ are parameters that are used to quantify the effect of mill speed on the load behaviour. **N*** is virtually independent of liner design. $\Delta_\mathbf{J}$ is a parameter that governs the strength of the dependency of $\boldsymbol{\delta_c}$ on the load filling **J** and will be a strong function of liner profile design.

The effective diameter of the mill ($\mathbf{D_{eff}}$) is given by:

$$D_{eff} = (1 - 2\delta_c)D \quad \textbf{6.3}$$

Here it is assumed that the thickness of the centrifuged layer is $\boldsymbol{\delta_c D}$.

The effective mill filling ($\mathbf{J_{eff}}$) is given by:

$$J_{eff} = \begin{cases} \frac{J-4\delta_c(1-\delta_c)}{(1-2\delta_c)^2}, & \delta_c < 0.5[1-(1-J)^{0.5}] \\ 0, & \delta_c \geq 0.5[1-(1-J)^{0.5}] \end{cases} \quad \textbf{6.4}$$

A simplification of equation 6.4 was proposed by Moys. The simplification is:

$$J_{eff} = \begin{cases} J - 2\delta_c, & \delta_c < J/2 \\ 0, & \delta_c \geq J/2 \end{cases} \quad \textbf{6.5}$$

6.2 ANALYSIS AND DISCUSSIONS

In chapter 4 it was seen that an increase in the particle filling can lead to an increase in cataracting and centrifuging of the load even at normal mill operating conditions. Such examples can be seen in the load behaviour signals for coarse particles at the mill speed of 78% of the critical speed with particle fillings between 110 - 150% (Figure 4.5a) and likewise for the mill speed of 88% of the critical speed with particle fillings between 80 - 150% (Figure 4.5b). In this study an attempt to model the effect of particle filling on the mill power will be made using Moys power model through a proposal of a relationship between the model parameter N* and particle filling.

To establish the initial parameter set to be used in the regression analysis for the particle filling effects on power; data from the ball only load experiments at the mill speeds of 63, 78, 88 and 98% of the critical mill speed were used. This was important so as to reduce the number of parameters to be established while modelling the particle filling effects on power thus leading to the parameters K, β, Δ_J, α and Δ_N in Moys power model being held constant while searching for parameter N*. For the balls only load the value of N* was kept at 136 similar to what Moys (1993) suggested in his analysis. The angle of repose was kept at 45^o.The model parameters seen in Table 6.1 were established from the regression analysis conducted on a load comprised of balls only. Further information

of the regression analysis can be obtained in Appendix A4.1 and being more specific Table A4.1 and Figure A4.1.

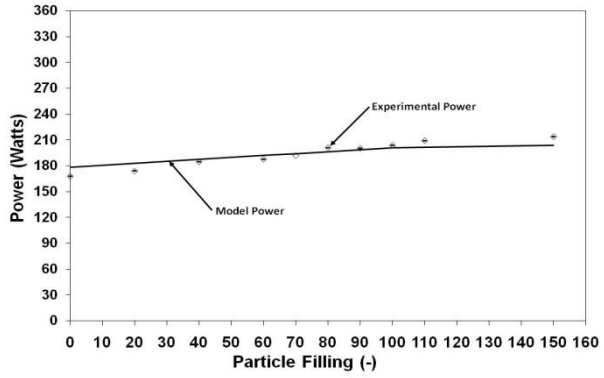
Table 6.1: Established initial parameters for a ball only load

Parameter	Value
K	0.124
β	0.836
Δ_J	2.935
Δ_N	1.018

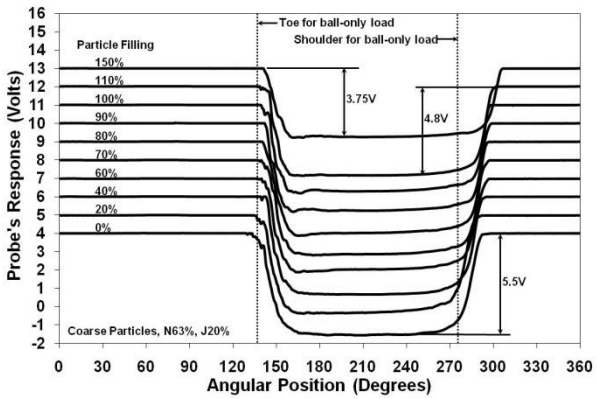
6.2.1 MODELLING OF COARSE PARTICLE EFFECTS ON POWER

For coarse particles at the mill speed of 63% of the critical as seen in Figure 6.1a and tabulated in Table A4.2 of Appendix A3.1, Moys model was capable of modelling adequately the experimental power well across almost all values of particle fillings. The established value of parameter N* across all particle fillings remained at 136 suggesting that at this mill speed increasing particle filling even up to 150% has no effect on power draw. For this mill speed at particle fillings less than 100%; it was anticipated that particles will not have any substantial influence on the power as no cataracting of balls onto the down coming shell occurred and likewise no centrifuging was detected by the inductive probe as seen in Figure 6.1b. Thus the only effect particles would have is increasing the mass of the load. At particle fillings greater than 100% two possibilities occurs i.e. expansion of the load or pooling of particles. In this modelling study the load expansion theory was used in conjunction with Moys power model

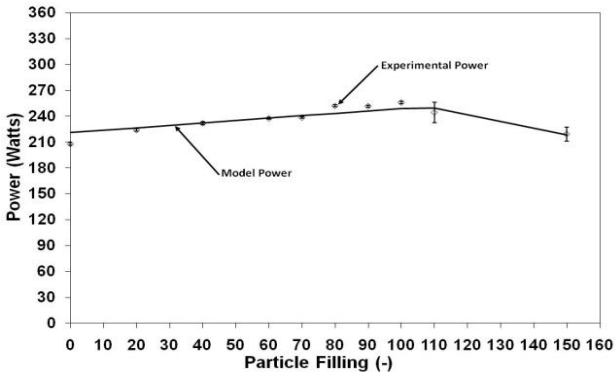
thus leading to a slight decrease in the model's power and likewise a slight under estimation of the experimental power draw for particle fillings greater than 100%. In addition in Moys power model it is assumed that the charge is well mixed which was not the case for particle filling greater than 100% as segregation occurred as seen in Figure 6.1b. No attempt was made to model the segregation.



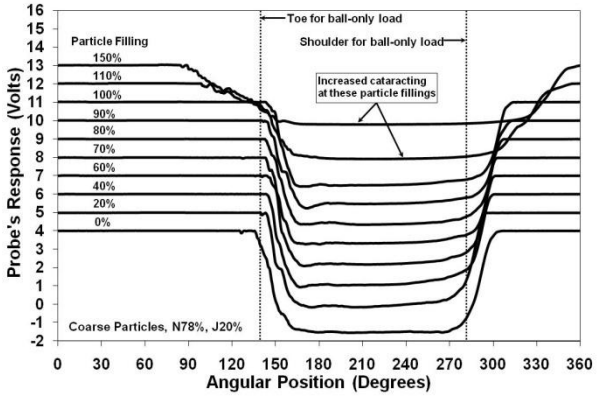
a) Moys power model – Coarse Particles (Mill speed = 63%)



b) Inductive probe signal - Coarse Particles (Mill speed = 63%)



c) Moys power model – Coarse Particles (Mill speed = 78%)



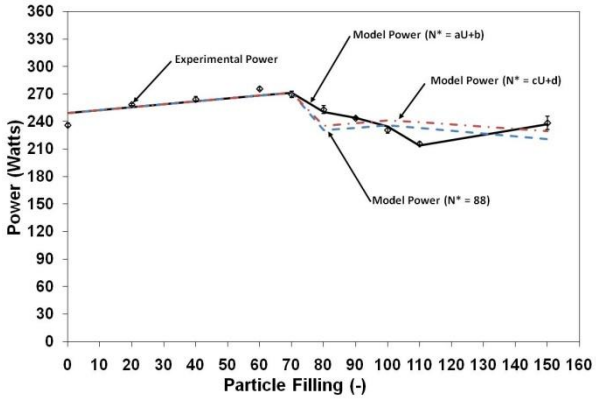
d) Inductive probe signal - coarse particles (Mill speed = 78%)

Figure 6.1: Moys power model predictions and the inductive probe average signal for the mill speeds of 63% and 78% of the critical

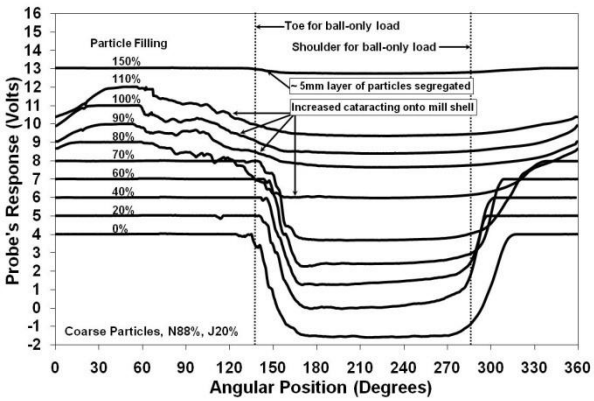
At the mill speed of 78% of the critical as seen in Figure 6.1c; the power model was capable of modelling adequately the experimental power over the full range of particle fillings. For the particle filling where substantial cataracting occurred in conjunction with a significant loss in power drawn by the mill the value on N* in the model decreased to 78.32 as seen in Table A4.3 in Appendix A4.1. It should be noted here that this substantial decrease in power was a result of balls cataracting on the descending mill shell and occurred only at the particle filling of 150%. Thus despite substantial cataracting occurring at a filling of 110% as seen in Figure 6.1d; Moys model does not activate the model that determines the centrifuged layer thickness as no substantial power loss is observed in the experimental data.

At the mill speeds of 88 and 98% of the critical, two different methods were used to describe the relationship between parameter N* and the particle filling. Initially parameter N* was made independent of particle filling in an attempt to use as few parameters as possible. In this case the power model estimations indicated by N* = 88 seen in Figure 6.2a and N* = 98 seen in Figure 6.2c show a significant deterioration in the model's ability to model the power draw beyond the particle filling of 70%. At particle fillings greater than 70% for the mill speed of 88% and likewise beyond the particle filling of 60% for the mill speed of 98% of the critical the load behaviour is dominated by significant cataracting of the load followed by centrifuging of the load at high particle fillings. Due to the influence

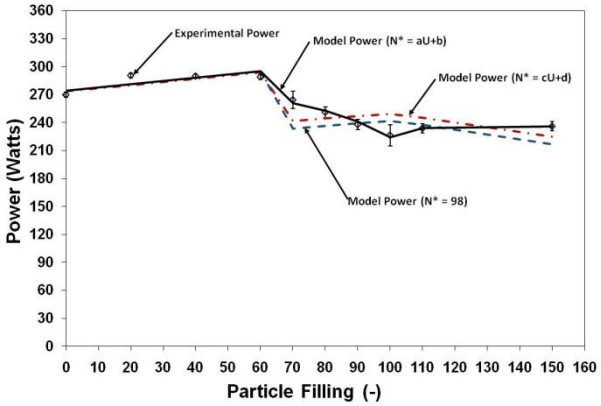
particles have on the load behaviour at particle fillings greater than 70% at the mill speeds of 88 and 98% of the critical it was deemed reasonable to use a linear model to relate the parameter N* to the particle filling. For Moys power model predictions with a linear model defined by N* = cU + d seen in Figure 6.2a and Figure 6.2c also displayed a significant deterioration in the model's ability to describe the power draw at particle filling greater than 70%.



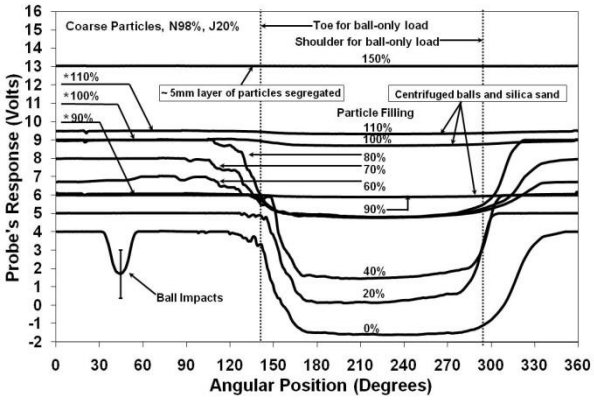
a) Moys power model – Coarse Particles (Mill speed = 88%)



b) Inductive probe signal - Coarse Particles (Mill speed = 88%)



c) Moys power model – Coarse Particles (Mill speed = 98%)



d) Inductive probe signal - Coarse particles (Mill speed = 98%)

Figure 6.2: Moys power model predictions and the inductive probe average signal for the mill speeds of 88% and 98% of the critical

By using a single constant value to define parameter N* (i.e. N* = 88 and N* = 98 as in Figure 6.2) or a linear model (i.e. N*= cU + d as in Figure 6.2) over conditions where both cataracting and centrifuging occur as a result of increasing particle filling reduced the model's ability to describe the power drawn by the mill. In the case of cataracting conditions it can be clearly seen from the experimental data in Figure 6.2 that increasing particle filling led to an increase in cataracting of the load coupled with a reduction in the mill's power draw. While in the case of centrifuging increasing particle filling while maintaining a constant mill speed led to an increase in the mills power draw. For the mill speed of 88% of the critical the load centrifuged at a particle filling of 150%, as seen in Figure 6.2a, and was associated with an 11% increase in the experimental power draw. Likewise for the mill speed of 98% of the critical speed, the centrifuging of the load that occurred after the particle filling of 100% as seen in Figure 6.2c was associated with a 5% increase in power draw. Possibly under the circumstances where increasing particle filling causes a change in the load behaviour the model that defines parameter N* should be limited to cover only a specific load condition.

Through the understanding of the load behaviour and the influence particle filling has on it for the mill speed of 88 and 98% of the critical it was best to use separate linear models to define the relationship between parameter N* and the particle filling when the load is cataracting and when it is centrifuging. For the linear power model predictions indicated by N*=aU+b

as seen in Figure 6.2a and Figure 6.2c, it can be seen that by using two separate linear models to relate parameter N* to the particle filling considerably improves the models ability to describe the power draw. The regression analysis data for the mill speeds of 88% of the critical can be seen in Table A3.4 through to Table A3.6 in Appendix A3.2. Likewise for the mill speed of 98% of the critical the regression analysis data can be seen in Table A3.7 through to Table A3.9 in Appendix A3.2.

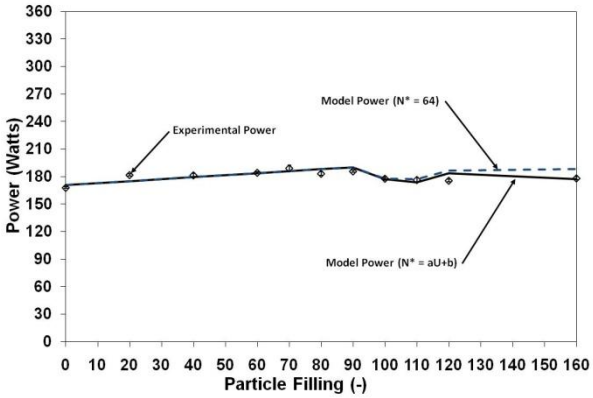
6.2.2 MODELLING OF THE FINE PARTICLE EFFECTS ON POWER

For the fine particles at the mill speeds of 63%, 78% and 88% of the critical speed no cataracting or centrifuging was experienced across any particle fillings. This is seen in the inductive probe signals in Figure 6.3b, 6.3d and 6.3f. The fine particles possibly lubricate the load more efficiently than coarse particles thus limiting the extent in which the load could possibly cataract. This kind of load behaviour across these mill speeds also led to a power draw that is relatively constant across all particle fillings.

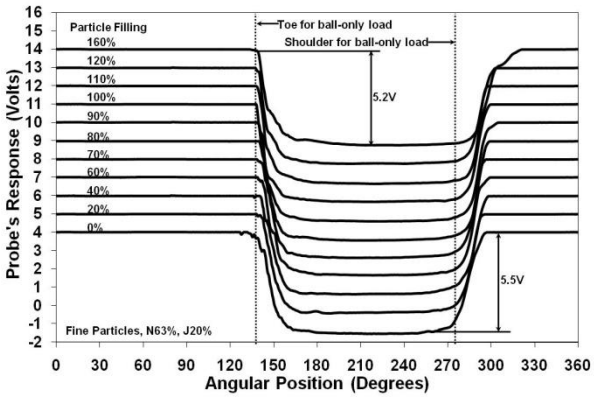
From the load behaviour investigation for the mill speeds between 63-88% of the critical, it is possible to safely assume that increasing fine particle filling has very little or no influence on the load behaviour and thus the parameter N* could be independent of the particle filling. For particle fillings greater than 100% the parameter N* in Moys power model was set at the value of 64 for the mill speed of 63% of the critical (Figure 6.3a), a

value of 78.98 for the mill speed of 78% of the critical (Figure 6.3c) and a value of 89.2 for the mill speed of 88% of the critical (Figure 6.3e). Using these values of the N* parameter for mill speeds between 63-88% of the critical, Moys power model was capable of modelling adequately the experimental power draw over most particle fillings. For the particle filling of 150%, Moys power model over estimated the experimental power draw by about 6%. It is possible that when excessive amounts of fine particles are present in the mill (i.e. U > 100%) a powder pool possibly exists that would cause a decrease in the power draw. In this modelling exercise the load expansion theory was used in conjunction with Moys power model. No investigations were conducted to look at the effects of a particle pool on the power draw as this was dealt in quite some detail in section 5.2.3 in Chapter 5. This once again strongly supports the possibility of a powder pool being formed.

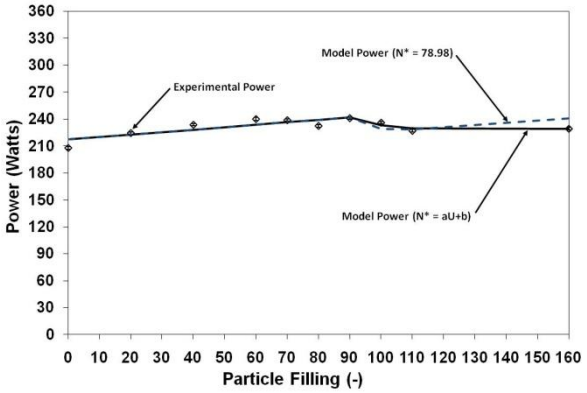
Using a linear model to define the dependency of parameter N* on the particle filling ($N^* = aU + b$) further improved the ability of Moys power model in modelling adequately the experimental power draw for particle fillings greater than 100% at the mill speed of 63% (Figure 6.3a), 78% (Figure 6.3c) and 88% of the critical speed (Figure 6.3a). Although in the case where the linear model is used the power loss is strongly related to the centrifuged layer in Moys power model being thicker thus accounting for the power loss.



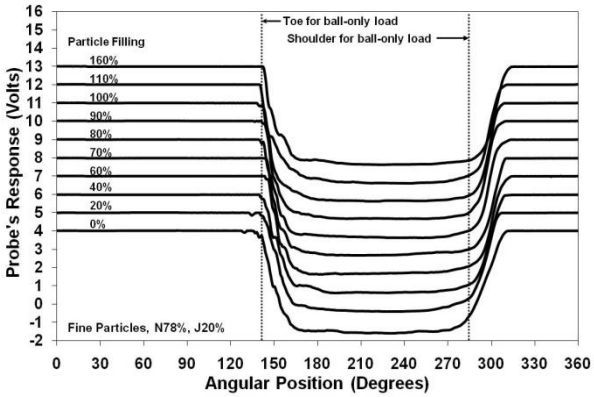
a) Moys power model – Fine Particles (Mill speed = 63%)



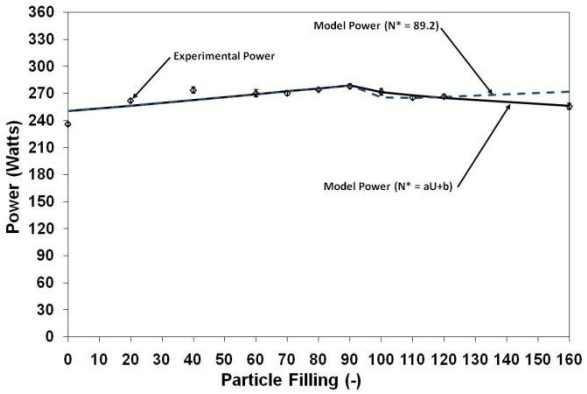
b) Inductive probe signal - Fine Particles (Mill speed = 63%)



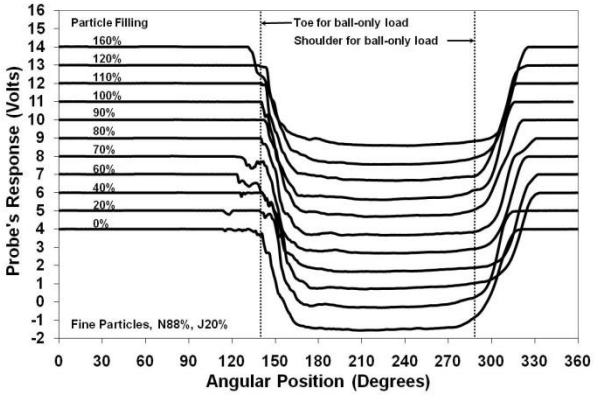
c) Moys power model – Fine Particles (Mill speed = 78%)



d) Inductive probe signal - Fine Particles (Mill speed = 78%)



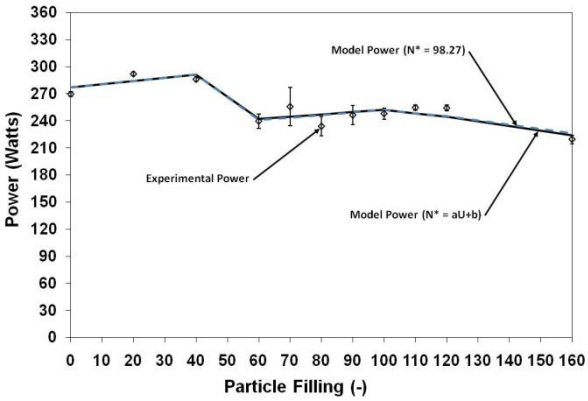
e) Moys power model – Fine Particles (Mill speed = 88%)



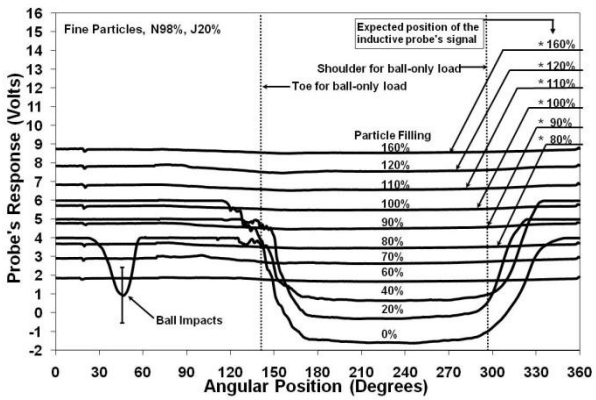
f) Inductive probe signal - Fine Particles (Mill speed = 88%)

Figure 6.3: Moys power model predictions and the inductive probe average signal for the mill speeds of 63%, 78% and 88% of the critical

Interestingly; for the case of 98% of the critical speed as seen in Figure 6.4b the load behaviour was either in and active charge state or centrifuged depending on the particle filling. This becomes interesting as these are the two extremes in load behaviour that Moys power model is based on i.e. either the load is comprised of an active cascading charge or the combinations of an active charge and centrifuged charge. However it should be made clear that in the centrifuged state (U > 60%) the behaviour of the active load is not known and the load could either be cascading or experiencing a significant amount of cataracting.



a) Moys power model – Fine Particles (Mill speed = 98%)



b) Inductive probe signal - Fine Particles (Mill speed = 98%)

Figure 6.4: Moys power model predictions and the inductive probe average signal for the mill speeds of 98% of the critical speeds

From Figure 6.4a it can be seen that Moys power model was capable of modelling adequately the power over all particle fillings. For the mill speed of 98% of the critical and for particle fillings greater than 40% the two

methods that define the relationship between parameter N* and particle filling were used in Moys power model. The use of the two models i.e. N* = 98.27 and N* = aU+b in Moys power model yield identical predictions of the experimental power over all particle fillings greater than 40%. The identical predictions are most likely due to the load conditions being similar to the basis of Moys power model. Furthermore it should be noted that after centrifuging occurred the power did increase and peak as the particle filling increased. This is due to the fact that when a mill with a smaller effective diameter is formed as a result of part of the active charge being centrifuged it would behave as a new mill and its power should increase with increasing particle filling provided that the mill speed is held constant.

The regression analysis data for the mill speeds of 63%, 78%, 88% and 98% of the critical can be seen in Table A3.10 through to Table A34.17 in Appendix A3.3.

6.3 CONCLUSION

In this modelling study a torque arm model in the form of Moys power model was used to model the mill's power draw from the experimental study conducted in Chapter 4. The experimental study offered a unique data set whereby the mill's power draw was obtained in conjunction with load behaviour data from an inductive proximity probe at the mill speeds of 63%, 78%, 88% and 98% of the critical speed. Various conditions of load

behaviour were encountered with increasing coarse and fine particle filling such as segregation, cascading, cataracting, centrifuging and possibly the pooling of particles. In the modelling it was assumed the charge was well mixed and no attempts were made in modelling the impact cataracting of the load has on the power. From the Moys power model the parameter N* was chosen to model the effects of increasing particle filling has on the mill's power draw. Two model definitions were used in the study whereby one kept the value of parameter N* to be constant and independent of particle filling and the other made parameter N* vary linearly with particle filling.

In the case of coarse particle filling at low mill speeds (i.e. 63% of the critical) the power draw can be predicted using N* = 136 as previously suggested by Moys (1993). It seems at such low speeds increasing the coarse particle filling does not have any significant influence on the load behaviour and likewise power draw. Increasing the mill speed to 78%, 88% and 98% of the critical a new value of parameter N* had to be established particularly when the conditions of cataracting or centrifuging prevail. For these mill speeds a better estimations of the mill's power draw resulted when the power draw at the conditions of cataracting and centrifuged are modelled based on separate N* linear models as particle filling is increased. This resulted from the fact that when balls cataract and strike on the descending mill shell it is normally accompanied by a loss in power draw for that mill speed. Increasing coarse particle filling increases

the intensity of cataracting at that mill speed. When centrifuging occurs at a constant speed while increasing the coarse particle filling it is accompanied by an increase in the power drawn by the mill.

For the case of increasing fine particle filling at the mill speeds of 63, 78 and 88% of the critical a linear model would be the best to use in defining the relationship between N* and the particle filling. At these mill speeds there is a possibility that the loss in power occurs as a result of the presence of a particle pool as no cataracting or centrifuging occurred. Increasing the mill speed to 98% of the critical the relationship between parameter N* and the particle filling could either be a constant value or a linear model. By understanding the load behaviour improvements in the modelling of a mill's power draw can be brought about.

CHAPTER 7

CONCLUSION AND RECOMMENDATIONS

7

7.0 CONCLUSION

Many factors that influence the ball load behaviour have been previously studied. It is known that a load comprised of balls only behaves quite differently when ore is introduced into the mill. Different ore types and sizes influence the ball load to varying extents. Typically in industry, while refilling a ground out mill the operator would fill the running mill with ore up to the point where the maximum power drawn by the mill is achieved. This practice is from the fact that the mill power has a parabolic dependency on the mill filling. Under filling the mill would result in an inefficient operation of the mill due to ball and liner wear. Overfilling the mill would also result in an inefficient mill operation due to a slowdown in grinding rates as a result of the presence of excess particles in the mill. At the maximum power draw it is generally assumed the load is well mixed and that the void spaces between the balls are full with particles. To the operator this translates to an efficient mill and maintains the maximum power draw as a set point. This study sets to understand how particle filling and size influence the ball load behaviour and power in a dry mill. The study mimics the filling of an industrial ball mill from when it is empty to when it is 50% overfilled with particles.

A novel technique in load behaviour measurements was used to conduct this study. The technique made use of an inductive proximity probe to measure the steel ball load position independently of the presence of

particles in the mill. Static and dynamic response test were performed on the inductive probe to assess its suitability for load behaviour measurements. The static test show that the inductive probe's signal varies linearly with an increase in distance from its sensing face of a metallic target. The dynamic tests show that the probe takes 6.9ms to reach 98% of its maximum signal value thus translating to an error of 2.54^{o} at the highest mill speed of 60.78rpm for the pilot mill used in this study. In the case of industrial mills that typically run at lower mill speeds this error would be insignificant. The probe was also tested in a mill as a means of measuring the dynamic load behaviour. Load conditions such as cataracting, centrifuging, ball packing, toe and shoulder positions as a function of mill filling and speed were easily detected and distinguishable in the probe's signal. The probe exhibits superior shoulder angular position measurement capabilities when compared to a force probe but the toe's angular position can be influenced with balls cataracting in this region. Furthermore, the probe does not require complicated circuitry or signal analysis algorithms. The inductive probe can be used in industrial mills provided the necessary protection is made for the probe to operate in the harsh conditions prevalent in the mill. For an industrial mill, it would be preferred to use the probe for investigative studies rather than a measurement device to obtain an additional control variable for the load behaviour. Here the load behaviour could be easily measured as mill operating variables are changed and a clear picture drawn as to how the load responds. The information from such investigations could be used in

conjunction with the Discrete Element Model (DEM) simulators to further understand the load behaviour in the mill. Possibly this would lead to enhancing the design of the mill internals or select suitable operating conditions that would lead to an optimal load behaviour prevailing. Caution should be taken in selecting a sensor with a suitable measuring range due to the fact that for the larger steel balls the signal will be noisier than the probe response signals displayed in this thesis. Possibly, for mills containing large ball sizes a different signal analysis technique could be used based on a moving standard deviation of the signal response rather than analysing the average signal response.

Increasing the particle filling of coarse silica sand particles at different mill speeds between 63-98% of the critical mill speed led to excessive cataracting of the load, radial segregation and centrifuging. These changes in load behaviour as particle filling was increased at a set mill speed led to variations in the experimental mill power draw trends. The radial segregation of silica sand particles to the periphery of the load was quantified and reveals that its intensity increases with an increase in mill speed and particle filling. The depletion of the coarse particles from the core of the load due to radial segregation causes an increased chance of ball to ball contacts thus possibly leading to an increased ball wear rate. The segregated silica sand causes excessive cataracting of the load onto the exposed mill shell thus leading to a loss in the mill's power. The centrifuging of the segregated silica sand leads to further losses in mill

power. The maximum mill power drawn by the mill exhibits the tendency to move to lower particle fillings as mill speed is increased. The steel balls being located at the core of the load reduced their chances to damage or break the silica particles thus possibly leading to the slowdown of grinding rates within the mill. Mill power loss due to cataracting and centrifuging further reduces the energy available for breakage of particles thus again negatively impacting the grinding rates. Should radial segregation occur in an industrial mill then the action of the operator chasing the maximum power by increasing the mill's particle filling would lead to the mill operating inefficiently especially at high mill speeds (i.e. greater than 88% of the critical speed). The development of the inductive probe to be used as an additional online measurement for the early detection of segregation would help the mill operator substantially.

The load comprised of fine silica particles behaved as one would expect for mill speeds up to 88% of the critical. The load was only sensitive to increases in mill speed thus leading to a rise in the shoulders angular position. No sensitivity was established with particle filling increase at a particular mill speed. The peak in mill power occurred at particle fillings between 80 – 110% followed by a slight loss in mill power. At this stage it was assumed that this loss in power is probably due to either load expansion or a particle pool being formed at the toe of the load. None of the two assumptions were validated experimentally. Unfortunately the inductive probe can only sense the presence of metallic objects; thus it

would be important in such cases that a second probe would be needed that can sense both metallic and non-metallic objects. Possibly a force probe or a capacitive proximity sensor could be used to detect the powder pool located at the toe of the load. Interestingly, the capacitive sensor can be very effective in measuring the presence of non- metallic objects, the density, thickness and location. The capacitive probe works by sensing changes in the dielectric of the material and therefore changes in capacitance due to the presence of a non-conductor in the sensing range. The sensitivity of the sensor to the non-conductive target is directly proportional to the dielectric constant of the material. When the mill speed was increased to 98% of the critical the fine silica particle caused the balls to centrifuge at a particle filling greater than 40% with a corresponding peak in the mill's power draw between particle fillings of 20 – 40%.

It should be noted that for both the coarse and fine particle experiments the effect of the continuous removal of fine particles generated in the mill by an air draft was not studied. Such an experiment would give an exact replication of an industrial air swept mill. This continuous removal of the right size particles can possibly change the load behaviour in the mill and likewise its power draw. Furthermore, no work was conducted into the effects that the various load behaviour conditions encountered have on the grinding rates in the mill. This work would form a basis to establish the effects that the various load behaviour conditions encountered in the experiments have on the energy efficiency of grinding. From the

experimental study it can be seen that using the power alone to be the sole indicator for finding a mill's best operating point is not always the best thing to do. Various conditions can arise within the mill that would lead to a peak in power at low particle fillings thus increasing ball and liner wear rates and leading to inefficient mill operations. With the greater use of variable speed mills in the mining industry it becomes even more important to understand how a mill would behave when various particle sizes are being filled into the mill in relation to the mill speed. It would be highly discouraged to operate a mill at speeds higher than 88% of the critical as in both cases of coarse and fine particle fillings the load behaviour changed dramatically and the conditions would lead to the mill being operated inefficiently.

A modelling study was conducted using Morrell's C model. The model was chosen due to the fact that it contains physical descriptors of the load such as the toe, shoulder and charge inner surface. Modifications to Morrell's model were made in the toe and shoulder models. A segregated charge model was proposed for situations where radial segregation occurred. A subtle difference was noted when the radial segregation power model results were compared to that of the mixed charge model. A centrifuged charge model was proposed which generally improved the model's capability of modelling the power draw during the centrifuging condition. In the case of fine particles at high particle fillings (U>100%) a split between a particle pool and load expansion model was proposed which improved

Morrell's C model ability of modelling the fine particle power draw. The modified Morrell C model was suitable in modelling the experimental power draw apart from conditions where there was intense cataracting of the load. No attempt was made to include the effects of the cataracting portion of the load into Morrell's model.

In a second modelling exercise the torque arm model in the form of the Moys power model was used to model the experimental power draw. This model was chosen due to the fact that it was developed based on the semi phenomenological understanding of the mill's load behaviour and could relate the non linear dependency that a mill's power has on ball filling, mill speed and particle filling. The parameter N* was assumed to either vary linearly with particle filling or be independent of particle filling. Improved modellling come about when N* is related linearly to the particle filling. With these modifications added to the N* model the modified Moys model was capable of modelling the mill's power draw sufficiently.

This modelling exercise demonstrated the importance of understanding the impact that mill operating variables and mill design have on the load behaviour and power draw and through this establish improvements that can be made to existing power models so as to enhance the models ability in modelling adequately a mill's power draw. Both the Morrell's C power model and Moys power model with the necessary modifications were

capable of modelling adequately the power drawn by the mill for most of the conditions occurring in the mill.

The Discrete Element Model (DEM) treats the charge as discrete particles which make it quite a powerful tool in simulating the complex load behaviours experienced in this study and likewise its corresponding power draw. Currently most of the available DEM packages can model particles with different densities and likewise shapes which will be quite useful in modelling the experiments conducted. Furthermore should a researcher wish to simplify the problem by using spherical particles for both the balls and silica particles with no breakage of particles occurring then the differences in the load behaviours can be established and necessary adjusting of the DEM model parameters can be done wisely and in an informed manner.

Some DEM simulators couple their models with Discrete Grain Breakage (DGB) models, Computational Fluid Dynamic (CFD) models, Smooth Particle Hydrodynamic (SPH) models and Multi-Phase Flow models (Cleary, 2001; Potapov et al, 2007). In most cases there has been a lack of DEM validation data to test their simulators against the reality over a wide range of conditions from a controlled experiment. The coarse and fine particle results can be used to validate DEM simulations and in particular when the researcher's interests involve a charge mixed with particles of different densities and of various particle sizes and shapes

undergoing breakage. When breakage of particles are involved in a DEM simulator the problem becomes handling the great number of particles resulting from the breakage events (i.e. tracking and storing information related to the new particles) as this would require tremendous computing power and memory and it would take a long period of time to obtain sensible results.

For the coarse particle case, the use of the technique published by Potapov et al (2007) of coupling the DEM with the PBM model to form what they refer to as the Fast-Breakage model would simplify the DEM simulation and bring down considerably the simulation time. For the fine particle case, a tremendous amount of particles will be involved from the start of the simulation and will continue to increase as breakage occurs in the mill. Possibly treating the fine particles as slurry would further simplify the problem. Fine particles have the ability of easily pouring through the void spaces in the charge without significantly affecting the behaviour of the ball load. It is important to establish the bottom size limit of the size distribution where below this size the particles would be regarded as slurry.

REFERENCES

Agrawala, S., Rajamani, R. K., Songfack, P. and Mishra, B. K., 1997. Mechanics of media motion in tumbling mills with 3D Discrete Element Method. Minerals Engineering, Volume 10(2), pp. 215 - 227.

Austin, L. G., Klimpel, R. R. and Luckie, P. T., 1984. Process engineering of size reduction: Ball Milling. Society of mining engineers of the American Institute of Mining, Metallurgical and Petroleum Engineers, Inc.

Behera, B., Mishra, B. K. and Murty, C.V.R., 2007. Experimental analysis of charge dynamics in tumbling mills by vibration signature technique. Minerals Engineering, Volume 20(1), pp. 84 – 91.

Bond, F.C, 1961a. Crushing and grinding calculations Part 1. British Chemical Engineering, Volume 6(8), pp. 378 – 385.

Bond, F.C, 1961b. Crushing and grinding calculations Part 2. British Chemical Engineering, Volume 6(8), pp. 543 –548.

Cundall, P.A. and Strack, O. D. L, 1979. Discrete numerical model for granular assemblies. Geotechnique, Volume 29(1), pp. 47 –64.

Campbell, J., Spencer, S., Sutherland, D., Rowlands, T., Weller, K., Cleary, P. and Hinde, A., 2001. SAG mill monitoring using surface vibrations. Proceedings of the International Autogenous and Semi-Autogenous grinding technology conference 2, pp. 373-385.

Campbell, J. J., Holmes, R. J., Spencer, S. J., Sharp, V., Davey, K. J., Barker, D. G. and Phillips, P. L., 2003. The collection and analysis of single sensor surface vibration data to estimate operating

conditions in pilot scale and production scale AG/SAG mills. Proceedings: XXII International Mineral Processing Congress, pp. 280 – 288.

Cleary, P. W., 1998. Predicting charge motion, power draw, segregation and wear in ball mills using discrete element methods. Minerals Engineering 11(11), pp. 1061-1080.

Cleary, P. W., 2001. Recent advances in DEM modelling of tumbling mills. Minerals Engineering 14(10), pp. 1295-1319.

Davis, E. W., 1919. Fine crushing in ball mills. Transactions of the American Institute of Mechanical Engineers (AIME). Volume 61, pp. 250.

Dong, H. and Moys, M. H., 2003. Load behaviour and Mill power. International Journal of Minerals Processing, Volume 69. pp 11-28.

Dong, H., Couvas, C., Breetzke, M. and Moys, M., 2005. Measurement of load behaviour of an Eskom coal mill. SAIMM-Mineral Processing Conference, Cape Town, OR20, pp. 38.

Dupont, J. F. & Vien, A., 2001a. Continuous SAG volumetric charge measurements. Proceedings of the 33rd Annual Canadian Mineral Processing AGM, CIM, Ottawa, Canada. pp. 51 – 67.

Dupont, J. F. & Vien, A., 2001b. Direct measurement and control of SAG volumetric loads using embedded sensors. Preprints of the SME annual meeting, USA. pp. 1 – 5.

Fuerstenau, D. W., Kapur, P. C. and Velamakanni, 1990. A multi-torque model for the effects of dispersants and slurry viscosity on ball

milling. International Journal of Minerals Processing, Volume 28, pp 81-98.

Gugel, K., Palacios, G., Ramirez, J. and Parra, M., 2003. Improving ball mill control with modern tools based on digital signal processing (DSP) technology. Cement industry technical conference. pp. 311 – 318.

Govender, I., Powell, M. S. and Nurick, G. N., 2002. Automated imaging technique to track the 3D motion of particles. Experimental Mechanics. Volume 42 (2), pp 153 - 160.

Govender, I., McBride, A. T., and Powell, M. S., 2004. Improved experimental tracking techniques for validating discrete element methods simulations of tumbling mills. Experimental Mechanics. Volume 44 (6), pp 593 - 607.

Harding, H., 1939. The ‘electric ear’, a device for automatically controlling mills by their sound. Transactions of the American Institute of Mining, Metallurgical and Petroleum Engineers. Volume 134, pp 371 - 380.

Jain, N., Ottino, J. and Lueptow, R., 2005. Regimes of segregation and mixing in combined size and density granular systems: an experimental study. Granular Matter 7, pp. 69 – 81

Jaspan, R. K., Young, G. J. C and Mellor, M. S., 1986. ROM mill power draft control using multiple microphones to determine mill load. Gold 100: Proceedings of the international conference on gold. SAIMM, Volume 2, pp 483-492.

Kalala, J. T., Breetzke, M. and Moys, M., 2007. Study of the influence of liner wear on the load behaviour of an industrial tumbling mill using Discrete Element Methods (DEM). International Journal of Mineral Processing. Volume 86(1-4), pp 33-39.

Kiangi, K. and Moys, M. H., 2006. Measurement of load behaviour in a dry pilot mill using an inductive proximity probe. Minerals engineering Volume 19(13), pp. 1348-1356.

Kolacz, J., 1997. Measurement system of the mill charge in grinding ball mill circuits. Minerals Engineering, Volume 10, No. 12, pp 1329-1338.

McIvor, R. E., 1983. Effect of speed and liner configuration on ball mill performance. Mining Engineering, Volume 35(6), pp 617 – 624.

Mishra, B. K., and Rajamani, R. J., 1992. The discrete element method for the simulation of ball mills. Applied Mathematical Modelling, Volume 16, 598-604.

Morrell, S., 1993. The prediction of power draw in wet tumbling mills. PhD Thesis. University of Queensland.

Moys, M. H., 1985. The measurements of parameters describing the dynamic behaviour of the load in a grinding mill. Journal of the South African Institute of Mining and Metallurgy, Volume 85(2), pp 51-63.

Moys, M. H., 1993. A model of mill power as affected by mill speed, load volume and liner design. Journal of the South African Institute of Mining and Metallurgy, Volume 93(6), pp 135-141.

Moys, M. H., Van Nierop, M. A. and Smit, I., 1996. Progress in measuring and modelling load behaviour in pilot and industrial mills. Minerals Engineering, Volume 9(12), pp 1201-1214.

Moys, M. H., Smit, I. and Stange, W., 1996. The measurement of forces exerted by the load on liners in rotary mills (wet and dry). International Journal of Minerals Processing, Volume 44-45, pp 383-393.

Nesbit, P. Q. and Moys, M. H., 1998. Load behaviour in the HICOM nutating mill. Minerals Engineering, Volume 11(10), pp 979 - 988.

Pax, R., 2001. Non-Contact acoustic measurement of in-mill variables of SAG mills. Proceedings of the International Autogenous and Semi-Autogenous grinding technology conference 2, pp. 386-393.

Potapov, A., Herbst, J., Song, M. and Pate, W., 2007. A DEM-PBM fast breakage model for simulation of comminution processes. Proceedings of Discrete Element Methods, Australia.

Powell, M. S. 1991. The effect of liner design on the motion of the outer grinding elements in a rotary mill. International Journal of Minerals Processing, Volume 31(3-4), pp 163-193.

Powell, M. S. and Nurick, G. N., 1996a. A study of charge motion in rotary mills Part 2- Experimental work. Minerals Engineering, Volume 9, No. 3, pp 343 – 350

Powell, M. S. and Nurick, G. N, 1996b. A study of charge motion in rotary mills Part 3 – Analysis of results. Minerals Engineering 9(4), pp. 399-418.

Qiu, X., Potapov, A., Song, M. and Nordell, L., 2001. Prediction of wear of mill lifters using DEM. Proceedings of the international Autogenous and Semi-Autogenous Grinding Technology, Vancouver, Canada. Volume IV, pp. 260-265.

Rose, H. E. and Sullivan, R. M. E, 1958. Treatise on the internal mechanics of ball tube and rod mills. Constable and Company Ltd., London.

Smit, I., 2000. The effect of slurry viscosity and mill speed on the behaviour of a rotary grinding mill. MSc Dissertation. University of the Witwatersrand, Johannesburg.

Skorupa, J. and Moys, M. H., 1993. Measurement of the radial and tangential forces exerted by the load on a liner in a ball mill as a function of load volume and mill speed. International Journal of Minerals Processing, Volume 37, pp 239 – 256.

Tangsathitkulchai, C., 2003. Effects of slurry concentration and powder filling on the net mill power of a laboratory ball mill. Powder Technology 137(3), pp. 131-138.

Tano, K; Palsson, B and Sellgren, A, 2005. Online lifter deflection measurements showing flow resistance effects in grinding mills. Minerals Engineering 18(11), pp. 1077-1085.

Van Nierop, M. A., and Moys, M. H., 2001. Exploration of mill power modelled as a function of load behaviour. Minerals Engineering, Volume 14(10), pp 1267-1276.

Vermeulen, L. A., Ohlson, M. J. and Schakowski, F., 1984. Continuous monitoring of information from the inside of a rotary mill. Journal of the South African Institute of Mining and Metallurgy, Volume 85(2), pp 51-63.

Vermeulen, L. A. and Howat, D. D., 1986. Fluctuations in slip of the grinding charge in rotary mills with smooth liners. International journal of mineral processing, Volume 16, pp. 153 – 168.

Watson, J. L, 1985. An analysis of grinding media noise. Powder Technology, Volume 41, pp 83-89.

White, H. A, 1905. Theory of the tube mill. Journal of the Chemical, Metallurgical and Mining Society of South Africa, Volume 5, pp 290-305.

Zeng, Y. and Forssberg, E., 1991. Effect of powder filling fraction on particle size and energy consumption in coarse grinding. Scandinavian Journal of Metallurgy 20, pp. 300 – 304.

Zeng, Y. and Forssberg, E., 1992. Effects of operating parameters on vibration signal under laboratory scale ball grinding conditions. International journal of mineral processing, Volume 35, pp 273 – 290.

Zeng, Y. and Forssberg, E., 1993. Monitoring grinding parameters by signal measurements for an industrial ball mill. International journal of mineral processing, Volume 40, pp 1 – 16.

APPENDIX 1

EXPERIMENTAL RESULTS

A1

A1.1 EXPERIMENTAL DATA FOR THE COARSE PARTICLE EXPERIMENTS

Mill speed of 63% of the critical:

	Speed		Toe		Shoulder		Torque		Power	
Particle Filling	Average	Standard deviation	Average	Standard deviation	Average	Standard deviation	Average	Standard deviation	Average	Standard deviation
%	%	%	Degrees	Degrees	Degrees	Degrees	Nm	Nm	watts	watts
0	62.99	0.09	153.25	1.81	290.93	2.66	43.33	0.20	167.94	0.92
20	62.43	0.40	155.01	2.48	285.25	1.10	45.20	0.28	173.93	1.85
40	63.22	0.37	156.94	3.08	290.43	2.45	47.38	0.19	184.66	1.10
60	62.58	0.31	156.49	2.65	291.19	1.95	48.69	0.27	187.75	1.60
70	63.00	0.45	158.64	5.43	292.66	1.90	49.37	0.15	191.79	1.27
80	64.45	0.43	159.75	6.63	294.56	1.83	50.59	0.19	201.00	1.57
90	63.68	0.45	166.70	8.00	295.22	1.72	51.02	0.30	200.29	1.47
100	64.11	0.27	155.50	4.32	296.27	1.16	51.57	0.30	203.69	1.59
110	64.02	0.42	154.63	1.54	297.72	1.00	52.98	0.22	209.05	1.55
150	64.20	0.26	156.11	5.67	303.84	2.43	54.00	0.44	213.53	2.33

Mill speed of 78% of the critical:

	Speed		Toe		Shoulder		Torque		Power	
Particle Filling	Average	Standard deviation	Average	Standard deviation	Average	Standard deviation	Average	Standard deviation	Average	Standard deviation
%	%	%	Degrees	Degrees	Degrees	Degrees	Nm	Nm	watts	watts
0	75.32	0.12	168.45	23.45	300.41	3.67	44.90	0.31	207.92	1.32
20	76.59	0.11	163.16	4.82	291.52	2.69	47.52	0.23	224.04	1.23
40	77.10	0.13	163.39	6.73	297.31	3.12	48.85	0.37	231.81	1.90
60	77.11	0.15	167.51	7.17	297.64	2.20	50.06	0.18	237.49	1.16
70	76.67	0.11	172.68	6.98	299.08	1.78	50.55	0.18	238.44	0.90
80	78.31	0.12	175.37	4.60	302.64	2.34	52.29	0.21	252.00	1.12
90	78.46	0.09	173.58	5.85	305.59	3.79	52.14	0.23	251.65	1.07
100	78.11	0.10	161.68	2.70	307.68	2.78	53.26	0.27	255.97	1.44
110	79.51	0.13	149.16	10.19	330.83	13.25	49.98	2.47	244.45	11.87
150	80.66	0.16	110.35	5.94	346.36	7.45	44.17	1.63	219.35	8.13

Mill speed of 88% of the critical:

	Speed		Toe		Shoulder		Torque		Power	
Particle Filling	Average	Standard deviation	Average	Standard deviation	Average	Standard deviation	Average	Standard deviation	Average	Standard deviation
%	%	%	Degrees	Degrees	Degrees	Degrees	Nm	Nm	watts	watts
0	85.05	0.48	163.40	3.38	312.38	3.85	45.14	0.28	236.16	1.90
20	86.62	0.17	162.05	1.90	294.55	1.42	48.51	0.19	258.62	1.28
40	86.06	2.81	163.71	3.94	297.66	1.82	49.43	0.64	264.44	3.00
60	87.67	0.15	163.84	2.96	306.24	3.26	51.13	0.30	275.74	1.72
70	88.47	0.14	172.87	4.49	316.10	9.08	49.53	0.69	269.59	3.76
80	90.14	0.10	137.10	9.56	340.44	13.44	45.63	0.82	253.05	4.60
90	88.70	0.17	151.18	22.18	352.26	5.57	44.69	0.30	243.85	1.60
100	88.96	0.22	134.43	8.63	353.17	5.22	42.18	0.62	230.85	3.67
110	88.97	0.11	152.07	10.63	346.21	14.88	42.48	1.54	215.70	2.16
150	89.14	0.51	Particle segregation occurs		Particle segregation occurs		43.43	1.33	238.64	7.24

Mill speed of 98% of the critical:

	Speed		Toe		Shoulder		Torque		Power	
Particle Filling	Average	Standard deviation	Average	Standard deviation	Average	Standard deviation	Average	Standard deviation	Average	Standard deviation
%	%	%	Degrees	Degrees	Degrees	Degrees	Nm	Nm	watts	watts
0	95.89	0.22	180.48	25.50	332.08	11.00	45.73	0.47	269.81	2.56
20	96.62	0.14	172.21	4.29	298.93	2.66	48.87	0.34	290.51	2.18
40	95.96	0.20	176.07	2.95	302.23	1.93	49.09	0.26	289.87	1.65
60	96.97	0.07	131.00	18.91	325.98	8.89	48.42	0.42	288.93	2.54
70	98.32	0.14	143.43	14.41	324.32	8.28	43.70	1.53	264.32	9.29
80	99.91	0.15	149.59	6.38	314.89	4.51	40.84	0.92	251.07	5.65
90	97.28	1.56	Centrifuging occurs		Centrifuging occurs		38.86	0.94	237.85	5.33
100	99.92	0.13	Centrifuging occurs		Centrifuging occurs		36.82	1.85	226.36	11.25
110	99.33	0.18	Centrifuging occurs		Centrifuging occurs		38.28	0.84	233.84	5.00
150	100.17	0.46	Silica particles centrifuged		Silica particles centrifuged		38.22	0.80	235.90	4.97

A1.2 EXPERIMENTAL DATA FOR THE FINE PARTICLE EXPERIMENTS

Mill speed of 63% of the critical:

	Speed		Toe		Shoulder		Torque		Power	
Particle Filling	Average	Standard deviation	Average	Standard deviation	Average	Standard deviation	Average	Standard deviation	Average	Standard deviation
%	%	%	Degrees	Degrees	Degrees	Degrees	Nm	Nm	watts	watts
0	62.98	0.46	169.54	10.76	290.35	3.61	43.33	0.20	167.94	0.92
20	63.91	0.37	164.70	6.60	291.77	2.63	46.21	0.17	181.70	1.07
40	63.63	0.47	154.88	1.78	293.46	2.86	46.34	0.26	181.43	2.20
60	62.23	0.49	155.76	4.03	292.24	4.08	48.11	0.47	184.19	1.20
70	63.63	0.44	153.67	1.80	292.45	2.60	48.28	0.47	189.02	3.08
80	62.64	0.45	151.34	1.99	294.80	1.93	47.52	0.20	183.12	1.89
90	63.41	0.41	150.99	2.17	295.88	4.26	47.60	0.15	185.71	1.09
100	63.57	0.42	150.71	2.82	294.66	1.97	45.46	0.18	177.80	1.53
110	63.37	0.36	167.91	6.99	295.13	1.99	45.25	0.32	176.41	2.21
120	63.19	0.44	165.77	7.94	296.76	2.90	45.17	0.10	175.61	1.43
160	64.12	0.48	173.05	16.22	303.71	6.32	45.16	0.29	178.13	1.71

Mill speed of 78% of the critical:

	Speed		Toe		Shoulder		Torque		Power	
Particle Filling	Average	Standard deviation	Average	Standard deviation	Average	Standard deviation	Average	Standard deviation	Average	Standard deviation
%	%	%	Degrees	Degrees	Degrees	Degrees	Nm	Nm	watts	watts
0	78.68	0.36	156.57	2.21	303.65	3.21	44.90	0.31	207.92	1.32
20	77.25	0.12	158.12	2.39	301.81	3.28	47.25	0.22	224.56	1.15
40	78.28	0.20	158.56	2.07	305.53	6.77	48.55	0.21	233.80	1.06
60	78.25	1.01	169.94	5.77	308.38	7.13	49.89	0.94	240.15	1.49
70	77.75	0.14	158.69	3.81	313.07	11.58	49.96	0.23	238.96	1.09
80	75.63	1.65	156.97	3.66	302.95	3.75	49.99	1.07	232.54	1.48
90	78.31	0.15	156.38	2.04	302.05	3.04	50.05	0.30	241.14	1.58
100	79.16	0.16	173.10	5.68	303.71	2.70	48.47	0.23	236.12	1.19
110	78.15	0.42	171.77	5.10	304.21	3.07	47.21	0.37	226.99	1.27
120										
160	79.18401	0.118805087	172.3088	5.559119274	307.3533	3.545998762	47.06723	0.328323368	229.2931	1.508450538

Mill speed of 88% of the critical:

	Speed		Toe		Shoulder		Torque		Power	
Particle Filling	Average	Standard deviation	Average	Standard deviation	Average	Standard deviation	Average	Standard deviation	Average	Standard deviation
%	%	%	Degrees	Degrees	Degrees	Degrees	Nm	Nm	watts	watts
0	87.72	0.12	174.53	27.53	316.12	5.90	45.14	0.28	236.16	1.90
20	87.61	1.66	174.03	6.68	313.34	7.03	48.66	1.12	262.16	1.86
40	88.37	1.07	174.14	5.07	325.11	6.89	50.39	1.16	273.87	3.31
60	87.02	0.59	175.74	3.90	335.89	17.55	50.50	1.08	270.35	4.08
70	87.36	0.34	171.74	4.35	321.63	8.04	50.37	0.62	270.56	2.66
80	87.68	0.17	172.05	4.79	320.23	10.94	50.88	0.34	274.48	1.83
90	88.49	0.40	174.12	5.65	320.66	12.91	51.11	0.37	278.23	2.83
100	88.24	2.15	172.89	4.48	313.72	5.11	50.06	0.60	271.93	3.74
110	88.35	0.35	175.04	5.79	318.19	9.56	48.88	0.48	265.69	2.26
120	89.24	0.18	173.64	5.16	314.71	4.89	48.60	0.48	266.81	2.53
160	89.51	0.15	174.95	4.04	325.16	8.19	46.46	0.61	255.83	3.52

Mill speed of 98% of the critical:

	Speed		Toe		Shoulder		Torque		Power	
Particle Filling	Average	Standard deviation	Average	Standard deviation	Average	Standard deviation	Average	Standard deviation	Average	Standard deviation
%	%	%	Degrees	Degrees	Degrees	Degrees	Nm	Nm	watts	watts
0	96.84	2.00	167.41	5.47	334.32	7.46	45.73	0.47	269.81	2.56
20	97.59	1.05	174.08	4.24	316.07	8.71	49.04	1.52	292.11	1.97
40	98.59	0.17	175.05	4.74	328.15	8.30	47.17	0.40	286.20	2.42
60	98.52	0.77	Centrifuging occurs		Centrifuging occurs		39.42	1.27	239.59	7.70
70	96.90	2.67					42.69	3.54	255.75	21.31
80	98.86	0.17					38.46	1.73	233.93	10.52
90	98.95	0.14					40.46	1.78	246.30	10.76
100	99.65	0.15					40.46	1.03	248.02	6.28
110	99.54	0.12					41.57	0.44	254.61	2.73
120	99.15	0.18					41.67	0.53	254.24	3.32
160	98.42	0.14					36.24	0.80	219.47	4.77

APPENDIX 2

MORRELL'S POWER MODEL

A2

A2.1 MIXED CHARGE MODELLING

Morrell's C power model is based on the description of the load behaviour as seen in Figure A2.1. The toe (θ_T) and shoulder (θ_{Sh}) values used in Morrell's load behaviour model are for an angular coordinate system which has the 0^o at the 3 o'clock position and the angles increment in the anticlockwise direction to 360^o. This thesis employs the use of a coordinate system that starts at the 12 o'clock position which represents the 0^o angular position and increments anticlockwise to the 360^o angular position. The physical limits of the charge are defined by radial lines that extend from the toe and shoulder to the mill's centre, the charge inner surface radius (r_i) and the mill's internal radius (r_m).

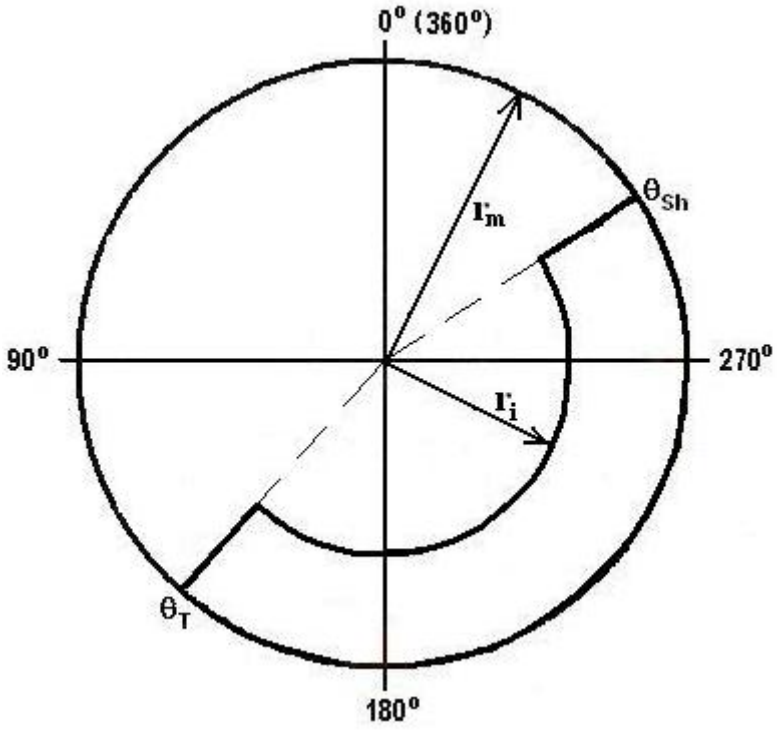


Figure A2.1: Morrell's C load behaviour model description

It is necessary to modify Morrell's original definitions of the toe and shoulder so as to be compatible with the coordinate system used at Wits. For the charge comprised of coarse particle the toe and shoulder models were modified to take into account the variations of the toe and shoulder angular positions with particle filling as seen below.

Toe:

$$\boldsymbol{\theta_T} = (\boldsymbol{A} + \boldsymbol{BN} + \boldsymbol{CU})\left(\mathbf{1} - \boldsymbol{e}^{-\boldsymbol{\beta}\left((\boldsymbol{D}+\boldsymbol{EN})-\boldsymbol{U}\right)}\right) \qquad \textbf{A2.1}$$

Shoulder:

$$\boldsymbol{\theta_{Sh}} = \mathbf{2}\boldsymbol{\pi} - (\boldsymbol{F} - \boldsymbol{GU})\boldsymbol{\theta_T} \qquad \textbf{A2.2}$$

Where:

A, B, C, D, E, F & G	Parameters determined by regression analysis	-
β	Parameter determined by regression analysis	-
N	Percentage of critical mill speed	%
U	Particle filling	%

Morrell's C power model which is based on the load behaviour description in Figure A2.1 is derived from an energy based method which sums the kinetic energy required to accelerate the balls in the toe region from rest to approximately the speed of the mill shell and the potential energy require

to raise the balls from the toe to the shoulder. The charge enclosed between the toe, shoulder and charge surface is assumed to be fully mixed. The net power drawn by the mill as described by Morrell (1997) is given by:

$$\boldsymbol{P_{net}} = \left[\frac{\pi g L \rho_c N_m r_m}{3(r_m - z r_i)}\left\{2r_m^3 - 3zr_m^2 r_i + r_i^3(3z-2)\right\}\{\sin\theta_{Sh} - \sin\theta_T\}\right] + \left[L\rho_c\left\{\frac{N_m r_m \pi}{(r_m - z r_i)}\right\}^3\left\{(r_m - z r_i)^4 - r_i^4(z-1)^4\right\}\right] \quad \textbf{A2.3}$$

Where:

P_{net}	Mill's net power draw	watts
g	Acceleration due to gravity	m/s^2
ρ_c	Charge density	Kg/m^3
N_m	Mill's rotational rate	rpm
r_m	Mill's internal radius	m
r_i	Charge inner surface radius	m
θ_{sh}	Shoulder's angular position	rad
θ_T	Toe's angular position	rad
J_T	Fractional mill filling	-
L	Mill's length	m

The empirically derived relationships in Morrell's net power are defined as:

Calculation of Z:

$$Z = (1 - J_t)^{0.4532} \quad \textbf{A2.4}$$

J_t corresponds to the fractional mill filling. For a ball mill with a particle filling less than 100% the fractional mill filling corresponds to the fraction of the mill's internal volume that the ball would occupy and at particle fillings greater than 100% the fractional filling corresponds to the fraction of the mill's internal volume that the whole charge would occupy.

Calculation of Charge inner surface, r_i:

The radial limit of the charge is defined by the position of the charge inner surface and is represented by the radial distance from the axis of rotation of the mill. From simple geometry together with the prior knowledge of the toe and shoulder angular positions and the volume of charge between these points the charge inner surface (r_i) can be given by:

$$r_i = r_m \left[1 - \left(\frac{2\pi\beta J_t}{2\pi+\theta_{Sh}-\theta_T}\right)\right]^{0.5} \quad \textbf{A2.5}$$

Where:

J_t	Fractional filling of the load	-
r_m	Mill's internal radius	m
β	Fraction of charge bound by toe, shoulder and the charge inner surface	-
θ_{Sh}	Shoulder's angular position	rad
θ_T	Toe's angular position	rad

To estimate the fraction of charge bound by the toe, shoulder and the charge inner surface (β), Morrell (1997) assumed that it was related to the

time taken for a particle to move between the toe and shoulder within the charge and between the shoulder and toe in free flight. Hence:

$$\beta = \frac{t_c}{t_f + t_c} \quad \textbf{A2.6}$$

Where:

t_c	Time taken to travel between the toe and shoulder within the active part of the charge	s
t_f	Time taken to travel between the shoulder and toe in freefall	s

The time taken to travel between the toe and shoulder within the active part of the charge is given by:

$$t_c \approx \left[\frac{\theta_{Sh} - \theta_T}{2\pi\bar{N}}\right] \quad \textbf{A2.7}$$

The above equation has been changed to suit wits coordinate system.

The mean value of the rotational rate of the active charge is given by:

$$\bar{N} = \frac{N_m}{2}$$

The time taken to travel between the shoulder and toe in freefall is given by:

$$t_f \approx \left[\frac{2\bar{r}(\sin\theta_{Sh} - \sin\theta_T)}{g}\right]^{0.5} \quad \textbf{A2.8}$$

The mean radial position of the active charge is given by:

$$\bar{r} = \frac{r_m}{2}\left[1 + \left(1 - \left(\frac{2\pi J_t}{2\pi + \theta_{Sh} - \theta_T}\right)\right)^{0.5}\right] \quad \textbf{A2.9}$$

Charge density, ρ_c

For particle fillings less than 100%:

$$\boldsymbol{\rho_C} = \boldsymbol{(1-\varepsilon)\rho_b} + \boldsymbol{(1-\varepsilon)\varepsilon\rho_p U} \quad \textbf{A2.10}$$

For particle fillings less than 100%:

$$\boldsymbol{\rho_C} = \frac{\boldsymbol{(1-\varepsilon)\rho_b + (1-\varepsilon)\varepsilon\rho_p U}}{\boldsymbol{1+\varepsilon(U-1)}} \quad \textbf{A2.11}$$

Where:

U	Particle filling	-
V_m	Mill's internal volume	m^3
ρ_b	Density of balls	kg/m^3
ρ_p	Density of silica particles	kg/m^3
ε	Voidage (0.4)	-

A2.2 CENTRIFUGED CHARGE MODELLING

Power drawn by active charge after centrifuging occurs:

After centrifuging the mill is viewed as a new mill with a reduced mill diameter. Figure A2.2 represents the situation where a part of the charge has centrifuged thus drawing no power and an active charge remains that draws power. The centrifuged layer is assumed to be of uniform thickness throughout the mills circumference. The void spaces between the centrifuged balls are assumed to contain silica sand. The centrifuged layer will reduce the mills diameter and alter the density of the load. The ball filling will be affected due to the reduction in the mill's diameter and a certain amount of balls centrifuging. It is anticipated that all these factors shall have a significant impact on the mill's power draw.

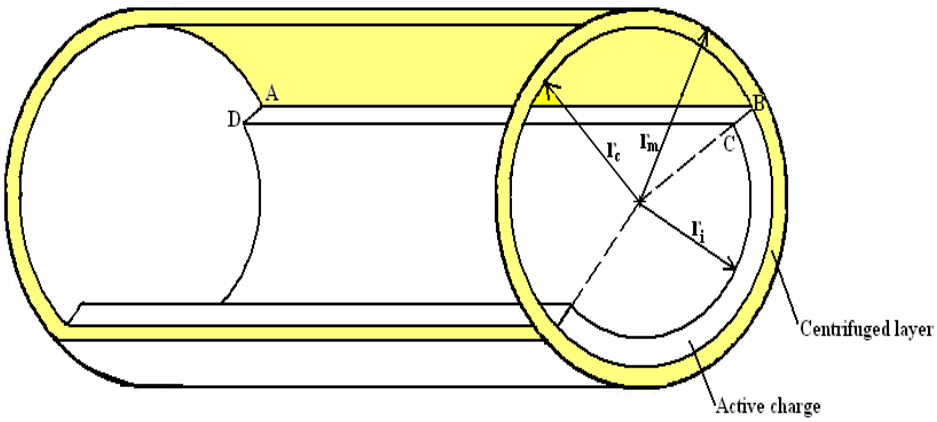


Figure A2.2: Illustration of the centrifuged layer model

From Figure A2.2, consider the element ABCD with length L and width dr.

The area of the element is given by:

$$Area = L.dr$$

The volumetric flowrate of particles with a tangential velocity V_r through the surface is given by:

$$Volumetric\ Flowrate = V_r.L.dr$$

The mass flowrate of the silica particle flowing through this surface is:

$$Mass\ Flowrate = \rho_{C,Active}.V_r.L.dr$$

The potential energy required to raise the particles from the toe to the shoulder is given by:

$$Potential\ Energy = g.h.\rho_{C,Active}.V_r.L.dr$$

Where: $h = r.(\sin\theta_{Sh} - \sin\theta_T)$

Thus:

$$Potential\ Energy = g.r.(\sin\theta_{Sh} - \sin\theta_T).\rho_{C,Active}.V_r.L.dr$$

The kinetic energy required to accelerate the balls from rest to the velocity of the mill shell is given by:

$$Kinetic\ Energy = \frac{V_r^3.\rho_{C,Active}.L.dr}{2}$$

The net power drawn by the segregated silica layer is the sum of the kinetic and potential energy.

$$P_{net,\ Active} = \int_{r_i}^{r_c} \left\{ g.r.(\sin\theta_{Sh} - \sin\theta_T).\rho_{C,Active}.V_r.L + \frac{V_r^3.\rho_{C,Active}.L}{2} \right\} dr \quad \textbf{2.12}$$

The tangential velocity of the particles is given by:

$$V_r = 2\pi N_r r \quad \textbf{A2.13}$$

Morrell suggested the following empirical expression for the mills rotational rate:

$$N_r = \frac{N_m.r_m.(r - zr_i)}{r(r_m - zr_i)} \quad \textbf{A2.14}$$

Thus substituting equation 2.14 into equation 2.13:

$$V_r = 2\pi \frac{N_m.r_m.(r - zr_i)}{(r_m - zr_i)} \quad \textbf{A2.15}$$

Substituting equation 2.15 into 2.12:

$$P_{net,\ Active} = \left[\frac{2\pi\rho_{C,Active} Lg(\sin\theta_{Sh} - \sin\theta_T) N_m r_m}{(r_m - zr_i)} \int_{r_i}^{r_c} r(r - zr_i) dr \right] + \left[\frac{4\pi^3 N_m^3 r_m^3 L \rho_{C,Active}}{(r_m - zr_i)^3} \int_{r_i}^{r_c} (r - zr_i)^3 dr \right] \quad \textbf{A2.16}$$

Performing the integration in equation 2.16:

$$\boldsymbol{P_{net,\ Active}} =$$

$$\left[\frac{\pi g L \rho_{C,Active} N_m r_m}{3(r_m - z r_i)}\left(2r_c^3 - 3zr_i\left(r_i^2 - r_c^2\right) - 2r_i^3\right)\left(\sin\theta_{Sh} - \sin\theta_T\right)\right] +$$

$$\left[L\rho_{C,Active}\left(\frac{N_m r_m \pi}{(r_m - z r_i)}\right)^3\left((r_c - z r_i)^4 - r_i^4(1-z)^4\right)\right] \qquad \textbf{A2.17}$$

Active charge density ($\rho_{C,\ Active}$):

For particle fillings less than 100%:

$$\boldsymbol{\rho_{C,Active}} = (1-\varepsilon)\rho_b + (1-\varepsilon)\varepsilon\rho_p U_{Actice\ Charge} \qquad \textbf{A2.18}$$

For particle fillings less than 100%:

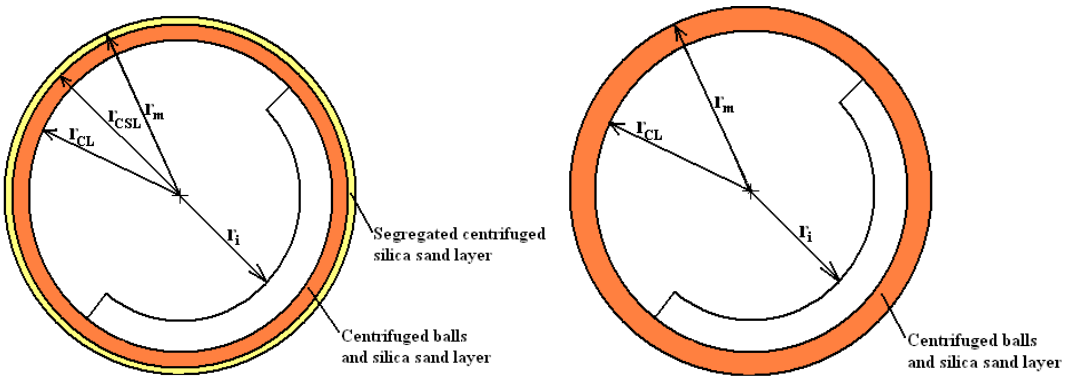
$$\boldsymbol{\rho_{C,Active}} = \frac{(1-\varepsilon)\rho_b + (1-\varepsilon)\varepsilon\rho_p U_{Active\ Charge}}{1+\varepsilon(U_{Active\ Charge} - 1)} \qquad \textbf{A2.19}$$

Where:

$U_{Active\ Charge}$	Particle filling of the active charge	-
ρ_b	Density of balls	kg/m^3
ρ_p	Density of silica particles	kg/m^3
ε	Voidage (0.4)	-

Active charge particle filling (U_{IL}):

When centrifuging occurs, the volume of particles in the active charge will be reduced by the amount of particles that have centrifuged. For centrifuging, in the case where segregation occurs (Coarse particles, N = 98%, U > 90%) it is assumed that a layer of segregated silica particles would centrifuge first followed by a layer steel balls containing particles in between the voids (Figure A2.3a). While for centrifuging where the charge is considered to be mixed (Fine particle, N = 98%, U > 40%) the centrifuged layer is considered to contain balls with particles present in the void spaces in between the balls (Figure A2.3b). In this study it is assumed that either the smallest ball size (6mm) or an average ball size (8mm) centrifuged. The particle filling will be affected by the centrifuging of particles. Likewise, the ball filling will be affected due to balls centrifuging and a reduction in the mills internal volume.



a) Segregated charge b) Mixed charge

Figure A2.3: Centrifuging of the charge for both segregated and mixed charge conditions

The particle filling for the active charge will be in both cases will be:

$$\boldsymbol{U_{Active\ Charge}} = \frac{\boldsymbol{V_{P,Active\ Charge}}}{\boldsymbol{\varepsilon(1-\varepsilon)J_{b,reduced}V_{m,reduced}}} \quad \textbf{A2.20}$$

Where:

$V_{P,\ Active\ Charge}$	Volume of particles in the active charge	m^3
$J_{b,\ reduced}$	Ball filling after centrifuging	-
$V_{m,\ reduced}$	Mill's internal volume after centrifuging	m^3
ε	Voidage	-

A) Segregated Centrifuged Charge

Calculation of the volume of silica particles in active charge ($V_{P,\ Active\ Charge}$):

The volume of silica particles in the active charge is the difference between the total volume of silica particles in the mill ($V_{P,\ Total}$) before centrifuging and the volume of particles in the centrifuged ball layer in between voids ($V_{P,\ CL}$) and the volume of segregated centrifuged particles ($V_{P,\ CSL}$).

$$V_{P,Active\ Charge} = V_{P,Total} - V_{P,CL} - V_{P,CSL} \quad \textbf{A2.21}$$

The total volume of particles present in the mill ($V_{P,\ Total}$) is:

$$V_{P,Total} = \varepsilon(1-\varepsilon)UJ_bV_m \quad \textbf{A2.22}$$

The volume of particles present in centrifuged ball voids ($V_{P,\ CL}$) is:

$$V_{P,CL} = \varepsilon\left(V_m - V_{OCL} - V_{lifters} - V_{CSL}\right)$$

$$V_{P,CL} = \varepsilon\left[\pi r_m^2 L - \pi L(r_m - \langle d_b + \Delta_s \rangle)^2 - 0.001056 - \left(\pi r_m^2 L - \pi(r_m - \Delta S)^2 L - 12\Delta S L(b_1 + b_2 + 2a)\right)\right]$$

A2.23

The volume of particles present in segregated and centrifuged silica layer ($V_{P,\,CSL}$) is:

$$V_{P,CSL} = \pi r_m^2 L - \pi(r_m - \Delta S)^2 L - 12\Delta S L(b_1 + b_2 + 2a) \quad \textbf{A2.24}$$

Thus substituting equations A2.22, A2.23 and A2.24 into A2.21 results into:

$$\boldsymbol{V_{P,Active\ Charge}} = [\boldsymbol{\varepsilon(1-\varepsilon)UJ_bV_m}] - \left[\boldsymbol{\varepsilon}\left[\boldsymbol{\pi r_m^2 L - \pi L(r_m - \langle d_b + \Delta_s \rangle)^2 - 0.001056} - \left(\boldsymbol{\pi r_m^2 L - \pi(r_m - \Delta S)^2 L - 12\Delta S L(b_1 + b_2 + 2a)}\right)\right]\right] - [\boldsymbol{\pi r_m^2 L - \pi(r_m - \Delta S)^2 L - 12\Delta S L(b_1 + b_2 + 2a)}] \quad \textbf{A2.25}$$

Where:

V_m	Mill's internal volume	m^3
V_{OCL}	Mills internal volume not occupied by centrifuged layer	m^3
$V_{lifters}$	Volume of lifters ($0.001056m^3$)	m^3
V_{CSL}	Volume of centrifuged segregated layer	m^3
d_b	Ball diameter	m

a, b_1, b_2	Dimensions of the trough between the lifters (a = 0.018m, b_1 = 0.003m and b_2 = 0.005m)	m
ΔS	Thickness of the segregated centrifuged silica layer	m

Calculation of the ball filling in the active charge ($J_{b,\ reduced}$):

From the definition of ball filling:

$$J_{b,reduced} = \frac{V_{b,left}}{(1-\varepsilon)V_{m,reduced}} \quad \textbf{A2.26}$$

The volume of balls left in the mill ($V_{b,\ left}$) after centrifuging can be calculated by:

$$V_{b,left} = V_{b,total} - V_{b,centrifuged} \quad \textbf{A2.27}$$

The total volume of balls in the mill ($V_{b,\ total}$) is given by:

$$V_{b,total} = (1-\varepsilon)J_b V_m \quad \textbf{A2.28}$$

The volume of balls centrifuged ($V_{b,\ centrifuged}$) is given by:

$$V_{b,centrifuged} = (1-\varepsilon)\left[V_m - V_{OCL} - V_{lifters} - V_{CSL}\right]$$

$$V_{b,centrifuged} = (1-\varepsilon)\left[\pi r_m^2 L - \pi L[r_m - (d_b + \Delta S)]^2 - 0.001056 - \right.$$

$$\pi rm2L - \pi rm - \Delta S2L - 12\Delta S Lb1 + b2 + 2a \quad \textbf{A2.29}$$

Substituting equations A2.28 and A2.29 into equation A2.27 then the volume of balls in the active charge will be:

$$V_{b,left} =$$

$$(1-\varepsilon)J_b V_m - \left[(1-\varepsilon)\left[\pi r_m^2 L - \pi L[r_m - (d_b + \Delta S)]^2 - 0.001056 - \left(\pi r_m^2 L - \pi(r_m - \Delta S)^2 L - 12\Delta S L(b_1 + b_2 + 2a)\right)\right]\right]$$

A2.30

Calculation of the reduced mill volume due to centrifuging ($V_{m,\,reduced}$):

The reduced mill volume due to centrifuging is given by:

$$V_{m,reduced} = \pi L\left(r_m - (d_b + \Delta S)\right)^2 \qquad \textbf{A2.31}$$

Evaluating equations A2.30 and A2.31 and substituting the results into equations A2.26 the ball filling of the active charge ($J_{b,\,reduced}$) can then be calculated for the segregated centrifuged charge.

B) Mixed Centrifuged Charge

Calculation of the volume of silica particles in active charge ($V_{P,\,Active\ Charge}$):

The volume of silica particles in the active charge is the difference between the total volume of silica particles in the mill ($V_{P,\,Total}$) before centrifuging and the volume of particles in the centrifuged ball layer in between voids ($V_{P,\,CL}$)

$$V_{P,Active\ Charge} = V_{P,Total} - V_{P,CL} \quad \textbf{A2.32}$$

The total volume of particles present in the mill ($V_{P,\ Total}$) is:

$$V_{P,Total} = \varepsilon(1-\varepsilon)UJ_bV_m \quad \textbf{A2.33}$$

The volume of particles present in centrifuged ball voids ($V_{P,\ CL}$) is:

$$V_{P,CL} = \varepsilon\left(V_m - V_{OCL} - V_{lifters}\right) \quad \textbf{A2.34}$$

$$V_{P,CL} = \varepsilon[\pi r_m^2 L - \pi L(r_m - d_b)^2 - 0.001056] \quad \textbf{A2.35}$$

Thus substituting equations A2.33 and A2.35 into equation A2.32 results in:

$$\boldsymbol{V_{P,Active\ Charge} = \varepsilon(1-\varepsilon)UJ_bV_m - \varepsilon[\pi r_m^2 L - \pi L(r_m - d_b)^2 - 0.001056]} \quad \textbf{A2.36}$$

Where:

V_m	Mill's internal volume	m^3
V_{OCL}	Mills internal volume not occupied by centrifuged layer	m^3
$V_{lifters}$	Volume of lifters ($0.001056m^3$)	m^3
d_b	Ball diameter	m

Calculation of the ball filling in the active charge ($J_{b,\ reduced}$):

From the definition of ball filling:

$$\boldsymbol{J_{b,reduced}} = \frac{\boldsymbol{V_{b,left}}}{\boldsymbol{(1-\varepsilon)V_{m,reduced}}} \quad \textbf{A2.37}$$

The volume of balls left in the mill ($V_{b,\ left}$) after centrifuging can be calculated by:

$$V_{b,left} = V_{b,total} - V_{b,centrifuged} \quad \textbf{A2.38}$$

The total volume of balls in the mill ($V_{b,\ total}$) is given by:

$$V_{b,total} = (1-\varepsilon)J_b V_m \quad \textbf{A2.39}$$

The volume of balls centrifuged ($V_{b,\ centrifuged}$) is given by:

$$V_{b,centrifuged} = (1-\varepsilon)\left[V_m - V_{OCL} - V_{lifters}\right]$$

$$V_{b,centrifuged} = (1-\varepsilon)[\pi r_m^2 L - \pi L[r_m - d_b]^2 - 0.001056] \quad \textbf{A2.40}$$

Thus the volume of balls in the active charge is given by substituting equations A2.39 and A2.40 into equation A2.37.

$$\boldsymbol{V_{b,left}} = \boldsymbol{(1-\varepsilon)J_b V_m - (1-\varepsilon)[\pi r_m^2 L - \pi L[r_m - d_b]^2 - 0.001056]} \quad \textbf{A2.41}$$

Calculation of the reduced mill volume due to centrifuging ($V_{m,\ reduced}$):

The reduced mill volume due to centrifuging is given by:

$$V_{m,reduced} = \pi L(r_m - d_b)^2 \qquad \textbf{A2.42}$$

Evaluating equations A2.41 and A2.42 and substituting the results into equations A2.37 the ball filling of the active charge ($J_{b,\ reduced}$) can then be calculated for the segregated centrifuged charge.

A2.3 SEGREGATED CHARGE MODELLING

The coarse silica charge experiences segregation. During segregation a layer of coarse silica particles is preferentially located at the periphery of the mill in contact with the mill shell and the thickness of this segregated layer increases with mill speed and particle filling. Morrell's depiction of the charge was modified to incorporate this segregated layer as seen in Figure A2.4 so that the effect of segregation on the net power drawn by the mill could be studied.

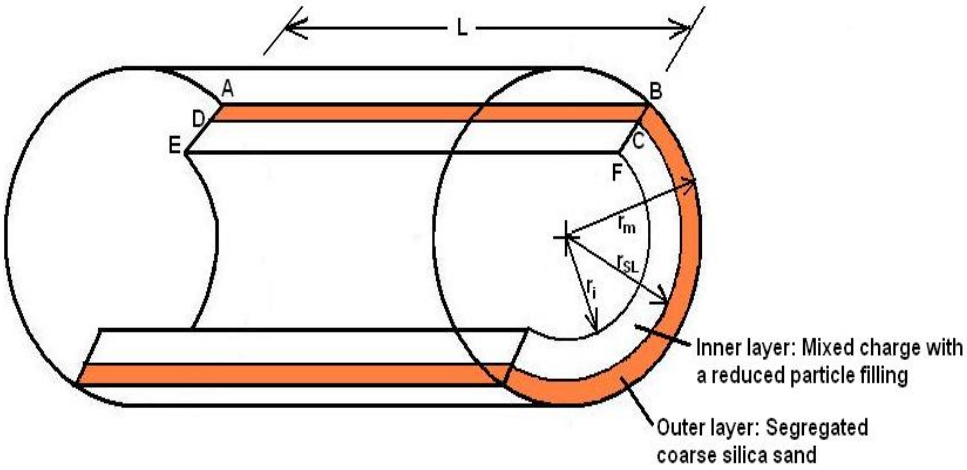


Figure A2.4: Morrell's C model description modified to account for segregation of coarse silica sand

It is assumed that the segregated outer layer contains silica sand only. The rest of the charge contained in the inner layer is well mixed and has a reduced particle filling. It is also assumed that no loss in rotational rate is experienced at the segregated layer interface (r_{SL}) that lies between the inner layer and the outer segregated layer.

The net power drawn by the mill is calculated by summing the net power drawn by the segregated silica outer layer and the power drawn by the mixed inner layer of the charge.

A) Power drawn by the segregated outer layer, $P_{net,\,OL}$:

From Figure A2.4, consider the element ABCD with length L and width dr.

The area of the element is given by:

$Area = L.dr$

The volumetric flowrate of particles with a tangential velocity V_r through the surface is given by:

$Volumetric\ Flowrate = V_r.L.dr$

The mass flowrate of the silica particle flowing through this surface is:

$Mass\ Flowrate = \rho_{silica}.V_r.L.dr$

The potential energy required to raise the particles from the toe to the shoulder is given by:

$Potential\ Energy = g.h.\rho_{silica}.V_r.L.dr$

Where: $h = r.(\sin\theta_{Sh} - \sin\theta_T)$

Thus:

$Potential\ Energy = g.r.(\sin\theta_{Sh} - \sin\theta_T).\rho_{silica}.V_r.L.dr$

The kinetic energy required to accelerate the balls from rest to the velocity of the mill shell is given by:

$$Kinetic\ Energy = \frac{V_r^3.\rho_{silica}.L.dr}{2}$$

The net power drawn by the segregated silica layer is the sum of the kinetic and potential energy.

$$P_{net,OL} = \int_{r_{sl}}^{r_m}\left\{g.r.(\sin\theta_{Sh} - \sin\theta_T).\rho_{silica}.V_r.L + \frac{V_r^3.\rho_{silica}.L}{2}\right\}dr \qquad \textbf{A2.43}$$

The tangential velocity of the particles is given by:

$$V_r = 2\pi N_r r \quad \textbf{A2.44}$$

Morrell suggested the following empirical expression for the mills rotational rate:

$$N_r = \frac{N_m . r_m . (r - zr_i)}{r(r_m - zr_i)} \quad \textbf{A2.45}$$

Thus substituting equation A2.45 into A2.44:

$$V_r = 2\pi \frac{N_m . r_m . (r - zr_i)}{(r_m - zr_i)} \quad \textbf{A2.45}$$

Substituting equation A2.45 into A2.43 results in:

$$P_{net,OL} = \left[\frac{2\pi\rho_{silica} Lg(\sin\theta_{Sh} - \sin\theta_T) N_m r_m}{(r_m - zr_i)} \int_{r_{Sl}}^{r_m} r(r - zr_i) dr\right] + \left[\frac{4\pi^3 N_m^3 r_m^3 L \rho_{silica}}{(r_m - zr_i)^3} \int_{r_{Sl}}^{r_m} (r - zr_i)^3 dr\right] \quad \textbf{A2.46}$$

Doing the integration on equation A2.46 results in:

$$\boldsymbol{P_{net,OL} = \left[\frac{\pi g L \rho_{silica} N_m r_m}{3(r_m - zr_i)} \left(2r_m^3 - 3zr_i\left(r_m^2 - r_{Sl}^2\right) - 2r_{Sl}^3\right)(\sin\theta_{Sh} - \sin\theta_T)\right] + \left[L\rho_{silica}\left(\frac{N_m r_m \pi}{(r_m - zr_i)}\right)^3 \left((r_m - zr_i)^4 - (r_{Sl} - zr_i)^4\right)\right]} \quad \textbf{A2.47}$$

B) Power drawn by the inner layer, $P_{net, IL}$:

From Figure A2.4, consider the element CDEF with length L and width dr. The area of the element is given by:

$$Area = L.dr$$

The volumetric flowrate of particles with a tangential velocity V_r through the surface is given by:

$$Volumetric\ Flowrate = V_r . L . dr$$

The mass flowrate of the silica particle flowing through this surface is:

$$Mass\ Flowrate = \rho_{C,IL}.V_r.L.dr$$

The potential energy required to raise the particles from the toe to the shoulder is given by:

$$Potential\ Energy = g.h.\rho_{C,IL}.V_r.L.dr$$

Where: $h = r.(\sin\theta_{Sh} - \sin\theta_T)$

Thus:

$$Potential\ Energy = g.r.(\sin\theta_{Sh} - \sin\theta_T).\rho_{C,IL}.V_r.L.dr$$

The kinetic energy required to accelerate the balls from rest to the velocity of the mill shell is given by:

$$Kinetic\ Energy = \frac{V_r^3.\rho_{C,IL}.L.dr}{2}$$

The net power drawn by the segregated silica layer is the sum of the kinetic and potential energy.

$$P_{net,OL} = \int_{r_i}^{r_{Sl}} \left\{ g.r.(\sin\theta_{Sh} - \sin\theta_T).\rho_{C,IL}.V_r.L + \frac{V_r^3.\rho_{C,IL}.L}{2} \right\} dr \qquad \textbf{A2.47}$$

The tangential velocity of the particles is given by:

$$V_r = 2\pi N_r r \qquad \textbf{A2.48}$$

Morrell suggested the following empirical expression for the mills rotational rate:

$$N_r = \frac{N_m.r_m.(r - zr_i)}{r(r_m - zr_i)} \qquad \textbf{A2.49}$$

Thus substituting equation A2.49 into A2.48 we get:

$$V_r = 2\pi \frac{N_m.r_m.(r - zr_i)}{(r_m - zr_i)} \qquad \textbf{A2.50}$$

Substituting equation A2.50 into A2.47 we get:

$$P_{net,IL} = \left[\frac{2\pi\rho_{C,IL}Lg(\sin\theta_{Sh}-\sin\theta_T)N_m r_m}{(r_m-zr_i)}\int_{r_i}^{r_{Sl}} r(r-zr_i)dr\right] + \left[\frac{4\pi^3 N_m^3 r_m^3 L\rho_{C,IL}}{(r_m-zr_i)^3}\int_{r_i}^{r_{Sl}}(r-zr_i)^3 dr\right] \quad \textbf{A2.51}$$

Doing the integration on equation A2.51:

$$\boldsymbol{P_{net,OL} = \left[\frac{\pi g L\rho_{C,IL}N_m r_m}{3(r_m-zr_i)}\left(2r_{SL}^3 - 3zr_i r_{Sl}^2 - r_i^3(3z-2)\right)(\sin\theta_{Sh}-\sin\theta_T)\right] + \left[L\rho_{C,IL}\left(\frac{N_m r_m \pi}{(r_m-zr_i)}\right)^3\left((r_{Sl}-zr_i)^4 - r_i^4(1-z)^4\right)\right]} \quad \textbf{A2.52}$$

Inner layer density ($\rho_{C,IL}$):

The occurrence of radial segregation causes a reduction in the particle filling for the inner layer. The density of the inner layer will then have to be recalculated to account for this reduction in the particle filling. The inner layer is assumed to be well mixed while the outer layer is assumed to contain silica sand only and has a uniform thickness.

For particle fillings less than 100%:

$$\boldsymbol{\rho_C = (1-\varepsilon)\rho_b + (1-\varepsilon)\varepsilon\rho_p U_{IL}} \quad \textbf{A2.53}$$

For particle fillings less than 100%:

$$\boldsymbol{\rho_C = \frac{(1-\varepsilon)\rho_b + (1-\varepsilon)\varepsilon\rho_p U_{IL}}{1+\varepsilon(U_{IL}-1)}} \quad \textbf{A2.54}$$

Where:

U_{IL}	Particle filling of inner layer	-
V_m	Mill's internal volume	m^3
ρ_b	Density of balls	kg/m^3

ρ_p	Density of silica particles	kg/m^3
ε	Voidage (0.4)	-

Inner layer particle filling (U_{IL}):

When segregation occurs, the volume of particles occupying the voids between the balls in the inner layer reduces by an equivalent volume of particles that have segregated to the outer layer. The new particle filling for the inner layer will be:

$$U_{IL} = \frac{V_{P,IL}}{\varepsilon(1-\varepsilon)J_b V_m} \quad \textbf{A2.55}$$

Where:

$V_{P,\,IL}$	Volume of particles in the inner layer	m^3
J_b	Ball filling	-
V_m	Mill's internal volume	m^3
ε	Voidage	-

The volume of particles in the inner layer is the difference between the total volume of particles in the mill ($V_{P,\,Total}$) and the volume of particles in the segregated outer layer ($V_{P,\,OL}$).

$$V_{P,IL} = V_{P,Total} - V_{P,OL} \quad \textbf{A2.56}$$

The total volume of particles present in the mill is given by:

$$V_{P,Total} = \varepsilon(1-\varepsilon)UJ_b V_m \quad \textbf{A2.57}$$

The total volume of particles in the segregated layer has to be derived from the geometry of the segregated layer. Considering Figure A2.5, the charge is bound by sector OAB subtended by an angle θ. The angle θ is obtained by the difference between the toe and shoulder angular positions.

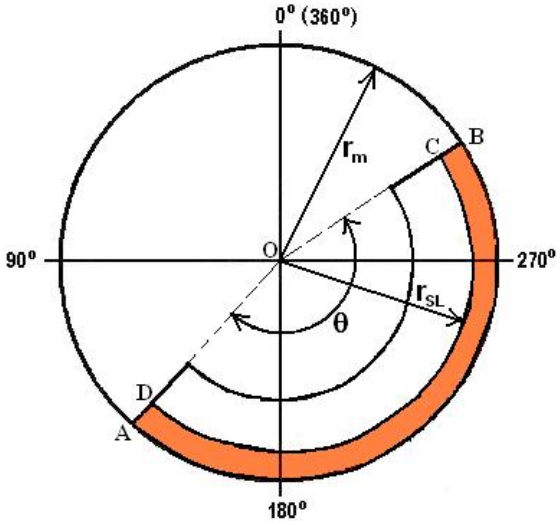


Figure A2.5: Morrell's C model geometry

From the above geometry:

$$Area\ of\ segregated\ outer\ layer\ =\ \frac{1}{2}\theta(r_m^2 - r_{Sl}^2) \qquad \textbf{A2.58}$$

$$Volume\ of\ segregated\ outer\ layer\ =\ \frac{1}{2}\theta L(r_m^2 - r_{Sl}^2) \qquad \textbf{A2.59}$$

$$Volume\ of\ particles\ in\ segregated\ outer\ layer\ \left(V_{P,OL}\right)\ =\ \frac{1}{2}\theta L(1 - \varepsilon)(r_m^2 - r_{Sl}^2) \qquad \textbf{A2.60}$$

The segregated layer radius (r_{SL}) varies with mills speed and particle filling increment. Thus

$$r_{SL} = r_m - \sigma\Delta R_{Inductive} \qquad \textbf{A2.61}$$

Where:

s	Radial segregation index	-
$\Delta R_{inductive}$	Inductive proximity probe's measuring range (0.005m)	m

Incorporating the definition of the segregated layer radius (equation A2.61) into the definition of the volume of particles in the segregated layer (equation A2.60) we obtain the following:

$$V_{P,OL} = \frac{1}{2}\theta\sigma\Delta R_{inductive} L(1-\varepsilon)(2r_m - \sigma\Delta R_{inductive}) \quad \textbf{A2.62}$$

Looking back at the definition of particle filling in the inner layer (equation A2.55) and incorporating the definitions for volume of particles in the inner layer (equation A2.56) we then obtain:

$$\boldsymbol{U_{IL}} = \frac{\boldsymbol{\varepsilon U J_b V_m - \frac{1}{2}\theta\sigma\Delta R_{inductive} L(2r_m - \sigma\Delta R_{inductive})}}{\boldsymbol{\varepsilon J_b V_m}} \quad \textbf{A2.63}$$

Thus including the definition of particle filling in the inner layer (equation A2.63) into that of the density of the inner layer when segregation occurs (equation A2.53 & A2.54); the density of the inner layer can be calculated.

The total net power for the charge will be given by:

$$\boldsymbol{P_{net} = P_{net,IL} + P_{net,OL}} \quad \textbf{A2.64}$$

A2.4 POOL POWER MODELLING USING SIMPSON'S METHOD

The pool shown in Figure A2.6 is assumed to contain only fine silica sand. The symmetrical portion of the pool does not draw any power as the torque from the two halves separated by the Y axis counter each other's effects. The additional mass shall only have an effect on the bearing pressure. The particles present in the toe portion of the pool exert a counter torque to the loads torque thus reducing its net torque and power draw.

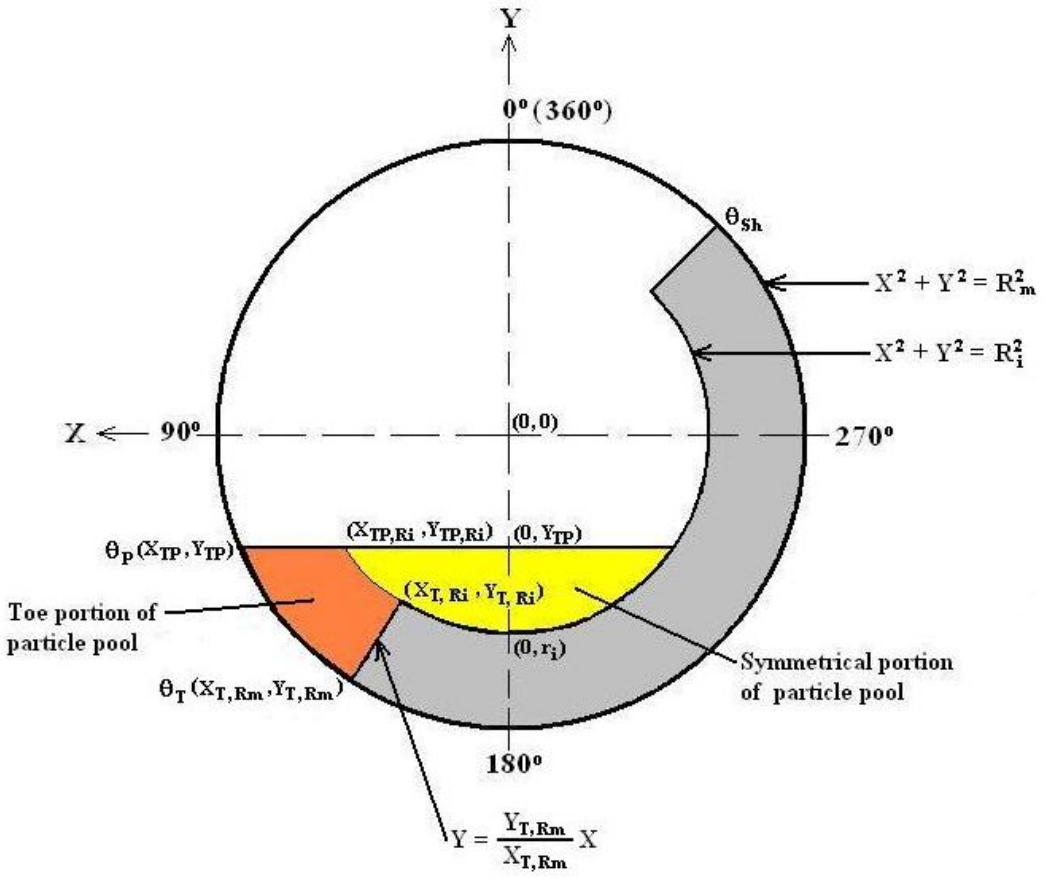


Figure A2.6: Illustration of the particle pool model

Assumptions:

- The maximum load density occur at the particle filling (U) of 100%. At this maximum density the void spaces between the balls are completely filled with particles.
- Pool formation begins at a particle filling greater than 100%. The density of the load remains constant and maximum at particle filling greater than 100%.
- The pool consists of silica particles only

Coordinates defining the boundary of the pool:

The coordinates defining the boundary of the toe portion of the particle pool are $\theta_p(X_{TP}, Y_{TP})$, $\theta_T(X_{T,Rm}, Y_{T,Rm})$, $(X_{TP,Ri}, Y_{TP,Ri})$ and $(X_{T,Ri}, Y_{T,Ri})$ and the indicated in Figure A2.6. The evaluations of the coordinates are:

Coordinates for the Toe, θ_T

At the mill radius r_m:

$$X_{T,Rm} = r_m \sin(\pi - \theta_T)$$

$$Y_{T,Rm} = r_m \cos(\pi - \theta_T)$$

At the charge inner radius r_i:

$$X_{T,Ri} = r_i \sin(\pi - \theta_T)$$

$$Y_{T,Ri} = r_i \cos(\pi - \theta_T)$$

Coordinates for the pool, θ_p:

At the mill radius r_m:

$$X_{TP} = \sqrt{(r_m^2 - Y_{TP}^2)}$$

$$\theta_P = \tan^{-1}\left(\frac{X_{TP}}{Y_{TP}}\right)$$

$Y_{T\ P}$: This is obtained by iterations of the pools height in the Simpsons method when the calculated volume of the pool by the Simpsons

method is equal to the volume of the excess particles above a particle filling of 100%.

At the charge inner radius r_i:

$$X_{TP,Ri} = \sqrt{(r_i^2 - Y_{TP}^2)}$$

Assuming the particle pool's surface is at the same level then:

$$Y_{TP,Ri} = Y_{TP}$$

Other important coordinates:

Minimum depth of the symmetrical pool: (0, r_i)

Maximum height of the pool: (0, Y_{TP})

Equation of the line through the origin and coordinates ($X_{T, Rm}$, $Y_{T, Rm}$):

$$Y = \left(\frac{Y_{T,Rm}}{X_{T,Rm}}\right) X$$

1. Calculation of the pool mass and volume:

For particle fillings greater than 100% the mass of particles present in the pool is:

$$m_{p,pool} = \varepsilon(1-\varepsilon) J_b \rho_p V_m (U_{U>100\%} - U_{100\%}) \quad \textbf{A2.65}$$

Thus the volume of the pool will be:

$$V_{pool} = \varepsilon J_b V_m (U_{U>100\%} - U_{100\%}) \quad \textbf{A2.66}$$

Where:

J_b	Ball filling	-
V_m	Mill's internal volume	m^3
$U_{U>100\%}$	Fraction of particle filling greater than 100%	-

$U_{U=100\%}$	Fraction of particle filling at 100%	-
ε	Voidage	-
ρ_p	Particle density	kg/m^3

2. Calculation of the pools centre of gravity:

The volume of the pool calculated above combines the toe portion and the symmetrical portion depending on the height of the pool. The toe portion of the pool is responsible for the power loss. The centre of gravity that is being calculated here is only for the toe portion of the pool. In Figure A2.6 the toe portion of the pool is divided into two sections, A and B. The derivation of the pools centre of gravity is drawn up by considering these two sections separately.

Centre of gravity of Section A:

In Figure A2.6, consider an element of width b and length L in section A of the toe portion of the particle pool. An exploded view of the element in consideration can be viewed in Figure A2.7 below and is split into two parts each having a mass m_1 and m_2.

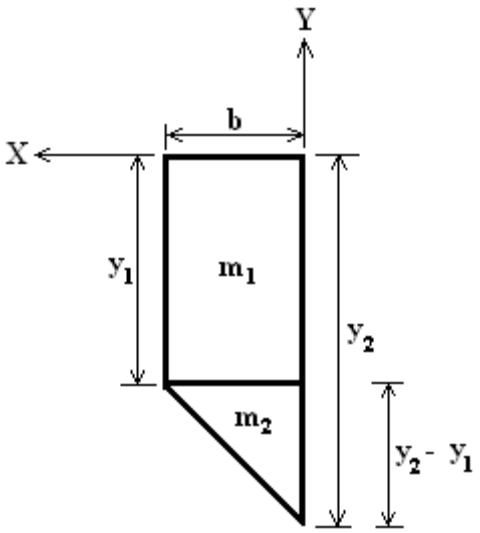


Figure A2.7: Illustration of an element in the toe portion of the pool

Mass of the element

The mass of the rectangular section of the element is given by:

$$m_{A,rectangle} = by_1 L\rho_p \quad \textbf{A2.67}$$

The mass of the triangular section of the element is given by:

$$m_{B,triangle} = \frac{1}{2} b(y_2 - y_1) L\rho_p \quad \textbf{A2.68}$$

Thus the total mass of the element is given by given by the sum of equations A2.27 and A2.68:

$$\boldsymbol{m_{total} = \frac{1}{2} bL\rho_p (y_1 + y_2)} \quad \textbf{A2.69}$$

Generally for each element's mass it can be expressed as:

$$\boldsymbol{m_{A,i} = \frac{1}{2} bL\rho_b (y_i + y_{i+1})} \quad \textbf{A2.70}$$

Moment of the element about the Y – axis

The moment of the element is given by:

$$C_x = \frac{\sum_1^2 m_{A,i} y_i}{\sum_1^2 m_{A,i}} \quad \textbf{A2.71}$$

Using the dimensions of the element we obtain

$$C_x = \frac{\left(by_1 L\rho_b \left(\frac{b}{2}\right)\right) + \left(\frac{1}{2} b(y_2 - y_1) L\rho_p \left(\frac{b}{3}\right)\right)}{\frac{1}{2} bL\rho_b (y_1 + y_2)} \quad \textbf{A2.72}$$

Simplifying equation A2.72 we get:

$$\boldsymbol{C_x = \frac{b(2y_1 + y_2)}{3(y_1 + y_2)}} \quad \textbf{A2.73}$$

The moment about the Y-axis of each element in section A of the toe portion of the pool ($C_{XA,\,i}$) is given by the sum of the distance of an element from the Y axis ($X_{A,\,i}$) and the moment of the element. This is expressed as:

$$C_{XA,i} = X_{A,i} + \frac{b[2y_i + y_{i+1}]}{3[y_i + y_{i+1}]} \quad \textbf{A2.74}$$

The centre of gravity for section A is then given by:

$$C_{XA} = \frac{\sum_{i=1}^{n}(m_{A,i}C_{XA,i})}{\sum_{i=1}^{n} m_{A,i}} \quad \textbf{A2.75}$$

Centre of gravity of Section B:

In Figure A2.6, consider an element of width b and length L in section A of the toe portion of the particle pool. An exploded view of the element in consideration can be viewed in Figure A2.8 below and is split into two parts each having a mass m_1 and m_2.

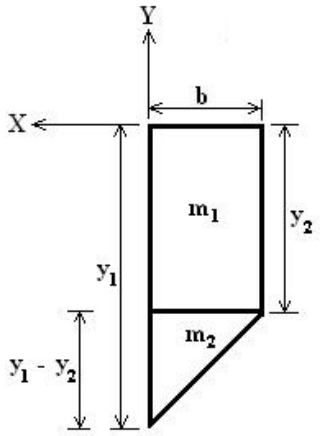


Figure A2.8: Illustration of an element in the toe portion of the pool

Mass of the element

The mass of the rectangular section of the element is given by:

$$m_{B,rectangle} = by_2L\rho_p \quad \textbf{A2.76}$$

The mass of the triangular section of the element is given by:

$$m_{B,traingle} = \frac{1}{2}b(y_1 - y_2)L\rho_p \quad \textbf{A2.77}$$

Thus the total mass of the element is given by given by:

$$\boldsymbol{m_{total} = \frac{1}{2} bL\rho_p(y_1 + y_2)} \quad \textbf{A2.78}$$

Generally for each element's mass it can be expressed as:

$$\boldsymbol{m_{B,i} = \frac{1}{2} bL\rho_b(y_i + y_{i+1})} \quad \textbf{A2.79}$$

Moment of the element about the Y – axis

The moment of the element about the Y – axis is given by:

$$C_x = \frac{\sum_1^2 m_{B,i} y_i}{\sum_1^2 m_{B,i}} \quad \textbf{A2.80}$$

Using the dimensions of the element we obtain

$$C_x = \frac{\left(by_2 L\rho_b\left(\frac{b}{2}\right)\right) + \left(\frac{1}{2}b(y_1 - y_2)L\rho_p\left(\frac{2b}{3}\right)\right)}{\frac{1}{2}bL\rho_b(y_1 + y_2)} \quad \textbf{A2.81}$$

Simplifying

$$\boldsymbol{C_x = \frac{b(2y_1 - 3y_2)}{3(y_1 + y_2)}} \quad \textbf{A2.82}$$

The moment about the Y-axis of each element in section B of the toe portion of the pool ($C_{XB,\,i}$) is given by the sum of the distance of an element from the Y axis ($X_{B,\,i}$) and the moment of the element. This is expressed as:

$$\boldsymbol{C_{XB,i} = X_{B,i} + \frac{b[2y_i - 3y_{i+1}]}{3[y_i + y_{i+1}]}} \quad \textbf{A2.83}$$

The centre of gravity for section B is then given by:

$$\boldsymbol{C_{XB} = \frac{\sum_{i=1}^{n}(m_{B,i} C_{XB,i})}{\sum_{i=1}^{n} m_{B,i}}} \quad \textbf{A2.84}$$

Thus the centre of gravity for the toe portion of the pool is given by:

$$\boldsymbol{C_X = \frac{m_A C_{XA} + m_B C_{XB}}{m_A + m_B}} \quad \textbf{A2.85}$$

Where:

$$m_A = \sum_{i=1}^{n} m_{A,i}$$

$$m_B = \sum_{i=1}^{n} m_{B,i}$$

3. Calculation of the pools torque and power

From the definition of torque:

$$T = mgd \qquad \textbf{A2.86}$$

Thus the pools torque is given by:

$$\boldsymbol{T_{pool} = (m_A + m_B) g C_X} \qquad \textbf{A2.87}$$

The pools power is given by:

$$\boldsymbol{P_{pool} = \frac{2\pi N T_{pool}}{60}} \qquad \textbf{A2.88}$$

A2.5 MATLAB PROGRAM: POOL'S TORQUE AND POWER

```
%% Pool_Torq Program
%% This program calculates the torque drawn by a pool in a batch ball mill
%% using Numerical methods

clear all
clc

%%Initialisation of variables

Ri = 0; Rm = 0.263; theta_T = 0; U = 0; Umax = 1; J = 0; Vm = 0; rho_P =
0; X_TRm = 0; Y_TRm = 0; X_TRi = 0; Y_TRi = 0; del_U = 0; Mp = 0; Ep =
0.4; Vpl = 0; Va = 0;Vb = 0; Vc = 0; Vd = 0; Ve = 0; Vf = 0; Vg = 0; Vh = 0;
Vj = 0; a = 0.001; X_Tp = 0; X_Tl = 0; b = 0; n = 0; incr = 1; V_meas = 0;
Vpool = 0; V_simp = 0; Y_even = 0; Y_odd = 0; Lm = 0; ind = 0; Y_Tp = 0;
Y_Tp1 = 0; Ya_even = 0; Ya_odd = 0; Yb_even = 0; Yb_odd = 0; Yc_even
= 0; Yc_odd = 0; Yd_even = 0; Yd_odd = 0;Ya = 0; Yb = 0;Yc = 0;

% User defined variables
Rm = 0.263; %input('Enter value for the mill internal radius (meters) :');
Lm = 0.18; %input('Enter value for the mill length (meters) :');
Ri = 0.202811; %input('Enter value for the charge internal radius (meters)
:');
N_rpm = 51.78444;
theta_T = 137.2109; %input('Enter value for the toe`s angular position
(degrees) :');
U = 160/100; %(input('Enter value for the particle filling (%) :'))/100;
J = 20/100; %(input('Enter value for the ball filling (%) :'))/100;
Vm = 0.0387; %input('Enter value for the mills internal volume (m^3) :');
rho_P = 2466.667; %input('Enter value for the particle density (kg/m^3) :');
a = 0.0000001; %input('Enter value for the pool height (m) (Default =
0.0001) :');
n = 1000; %input('Enter number of strips to be created (default 1000) :');

%% Conversion of the toe coordinates of the load to cartesian coordinates

%Toe coordinates at the mill shell
X_TRm = Rm*sin(pi-((pi/180)*theta_T));
Y_TRm = Rm*cos(pi - ((pi/180)*theta_T));

%Toe coerdinates at the charge inner surface radius
X_TRi = Ri*sin(pi-((pi/180)*theta_T));
Y_TRi = Ri*cos(pi - ((pi/180)*theta_T));

 %% Calculation of the pools mass and volume
```

```
% Pool Mass
del_U = U - Umax;
Mp = Ep*(1 - Ep)*J*rho_P*Vm*del_U;

%Pool Volume
V_meas = 0.4*Ep*J*Vm*del_U; % Experimatally determined pool volume
from particles filling


% Calculation of the pools volume
% This is the first part of the calculation of the center of gravity of the
% toe pool. The condition that has to be met when generating the pool is
% that the Experimentally determined pool vulme V_meas should equal
the
% pool volume generated by Simpson`s rule V_pool.

Y_Tp = Y_TRm; %Setting the pool height to be equal to the toe`s Y coord.


while (V_meas - Vpool) >=  0   %Dummy

    Y_Tp = Y_Tp - a; % Increase the pool height

    if Y_TRm >= Ri % Check if the symetrical pool is present

        if Y_Tp >= Ri % Check if the symetrical pool is present


            Ya_even = 0;
            Ya_odd  = 0;
            Yb_even = 0;
            Yb_odd  = 0;

            X_Tp = sqrt((Rm^2)-(Y_Tp^2)); %Initial X coordinate of the pool
            X_Tl = (X_TRm/Y_TRm)*Y_Tp; % Final X coordinate of the pool

            b = (X_Tp - X_TRm)/n; % Width of the strip for toe pool A
            c = (X_TRm - X_Tl)/n; % width of the strip for toe pool B

                for k = 1:(n+1) % Loop to define the x coord and calc the
                                %corresponding y coord

                    %Calculation of the Y coordinates of toe pool A
                    Xa(k) = X_Tp - ((k-1)*b); % x coord of toe pool A
                    Ya(k) = sqrt((Rm^2) - (Xa(k)^2)) - Y_Tp; % y coord of
                                                             %toe pool A
```

```
            odd = ((k/2)-fix(k/2));

            if (odd == 0)&(k ~= (n+1))&(k>1)% Sorts out and adds up
                                    %the Y coord with odd
                                    %indices excluding Y(1)
                                    % and Y(n)
               Ya_even = Ya(k) + Ya_even;
            end

            if (odd > 0)&(k ~= (n+1))&(k>1)% Sorts out and adds up
                                   %the Y coord with even
                                   %indices excluding Y(1)
                                   %and Y(n)
               Ya_odd = Ya(k) + Ya_odd;
            end


            % Calculation of the Y coordinate of toe pool B
            Xb(k) = X_TRm - ((k - 1)*c); % x coord of toe pool B
            Yb(k) = ((Y_TRm/X_TRm)*Xb(k)) - Y_Tp; % y coord of toe
pool B

            odd = ((k/2)-fix(k/2));

            if (odd == 0)&(k ~= (n+1))&(k>1)% Sorts out and adds up
                                    %the Y coord with odd
                                    %indices excluding Y(1) and Y(n)
               Yb_even = Yb(k) + Yb_even;
            end

            if (odd > 0)&(k ~= (n+1))&(k>1)% Sorts out and adds up
                                   %the Y coord with even
                                   %indices excluding Y(1) and Y(n)
               Yb_odd = Yb(k) + Yb_odd;
            end
         end

         % Calculation of the pool volume by Simpsons Rule
         Va = b/3*Lm*((Ya(1)+Ya((n+1))) + (4*Ya_even)+(2*Ya_odd));
         Vb = c/3*Lm*((Yb(1)+Yb((n+1))) + (4*Yb_even)+(2*Yb_odd));
      end

      if (Y_Tp < Ri)&(Y_Tp >= Y_TRi)

         Ya_even = 0;
         Ya_odd  = 0;
         Yb_even = 0;
```

```
Yb_odd  = 0;
Yc_even = 0;
Yc_odd = 0;

X_Tp = sqrt((Rm^2)-(Y_Tp^2));
X_Tl = X_TRm/Y_TRm*Y_Tp;
X_Sp = sqrt((Ri^2)-(Y_Tp^2));

b = (X_Tp - X_TRm)/n;
c = (X_TRm - X_Tl)/n;
f = X_Sp/n;

   for k = 1:(n+1)

      Xa(k) = X_Tp - ((k-1)*b);
      Ya(k) = sqrt((Rm^2)-(Xa(k)^2))-Y_Tp;

      odd = ((k/2)-fix(k/2));

      if (odd == 0)&(k ~= (n+1))&(k>1)% Sorts out and adds up
                                      %the Y coord with odd indices
                                      %excluding Y(1) and Y(n)
         Ya_even = Ya(k) + Ya_even;
      end

      if (odd > 0)&(k ~= (n+1))&(k>1)% Sorts out and adds up
                                     %the Y coord with even indices
                                     %excluding Y(1) and Y(n)
         Ya_odd = Ya(k) + Ya_odd;
      end


      Xb(k) = X_TRm - ((k-1)*c);
      Yb(k) = ((Y_TRm/X_TRm)*Xb(k)) - Y_Tp;

      if (odd == 0)&(k ~= (n+1))&(k>1)% Sorts out and adds up
                                      %the Y coord with odd indices
                                      %excluding Y(1) and Y(n)
         Yb_even = Yb(k) + Yb_even;
      end

      if (odd > 0)&(k ~= (n+1))&(k>1)% Sorts out and adds up
                                     %the Y coord with even indices
                                     %excluding Y(1) and Y(n)
         Yb_odd = Yb(k) + Yb_odd;
      end
```

```
            Xc(k) = X_Sp - ((k-1)*f);
            Yc(k) = sqrt((Ri^2)-(Xc(k)^2))-Y_Tp;

            if (odd == 0)&(k ~= (n+1))&(k>1)% Sorts out and adds up
                                            %the Y coord with odd indices
                                            %excluding Y(1) and Y(n)
               Yc_even = Yc(k) + Yc_even;
            end

            if (odd > 0)&(k ~= (n+1))&(k>1)% Sorts out and adds up
                                           %the Y coord with even indices
                                           %excluding Y(1) and Y(n)
               Yc_odd = Yc(k) + Yc_odd;
            end
         end

         % Calculation of the pool volume using Simpson rule
         Va = b/3*Lm*((Ya(1)+Ya((n+1))) + (4*Ya_even)+(2*Ya_odd));
         Vb = c/3*Lm*((Yb(1)+Yb((n+1))) + (4*Yb_even)+(2*Yb_odd));
         Vc = 2*f/3*Lm*((Yc(1)+Yc((n+1)))+(4*Yc_even)+(2*Yc_odd));
end

if (Y_Tp < Y_TRi) & (Y_Tp >= 0)

   Ya_even = 0;
   Ya_odd  = 0;
   Yb_even = 0;
   Yb_odd  = 0;
   Yc_even = 0;
   Yc_odd = 0;
   Yd_even = 0;
   Yd_odd = 0;

   X_Tp = sqrt((Rm^2)-(Y_Tp^2));
   X_Sp = sqrt((Ri^2) - (Y_Tp^2));

   b = (X_Tp - X_TRm)/n;
   c = (X_TRm - X_TRi)/n;
   f = X_TRi/n;
   g = X_Sp/n;

   for k = 1:(n+1)

            Xa(k) = X_Tp - ((k-1)*b);
            Ya(k) = sqrt((Rm^2)-(Xa(k)^2))-Y_Tp;
```

```
odd = ((k/2)-fix(k/2));

if (odd == 0)&(k ~= (n+1))&(k>1)% Sorts out and adds up
                                 %the Y coord with odd indices
                                 % excluding Y(1) and Y(n)
   Ya_even = Ya(k) + Ya_even;
end

if (odd > 0)&(k ~= (n+1))&(k>1)% Sorts out and adds up
                               %the Y coord with even indices
                               %excluding Y(1) and Y(n)
   Ya_odd = Ya(k) + Ya_odd;
end


Xb(k) = X_TRm - ((k-1)*c);
Yb(k) = (((Y_TRm/X_TRm)*Xb(k)) - Y_Tp);

if (odd == 0)&(k ~= (n+1))&(k>1)% Sorts out and adds up
                                 %the Y coord with odd indices
                                 %excluding Y(1) and Y(n)
   Yb_even = Yb(k) + Yb_even;
end

if (odd > 0)&(k ~= (n+1))&(k>1)% Sorts out and adds up
                               %the Y coord with even indices
                               %excluding Y(1) and Y(n)
   Yb_odd = Yb(k) + Yb_odd;
end


Xc(k) = X_TRi - ((k-1)*f);
Yc(k) = sqrt((Ri^2)-(Xc(k)^2))-Y_Tp;

if (odd == 0)&(k ~= (n+1))&(k>1)% Sorts out and adds up
                                 %the Y coord with odd indices
                                 %excluding Y(1) and Y(n)
   Yc_even = Yc(k) + Yc_even;

end

if (odd > 0)&(k ~= (n+1))&(k>1)% Sorts out and adds up
                               %the Y coord with even indices
                               %excluding Y(1) and Y(n)
   Yc_odd = Yc(k) + Yc_odd;

end
```

```
            Xd(k) = 0 - ((k-1)*g);
            Yd(k) = sqrt((Ri^2)-((Xd(k))^2))-Y_Tp;

            if (odd == 0)&(k ~= (n+1))&(k>1)% Sorts out and adds up
                                            %the Y coord with odd indices
                                            %excluding Y(1) and Y(n)
               Yd_even = Yd(k) + Yd_even;

            end

            if (odd > 0)&(k ~= (n+1))&(k>1)% Sorts out and adds up
                                           %the Y coord with even indices
                                           %excluding Y(1) and Y(n)
               Yd_odd = Yd(k) + Yd_odd;

            end
        end
        % Calculation of the pool volume using Simpson rule
        Va = b/3*Lm*((Ya(1)+Ya(n+1)) + (4*Ya_even) + (2*Ya_odd));
        Vb = c/3*Lm*((Yb(1)+Yb(n+1)) + (4*Yb_even) + (2*Yb_odd));
        Vc = f/3*Lm*((Yc(1)+Yc(n+1)) + (4*Yc_even) + (2*Yc_odd));
        Vd = g/3*Lm*((Yd(1)+Yd(n+1)) + (4*Yd_even) + (2*Yd_odd));

    end

    Vpool = Va + Vb+ Vc+ Vd;

elseif Y_TRm < Ri % If the Toe Pool is above the inner surface radius

    if (Y_Tp >= Y_TRm) & (Y_Tp < Ri) % Is the pool height between
                                     % the toe Y coordinate and the
                                     % charge inner surface radius?
        Ye_even = 0;
        Ye_odd = 0;

        X_Sp = sqrt((Ri^2)-(Y_Tp^2));
        h = X_Sp/n;


        for k = 1:(n+1)

            %Calculation of the Y coordinates of the pool
            Xe(k) = X_Sp - ((k-1)*h);
            Ye(k) = (sqrt((Ri^2)-(Xe(k)^2)))- Y_Tp;

            odd = ((k/2)-fix(k/2));
```

```
        if (odd == 0)&(k ~= (n+1))&(k>1)% Sorts out and adds up
                                        %the Y coord with odd indices
                                        % excluding Y(1) and Y(n)
            Ye_even = Ye(k) + Ye_even;
        end

        if (odd > 0)&(k ~= (n+1))&(k>1)% Sorts out and adds up
                                       %the Y coord with even indices
                                       %excluding Y(1) and Y(n)
            Ye_odd = Ye(k) + Ye_odd;

        end
    end
    % Calculation of the volume of the symetrical pool
    Ve = 2*h/3*Lm*((Ye(1)+Ye(n+1))+(4*Ye_even)+(2*Ye_odd));
end

if (Y_Tp < (Y_TRm-a))  %Is pool height greater than the
                %Y coordinate of the toe's angular position?
Ve = 0;
Yf_even = 0;
Yf_odd = 0;
Yg_even = 0;
Yg_odd = 0;
Yh_even = 0;
Yh_odd = 0;
Yj_even = 0;
Yj_odd = 0;

X_Tp = sqrt((Rm^2)-(Y_Tp^2));
X_Tl = (X_TRm/Y_TRm)*Y_Tp;
X_Sp = sqrt((Ri^2)-(Y_Tp^2));

l = (X_Tp - X_TRm)/n;
m = (X_TRm - X_Tl)/n;
p = X_TRi/n;
q = X_Sp/n;

for k = 1:(n+1)

    % Calculations for toe pool A
    Xf(k) = X_Tp - ((k-1)*l);
    Yf(k) = sqrt((Rm^2)- (Xf(k)^2)) - Y_Tp;

    odd = ((k/2)-fix(k/2));
    if (odd == 0)&(k ~= (n+1))&(k>1)% Sorts out and adds up
```

```
                        % the Y coord with odd indices
                        % excluding Y(1) and Y(n)
    Yf_even = Yf(k) + Yf_even;
end

if (odd > 0)&(k ~= (n+1))&(k>1)% Sorts out and adds up
                        % the Y coord with even indices
                        % excluding Y(1) and Y(n)
    Yf_odd = Yf(k) + Yf_odd;
end

% Calculations for toe pool B
Xg(k) = X_TRm - ((k-1)*m);
Yg(k) = ((Y_TRm/ X_TRm)*Xg(k)) - Y_Tp;

if (odd == 0)&(k ~= (n+1))&(k>1)% Sorts out and adds up
                        % the Y coord with odd indices
                        % excluding Y(1) and Y(n)
    Yg_even = Yg(k) + Yg_even;
end

if (odd > 0)&(k ~= (n+1))&(k>1)% Sorts out and adds up
                        % the Y coord with even indices
                        % excluding Y(1) and Y(n)
    Yg_odd = Yg(k) + Yg_odd;
end

% Calculations for toe pool C
Xh(k) = X_TRi - ((k-1)*p);
Yh(k) = sqrt((Ri^2)- (Xh(k)^2)) - Y_Tp;

if (odd == 0)&(k ~= (n+1))&(k>1)% Sorts out and adds up
                        % the Y coord with odd indices
                        % excluding Y(1) and Y(n)
    Yh_even = Yh(k) + Yh_even;
end

if (odd > 0)&(k ~= (n+1))&(k>1)% Sorts out and adds up
                        % the Y coord with even indices
                        % excluding Y(1) and Y(n)
    Yh_odd = Yh(k) + Yh_odd;
end

% Calculations for toe pool D
Xj(k) = 0 - ((k-1)*q);
Yj(k) = sqrt((Ri^2)- (Xj(k)^2)) - Y_Tp;
```

```
        if (odd == 0)&(k ~= (n+1))&(k>1)% Sorts out and adds up
                                        % the Y coord with odd indices
                                        % excluding Y(1) and Y(n)
            Yj_even = Yj(k) + Yj_even;
        end

        if (odd > 0)&(k ~= (n+1))&(k>1)% Sorts out and adds up
                                       % the Y coord with even indices
                                       % excluding Y(1) and Y(n)
            Yj_odd = Yj(k) + Yj_odd;
        end
    end

    % Calculation of the pool volume using Simpson rule
    Vf = l/3*Lm*((Yf(1)+Yf(n+1)) + (4*Yf_even) + (2*Yf_odd));
    Vg = m/3*Lm*((Yg(1)+Yg(n+1)) + (4*Yg_even) + (2*Yg_odd));
    Vh = p/3*Lm*((Yh(1)+Yh(n+1)) + (4*Yh_even) + (2*Yh_odd));
    Vj = q/3*Lm*((Yj(1)+Yj(n+1)) + (4*Yj_even) + (2*Yj_odd));

    end

    Vpool = Ve + Vf + Vg+ Vh + Vj;
  end

  V_simp = Vpool;
end

%%Calculation of the pools center of gravity
if Y_Tp < Y_TRi


  sum_MCx_r = 0;
  sum_MCx_s = 0;
  sum_MCx_t = 0;

  X_Tpi = sqrt((Ri^2)-(Y_Tp^2));

  for k = 1:(n+1)

    % create strips for different regions of the toe pool
    r = (X_Tp - X_TRm)/n;
    s = (X_TRm - X_Tpi)/n;
    t = ((X_Tpi - X_TRi)/n);

    % X & Y coordinates
    Xr(k) = X_Tp - ((k-1)*r);
    Yr(k) = sqrt((Rm^2)- (Xr(k)^2)) - Y_Tp;
```

```
        Xs(k) = X_TRm - ((k-1)*s);
        Ys(k) = (Y_TRm/X_TRm*Xs(k)) - Y_Tp;

        Xt(k) = X_Tpi - ((k-1)*t);
        Yt(k) = sqrt((Ri^2)-(Xt(k)^2)) - Y_Tp;
    end

    % Calculation of center of gravity for the strips

    for k = 1:n

        % Calculation of the centre of gravity for individual strips
        Cx_r(k) = (r*((2*Yr(k))+ (Yr(k+1)))/(3*(Yr(k)+Yr(k+1))))+ Xr(k+1);
        Cx_s(k) = (s*((2*Ys(k))+ (Ys(k+1)))/(3*(Ys(k)+Ys(k+1))))+ Xs(k+1);
        Cx_t(k) = (t*((2*Yt(k))+ (Yt(k+1)))/(3*(Yt(k)+Yt(k+1))))+ Xt(k+1);

        %Calculation of the mass of the individual elements
        Mr(k) = 0.5*r*Lm*rho_P*(Yr(k)+Yr(k+1));
        Ms(k) = 0.5*s*Lm*rho_P*(Ys(k)+Ys(k+1));
        Mt(k) = 0.5*t*Lm*rho_P*(Yt(k)+Yt(k+1));

        %Calculation of the product of Cx * M for individual strips
        sum_MCx_r = sum_MCx_r + (Mr(k)*Cx_r(k));
        sum_MCx_s = sum_MCx_s + (Ms(k)*Cx_s(k));
        sum_MCx_t = sum_MCx_t + (Mt(k)*Cx_t(k));
    end

    M_total = sum(Mr + Ms + Mt);% Total pool mass
    sum_MCx = sum_MCx_r + sum_MCx_s + sum_MCx_t; %Total sum of
the product of M * Cx
    Cx = (sum_MCx/M_total)
end

if Y_Tp >= Y_TRi


    sum_MCx_u = 0;
    sum_MCx_v = 0;

    X_Tpi = (X_TRm/Y_TRm)*Y_Tp;

    for k = 1:(n+1)

        % create strips for different regions of the toe pool
        u = (X_Tp - X_TRm)/n;
        v = (X_TRm - X_Tpi)/n;
```

```
        % X & Y coordinates
        Xu(k) = X_Tp - ((k-1)*u);
        Yu(k) = sqrt((Rm^2)- (Xu(k)^2)) - Y_Tp;

        Xv(k) = X_TRm - ((k-1)*v);
        Yv(k) = (Y_TRm/X_TRm*Xv(k)) - Y_Tp;
    end

    % Calculation of center of gravity for the strips
     for k = 1:n

        % Calculation of the centre of gravity for individual strips
        Cx_u(k) = (u*((2*Yu(k))+ (Yu(k+1)))/(3*(Yu(k)+Yu(k+1))))+ Xu(k+1);
        Cx_v(k) = (v*((2*Yv(k))+ (Yv(k+1)))/(3*(Yv(k)+Yv(k+1))))+ Xv(k+1);

        %Calculation of the mass of the individual elements
        Mu(k) = 0.5*u*Lm*rho_P*(Yu(k)+Yu(k+1));
        Mv(k) = 0.5*v*Lm*rho_P*(Yv(k)+Yv(k+1));

        %Calculation of the product of Cx * M for individual strips
        sum_MCx_u = sum_MCx_u + (Mu(k)*Cx_u(k));
        sum_MCx_v = sum_MCx_v + (Mv(k)*Cx_v(k));
    end

    M_total = sum(Mu + Mv);% Total pool mass
    sum_MCx = sum_MCx_u + sum_MCx_v; %Total sum of the product of
M * Cx
    Cx = (sum_MCx/M_total)
end

%% Pool Torque and Power calculation
Torq = M_total*9.81*Cx
Power = 2*pi*N_rpm*Torq/60
```

APPENDIX 3

TORQUE AREM MODEL

A3

A3.1 REGRESSION ON BALLS ONLY DATA

Table A3.1: Parameter estimation for balls only load

Parameters								
K	0.124							
β	0.836							
Δ_J	2.935							
N*	136.000							
Δ_N	1.018							
Experiment Data	**Experiment 1**				**Experiment 2**			
Mill Speed, N (%)	62.993	75.316	85.046	95.893	62.985	78.677	87.725	96.843
Mill Speed, rpm	37.006	44.246	49.962	56.334	37.002	46.221	51.536	56.893
Power, Watts	167.942	207.920	236.164	269.806	171.825	221.253	252.773	278.580
StdDev	0.920	1.323	1.901	2.560	1.523	1.279	2.115	3.352
Mill Filling, J (-)	0.200	0.200	0.200	0.200	0.200	0.200	0.200	0.200
Internal Mill Diameter, D (m)	0.526	0.526	0.526	0.526	0.526	0.526	0.526	0.526
Mill Length, L (m)	0.180	0.180	0.180	0.180	0.180	0.180	0.180	0.180
Model Data								
Ball Density, rb (Kg/m3)	7800.000	7800.000	7800.000	7800.000	7800.000	7800.000	7800.000	7800.000
Load Density, rl (kg/m3)	4680.000	4680.000	4680.000	4680.000	4680.000	4680.000	4680.000	4680.000
δ_c	0.000	0.000	0.000	0.000	0.000	0.000	0.000	0.000
Thickness of centrifuged layer, mm	0.000	0.000	0.000	0.000	0.000	0.000	0.000	0.000
Effective mill Diameter, Deff (m)	0.526	0.526	0.526	0.526	0.526	0.526	0.526	0.526
Effective mill filling, Jeff (-)	0.200	0.200	0.200	0.200	0.200	0.200	0.200	0.200
Effective Critical Mill Speed (RPM)	58.747	58.747	58.747	58.747	58.747	58.747	58.747	58.747
Effective mill speed, Neff (%)	62.993	75.316	85.046	95.893	62.985	78.677	87.725	96.843
Angle of repose, rads	0.785	0.785	0.785	0.785	0.785	0.785	0.785	0.785
Angle of repose, degrees	45.000	45.000	45.000	45.000	45.000	45.000	45.000	45.000
Model_Net Power (Watts)	176.779	211.362	238.670	269.109	176.757	220.795	246.187	271.775
Δ(Expt - Mod)	-8.837	-3.442	-2.506	0.697	-4.931	0.457	6.586	6.805
SSE	210.927							

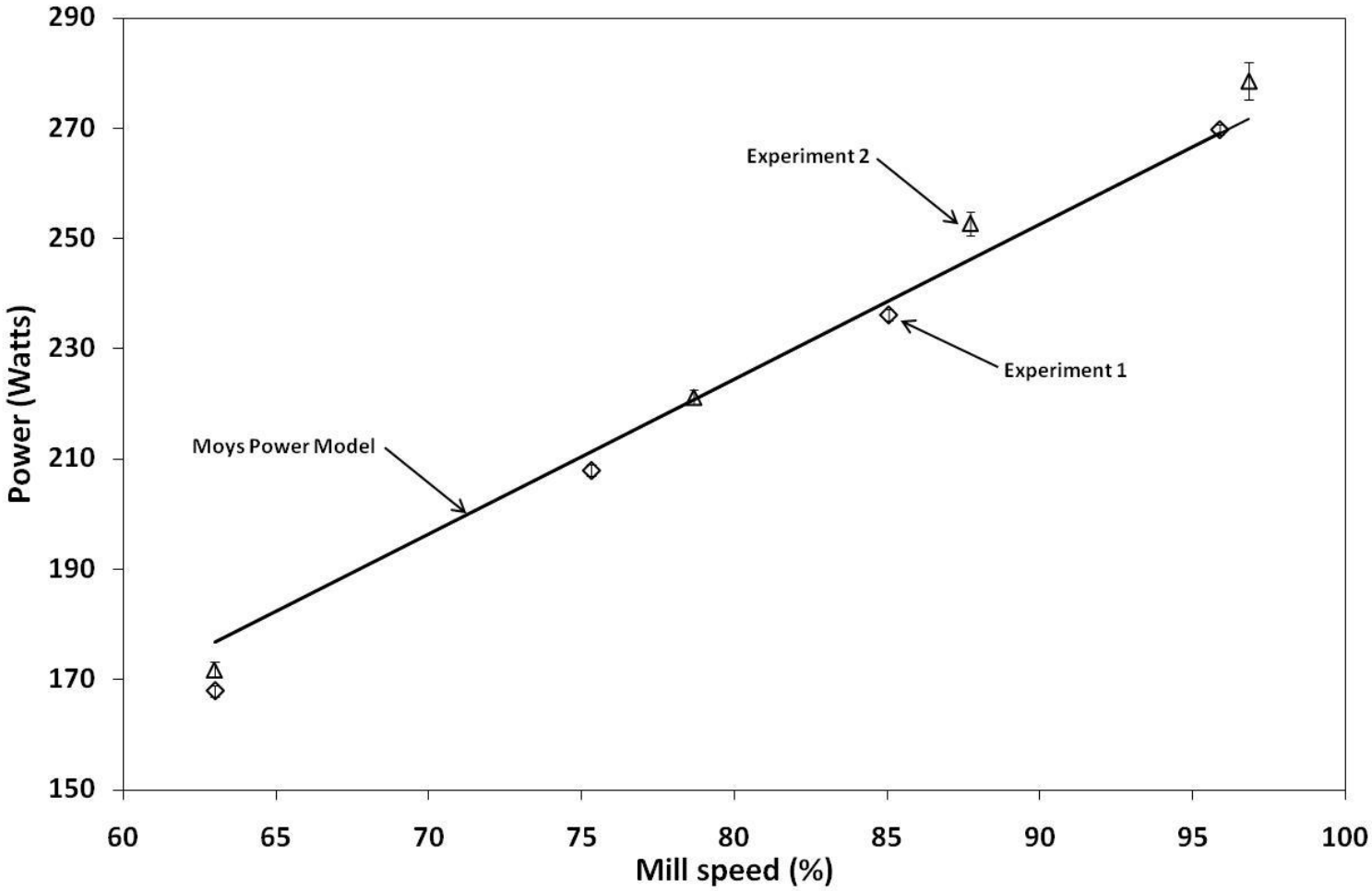


Figure A3.1: Model fit for balls only load

A3.2 REGRESSION ON POWER DATA FROM COARSE PARTICLE EXPERIMENTS

Table A3.2: Parameter estimation for coarse particles at the mill speed of 63% of the critical

Parameters										
K	0.124									
β	0.836									
Δ_J	2.935									
N*	136.000									
Δ_N	1.018									
Experiment Data										
Particle Filling, U (-)	0	20	40	60	70	80	90	100	110	150
Power_Expt (Watts)	167.942	173.925	184.655	187.747	191.792	200.997	200.292	203.689	209.045	213.534
StdDev	0.199	0.279	0.185	0.266	0.150	0.185	0.295	0.305	0.221	0.437
Mill Speed (%)	63.468	63.468	63.468	63.468	63.468	63.468	63.468	63.468	63.468	63.468
Mill Speed rpm	37.286	37.286	37.286	37.286	37.286	37.286	37.286	37.286	37.286	37.286
Ball filling (J)	0.200	0.200	0.200	0.200	0.200	0.200	0.200	0.200	0.208	0.240
Internal Mill Diameter, D (m)	0.526	0.526	0.526	0.526	0.526	0.526	0.526	0.526	0.526	0.526
Mill Length, L (m)	0.180	0.180	0.180	0.180	0.180	0.180	0.180	0.180	0.180	0.180
Ball Density (Kg/m3)	7800.000	7800.000	7800.000	7800.000	7800.000	7800.000	7800.000	7800.000	7800.000	7800.000
Particle Density (Kg/m3)	2466.667	2466.667	2466.667	2466.667	2466.667	2466.667	2466.667	2466.667	2466.667	2466.667
Load Density (kg/m3)	4680.000	4798.400	4916.800	5035.200	5094.400	5153.600	5212.800	5272.000	5126.154	4640.000
Model Data										
N*	136.000	136.000	136.000	136.000	136.000	136.000	136.000	136.000	136.000	136.000
N*f	136.000	136.000	136.000	136.000	136.000	136.000	136.000	136.000	136.000	136.000
Ucrit	2.500	2.500	2.500	2.500	2.500	2.500	2.500	2.500	2.500	2.500
N*p	136.000	136.000	136.000	136.000	136.000	136.000	136.000	136.000	136.000	136.000
dc	0.000	0.000	0.000	0.000	0.000	0.000	0.000	0.000	0.000	0.000
Thickness of centrifuged layer, mm	0.000	0.000	0.000	0.000	0.000	0.000	0.000	0.000	0.000	0.000
Deff	0.526	0.526	0.526	0.526	0.526	0.526	0.526	0.526	0.526	0.526
Jeff	0.200	0.200	0.200	0.200	0.200	0.200	0.200	0.200	0.208	0.240
Nceff , (rpm)	58.747	58.747	58.747	58.747	58.747	58.747	58.747	58.747	58.747	58.747
Neff , (%)	63.468	63.468	63.468	63.468	63.468	63.468	63.468	63.468	63.468	63.468
a	0.785	0.785	0.785	0.785	0.785	0.785	0.785	0.785	0.785	0.785
Power_Model (Watts)	178.378	182.891	187.404	191.917	194.173	196.430	198.686	200.943	201.566	203.698
Δ(Expt - Mod)	-10.436	-8.966	-2.749	-4.170	-2.381	4.567	1.606	2.746	7.479	9.836
SSE	403.589									

Table A3.3: Parameter estimation for coarse particles at the mill speed of 78% of the critical

Parameters										
K	0.126									
β	0.836									
Δ_J	2.935									
N*	136.000									
Δ_N	1.018									
Experiment Data										
Particle Filling, U (-)	0	20	40	60	70	80	90	100	110	150
Power_Expt (Watts)	207.920	224.045	231.809	237.486	238.439	252.005	251.649	255.973	244.451	219.352
StdDev	1.323	1.234	1.901	1.156	0.902	1.123	1.066	1.440	11.870	8.133
Mill Speed (%)	77.784	77.784	77.784	77.784	77.784	77.784	77.784	77.784	77.784	77.784
Mill Speed rpm	45.696	45.696	45.696	45.696	45.696	45.696	45.696	45.696	45.696	45.696
Ball filling (J)	0.200	0.200	0.200	0.200	0.200	0.200	0.200	0.200	0.208	0.240
Internal Mill Diameter, D (m)	0.526	0.526	0.526	0.526	0.526	0.526	0.526	0.526	0.526	0.526
Mill Length, L (m)	0.180	0.180	0.180	0.180	0.180	0.180	0.180	0.180	0.180	0.180
Ball Density (Kg/m3)	7800.000	7800.000	7800.000	7800.000	7800.000	7800.000	7800.000	7800.000	7800.000	7800.000
Particle Density (Kg/m3)	2466.667	2466.667	2466.667	2466.667	2466.667	2466.667	2466.667	2466.667	2466.667	2466.667
Load Density (kg/m3)	4680.000	4798.400	4916.800	5035.200	5094.400	5153.600	5212.800	5272.000	5126.154	4640.000
Model Data										
N*	136.000	136.000	136.000	136.000	136.000	136.000	136.000	136.000	136.000	78.324
N*f	78.324	78.324	78.324	78.324	78.324	78.324	78.324	78.324	78.324	78.324
Ucrit	1.300	1.300	1.300	1.300	1.300	1.300	1.300	1.300	1.300	1.300
N*p	136.000	136.000	136.000	136.000	136.000	136.000	136.000	136.000	136.000	78.324
dc	0.000	0.000	0.000	0.000	0.000	0.000	0.000	0.000	0.000	0.009
Thickness of centrifuged layer, mm	0.000	0.000	0.000	0.000	0.000	0.000	0.000	0.000	0.000	4.689
Deff	0.526	0.526	0.526	0.526	0.526	0.526	0.526	0.526	0.526	0.517
Jeff	0.200	0.200	0.200	0.200	0.200	0.200	0.200	0.200	0.208	0.212
Nceff , (rpm)	58.747	58.747	58.747	58.747	58.747	58.747	58.747	58.747	58.747	59.288
Neff , (%)	77.784	77.784	77.784	77.784	77.784	77.784	77.784	77.784	77.784	77.074
a	0.785	0.785	0.785	0.785	0.785	0.785	0.785	0.785	0.785	0.785
Power_Model (Watts)	220.993	226.584	232.175	237.766	240.561	243.357	246.152	248.948	249.720	218.271
Δ(Expt - Mod)	-13.073	-2.539	-0.366	-0.280	-2.122	8.648	5.497	7.026	-5.269	1.080
SSE	365.366									

Table A3.4: Power prediction with N* = 88 for coarse particles at the mill speed of 88% of the critical

Parameters										
K	0.125									
β	0.836									
Δ_J	2.935									
N*	136.000									
Δ_N	1.018									
Experiment Data										
Particle Filling, U (-)	0	20	40	60	70	80	90	100	110	150
Power_Expt (Watts)	236.164	258.624	264.437	275.737	269.589	253.047	243.850	230.850	215.696	238.643
StdDev	1.901	1.277	3.001	1.725	3.755	4.603	1.599	3.674	2.156	7.241
Mill Speed (%)	87.979	87.979	87.979	87.979	87.979	87.979	87.979	87.979	87.979	87.979
Mill Speed rpm	51.685	51.685	51.685	51.685	51.685	51.685	51.685	51.685	51.685	51.685
Ball filling (J)	0.200	0.200	0.200	0.200	0.200	0.200	0.200	0.200	0.208	0.240
Internal Mill Diameter, D (m)	0.526	0.526	0.526	0.526	0.526	0.526	0.526	0.526	0.526	0.526
Mill Length, L (m)	0.180	0.180	0.180	0.180	0.180	0.180	0.180	0.180	0.180	0.180
Ball Density (Kg/m3)	7800.000	7800.000	7800.000	7800.000	7800.000	7800.000	7800.000	7800.000	7800.000	7800.000
Particle Density (Kg/m3)	2466.667	2466.667	2466.667	2466.667	2466.667	2466.667	2466.667	2466.667	2466.667	2466.667
Load Density (kg/m3)	4680.000	4798.400	4916.800	5035.200	5094.400	5153.600	5212.800	5272.000	5126.154	4640.000
Model Data										
N*	136.000	136.000	136.000	136.000	136.000	88.000	88.000	88.000	88.000	88.000
N*f	97.892	94.731	92.149	90.147	89.363	88.724	88.230	87.880	87.676	88.306
Ucrit	0.750	0.750	0.750	0.750	0.750	0.750	0.750	0.750	0.750	0.750
N*p	136.000	136.000	136.000	136.000	136.000	88.000	88.000	88.000	88.000	88.000
$\delta\chi$	0.000	0.000	0.000	0.000	0.000	0.009	0.009	0.009	0.010	0.015
Thickness of centrifuged layer, mm	0.000	0.000	0.000	0.000	0.000	4.573	4.573	4.573	5.131	7.809
Deff	0.526	0.526	0.526	0.526	0.526	0.517	0.517	0.517	0.516	0.510
Jeff	0.200	0.200	0.200	0.200	0.200	0.171	0.171	0.171	0.176	0.193
Nceff , (rpm)	58.747	58.747	58.747	58.747	58.747	59.275	59.275	59.275	59.340	59.657
Neff , (%)	87.979	87.979	87.979	87.979	87.979	87.196	87.196	87.196	87.100	86.637
α	0.785	0.785	0.785	0.785	0.785	0.785	0.785	0.785	0.785	0.785
Power_Model (Watts)	249.382	255.691	262.000	268.309	271.464	230.507	233.155	235.803	233.100	220.552
Δ(Expt - Mod)	-13.218	2.933	2.436	7.428	-1.875	22.539	10.695	-4.953	-17.404	18.091
SSE	1197.757									

Table A3.5: N* linear model parameter estimation for coarse particles at the mill speed of 88% of the critical

Parameters									
K	0.125								
β	0.836								
Δ_J	2.935								
N*	136.000								
Δ_N	1.018								
N* Linear model parameters									
a1	-3.127								
b1	91.103								
Experiment Data									
Particle Filling, U (-)	0	20	40	60	70	80	90	100	110
Power_Expt (Watts)	236.164	258.624	264.437	275.737	269.589	253.047	243.850	230.850	215.696
StdDev	1.901	1.277	3.001	1.725	3.755	4.603	1.599	3.674	2.156
Mill Speed (%)	87.979	87.979	87.979	87.979	87.979	87.979	87.979	87.979	87.979
Mill Speed rpm	51.685	51.685	51.685	51.685	51.685	51.685	51.685	51.685	51.685
Ball filling (J)	0.200	0.200	0.200	0.200	0.200	0.200	0.200	0.200	0.208
Internal Mill Diameter, D (m)	0.526	0.526	0.526	0.526	0.526	0.526	0.526	0.526	0.526
Mill Length, L (m)	0.180	0.180	0.180	0.180	0.180	0.180	0.180	0.180	0.180
Ball Density (Kg/m3)	7800.000	7800.000	7800.000	7800.000	7800.000	7800.000	7800.000	7800.000	7800.000
Particle Density (Kg/m3)	2466.667	2466.667	2466.667	2466.667	2466.667	2466.667	2466.667	2466.667	2466.667
Load Density (kg/m3)	4680.000	4798.400	4916.800	5035.200	5094.400	5153.600	5212.800	5272.000	5126.154
Model Data									
N*	136.000	136.000	136.000	136.000	136.000	88.601	88.289	87.976	87.663
N*f	97.892	94.731	92.149	90.147	89.363	88.724	88.230	87.880	87.676
Ucrit	0.750	0.750	0.750	0.750	0.750	0.750	0.750	0.750	0.750
N*p	136.000	136.000	136.000	136.000	136.000	88.601	88.289	87.976	87.663
δ_c	0.000	0.000	0.000	0.000	0.000	0.005	0.007	0.009	0.014
Thickness of centrifuged layer, mm	0.000	0.000	0.000	0.000	0.000	2.532	3.443	4.682	7.142
Deff	0.526	0.526	0.526	0.526	0.526	0.521	0.519	0.517	0.512
Jeff	0.200	0.200	0.200	0.200	0.200	0.184	0.179	0.171	0.163
Nceff , (rpm)	58.747	58.747	58.747	58.747	58.747	59.038	59.143	59.288	59.578
Neff , (%)	87.979	87.979	87.979	87.979	87.979	87.546	87.390	87.177	86.752
α (Radians)	0.785	0.785	0.785	0.785	0.785	0.785	0.785	0.785	0.785
Power_Model (Watts)	249.382	255.691	262.000	268.309	271.464	250.233	244.210	234.726	213.892
Δ(Expt - Mod)	-13.218	2.933	2.436	7.428	-1.875	2.814	-0.360	-3.877	1.804
SSE	274.266								

Table A3.6: N* linear model parameter estimation for coarse particles at the mill speed of 88% of the critical

Parameters										
K	0.125									
β	0.836									
Δ_J	2.935									
N*	136.000									
Δ_N	1.018									
N* Linear model parameters										
a1	-3.127									
b1	91.103									
N* Linear model parameters										
a2	1.598									
b2	85.910									
Experiment Data										
Particle Filling, U (-)	0	20	40	60	70	80	90	100	110	150
Power_Expt (Watts)	236.164	258.624	264.437	275.737	269.589	253.047	243.850	230.850	215.696	238.643
StdDev	1.901	1.277	3.001	1.725	3.755	4.603	1.599	3.674	2.156	7.241
Mill Speed (%)	87.979	87.979	87.979	87.979	87.979	87.979	87.979	87.979	87.979	87.979
Mill Speed rpm	51.685	51.685	51.685	51.685	51.685	51.685	51.685	51.685	51.685	51.685
Ball filling (J)	0.200	0.200	0.200	0.200	0.200	0.200	0.200	0.200	0.208	0.240
Internal Mill Diameter, D (m)	0.526	0.526	0.526	0.526	0.526	0.526	0.526	0.526	0.526	0.526
Mill Length, L (m)	0.180	0.180	0.180	0.180	0.180	0.180	0.180	0.180	0.180	0.180
Ball Density (Kg/m3)	7800.000	7800.000	7800.000	7800.000	7800.000	7800.000	7800.000	7800.000	7800.000	7800.000
Particle Density (Kg/m3)	2466.667	2466.667	2466.667	2466.667	2466.667	2466.667	2466.667	2466.667	2466.667	2466.667
Load Density (kg/m3)	4680.000	4798.400	4916.800	5035.200	5094.400	5153.600	5212.800	5272.000	5126.154	4640.000
Model Data										
N*	136.000	136.000	136.000	136.000	136.000	88.601	88.289	87.976	87.663	88.307
N*f	97.892	94.731	92.149	90.147	89.363	88.724	88.230	87.880	87.676	88.306
Ucrit	0.750	0.750	0.750	0.750	0.750	0.750	0.750	0.750	0.750	0.750
N*p	136.000	136.000	136.000	136.000	136.000	88.601	88.289	87.976	87.663	88.307
dc	0.000	0.000	0.000	0.000	0.000	0.005	0.007	0.009	0.014	0.011
Thickness of centrifuged layer, mm	0.000	0.000	0.000	0.000	0.000	2.532	3.443	4.682	7.142	5.778
Deff	0.526	0.526	0.526	0.526	0.526	0.521	0.519	0.517	0.512	0.514
Jeff	0.200	0.200	0.200	0.200	0.200	0.184	0.179	0.171	0.163	0.205
Nceff , (rpm)	58.747	58.747	58.747	58.747	58.747	59.038	59.143	59.288	59.578	59.416
Neff , (%)	87.979	87.979	87.979	87.979	87.979	87.546	87.390	87.177	86.752	86.988
a	0.785	0.785	0.785	0.785	0.785	0.785	0.785	0.785	0.785	0.785
Power_Model (Watts)	249.382	255.691	262.000	268.309	271.464	250.233	244.210	234.726	213.892	237.330
Δ(Expt - Mod)	-13.218	2.933	2.436	7.428	-1.875	2.814	-0.360	-3.877	1.804	1.312
SSE	274.266									

Table A3.7: Power prediction with N* = 98 for coarse particles at the mill speed of 98% of the critical

Parameters										
K	0.126									
β	0.937									
Δ_J	2.935									
N*	136.000									
Δ_N	1.018									
Experiment Data										
Particle Filling, U (-)	0	20	40	60	70	80	90	100	110	150
Power_Expt (Watts)	269.806	290.506	289.874	288.930	264.318	251.065	237.848	226.363	233.843	235.896
StdDev	2.560	2.184	1.654	2.543	9.285	5.648	5.332	11.246	5.001	4.975
Mill Speed (%)	98.300	98.300	98.300	98.300	98.300	98.300	98.300	98.300	98.300	98.300
Mill Speed rpm	57.749	57.749	57.749	57.749	57.749	57.749	57.749	57.749	57.749	57.749
Ball filling (J)	0.200	0.200	0.200	0.200	0.200	0.200	0.200	0.200	0.208	0.240
Internal Mill Diameter, D (m)	0.526	0.526	0.526	0.526	0.526	0.526	0.526	0.526	0.526	0.526
Mill Length, L (m)	0.180	0.180	0.180	0.180	0.180	0.180	0.180	0.180	0.180	0.180
Ball Density (Kg/m3)	7800.000	7800.000	7800.000	7800.000	7800.000	7800.000	7800.000	7800.000	7800.000	7800.000
Particle Density (Kg/m3)	2466.667	2466.667	2466.667	2466.667	2466.667	2466.667	2466.667	2466.667	2466.667	2466.667
Load Density (kg/m3)	4680.000	4798.400	4916.800	5035.200	5094.400	5153.600	5212.800	5272.000	5126.154	4640.000
Model Data										
N*	136.000	136.000	136.000	136.000	98.000	98.000	98.000	98.000	98.000	98.000
N*f	102.860	101.257	99.957	98.959	98.574	98.264	98.030	97.872	97.789	98.215
Ucrit	0.650	0.650	0.650	0.650	0.650	0.650	0.650	0.650	0.650	0.650
N*p	136.000	136.000	136.000	135.775	98.000	98.000	98.000	98.000	98.000	98.000
dc	0.000	0.000	0.000	0.000	0.012	0.012	0.012	0.012	0.013	0.020
Thickness of centrifuged layer, mm	0.000	0.000	0.000	0.000	6.271	6.271	6.271	6.271	7.036	10.709
Deff	0.526	0.526	0.526	0.526	0.513	0.513	0.513	0.513	0.512	0.505
Jeff	0.200	0.200	0.200	0.200	0.160	0.160	0.160	0.160	0.164	0.174
Nceff , (rpm)	58.747	58.747	58.747	58.747	59.474	59.474	59.474	59.474	59.565	60.006
Neff , (%)	98.300	98.300	98.300	98.300	97.098	97.098	97.098	97.098	96.950	96.238
a	0.785	0.785	0.785	0.785	0.785	0.785	0.785	0.785	0.785	0.785
Power_Model (Watts)	273.381	280.297	287.214	294.130	233.252	235.962	238.673	241.383	236.809	216.213
Δ(Expt - Mod)	-3.575	10.209	2.660	-5.200	31.066	15.103	-0.825	-15.020	-2.966	19.683
SSE	1966.854									

Table A3.8: N* linear model parameter estimation for coarse particles at the mill speed of 98% of the critical

Parameters										
K	0.126									
β	0.937									
Δ_J	2.935									
N*	136.000									
Δ_N	1.018									
N* Linear model parameters										
a1	-0.059									
b1	98.186									
Experiment Data										
Particle Filling, U (-)	0	20	40	60	70	80	90	100	110	150
Power_Expt (Watts)	269.806	290.506	289.874	288.930	264.318	251.065	237.848	226.363	233.843	235.896
StdDev	2.560	2.184	1.654	2.543	9.285	5.648	5.332	11.246	5.001	4.975
Mill Speed (%)	98.300	98.300	98.300	98.300	98.300	98.300	98.300	98.300	98.300	98.300
Mill Speed rpm	57.749	57.749	57.749	57.749	57.749	57.749	57.749	57.749	57.749	57.749
Ball filling (J)	0.200	0.200	0.200	0.200	0.200	0.200	0.200	0.200	0.208	0.240
Internal Mill Diameter, D (m)	0.526	0.526	0.526	0.526	0.526	0.526	0.526	0.526	0.526	0.526
Mill Length, L (m)	0.180	0.180	0.180	0.180	0.180	0.180	0.180	0.180	0.180	0.180
Ball Density (Kg/m3)	7800.000	7800.000	7800.000	7800.000	7800.000	7800.000	7800.000	7800.000	7800.000	7800.000
Particle Density (Kg/m3)	2466.667	2466.667	2466.667	2466.667	2466.667	2466.667	2466.667	2466.667	2466.667	2466.667
Load Density (kg/m3)	4680.000	4798.400	4916.800	5035.200	5094.400	5153.600	5212.800	5272.000	5126.154	4640.000
Model Data										
N*	136.000	136.000	136.000	135.775	98.145	98.139	98.133	98.127	98.121	98.098
N*f	102.860	101.257	99.957	98.959	98.574	98.264	98.030	97.872	97.789	98.215
Ucrit	0.650	0.650	0.650	0.650	0.650	0.650	0.650	0.650	0.650	0.650
N*p	136.000	136.000	136.000	135.775	98.145	98.139	98.133	98.127	98.121	98.098
dc	0.000	0.000	0.000	0.000	0.010	0.010	0.010	0.011	0.012	0.018
Thickness of centrifuged layer, mm	0.000	0.000	0.000	0.000	5.440	5.471	5.503	5.535	6.246	9.729
Deff	0.526	0.526	0.526	0.526	0.515	0.515	0.515	0.515	0.514	0.507
Jeff	0.200	0.200	0.200	0.200	0.166	0.166	0.165	0.165	0.169	0.180
Nceff , (rpm)	58.747	58.747	58.747	58.747	59.377	59.380	59.384	59.388	59.472	59.887
Neff , (%)	98.300	98.300	98.300	98.300	97.258	97.252	97.246	97.240	97.103	96.429
a	0.785	0.785	0.785	0.785	0.785	0.785	0.785	0.785	0.785	0.785
Power_Model (Watts)	273.381	280.297	287.214	294.130	241.867	244.347	246.818	249.279	244.956	224.970
Δ(Expt - Mod)	-3.575	10.209	2.660	-5.200	22.451	6.718	-8.970	-22.916	-11.113	10.926
SSE	1548.808									

Table A3.9: N* linear model parameter estimation for coarse particles at the mill speed of 98% of the critical

Parameters										
K	0.126									
β	0.937									
Δ_J	2.935									
N*	136.000									
Δ_N	1.018									
N* Linear model parameters - Cataracting										
a1	-2.597									
b1	100.359									
N* Linear model parameters - Centrifuging										
a2	0.690									
b2	97.189									
Experiment Data										
Particle Filling, U (-)	0	20	40	60	70	80	90	100	110	150
Power_Expt (Watts)	269.806	290.506	289.874	288.930	264.318	251.065	237.848	226.363	233.843	235.896
StdDev	2.560	2.184	1.654	2.543	9.285	5.648	5.332	11.246	5.001	4.975
Mill Speed (%)	98.300	98.300	98.300	98.300	98.300	98.300	98.300	98.300	98.300	98.300
Mill Speed rpm	57.749	57.749	57.749	57.749	57.749	57.749	57.749	57.749	57.749	57.749
Ball filling (J)	0.200	0.200	0.200	0.200	0.200	0.200	0.200	0.200	0.208	0.240
Internal Mill Diameter, D (m)	0.526	0.526	0.526	0.526	0.526	0.526	0.526	0.526	0.526	0.526
Mill Length, L (m)	0.180	0.180	0.180	0.180	0.180	0.180	0.180	0.180	0.180	0.180
Ball Density (Kg/m3)	7800.000	7800.000	7800.000	7800.000	7800.000	7800.000	7800.000	7800.000	7800.000	7800.000
Particle Density (Kg/m3)	2466.667	2466.667	2466.667	2466.667	2466.667	2466.667	2466.667	2466.667	2466.667	2466.667
Load Density (kg/m3)	4680.000	4798.400	4916.800	5035.200	5094.400	5153.600	5212.800	5272.000	5126.154	4640.000
Model Data										
N*	136.000	136.000	136.000	135.775	98.541	98.282	98.022	97.762	97.947	98.223
N*f	102.860	101.257	99.957	98.959	98.574	98.264	98.030	97.872	97.789	98.215
Ucrit	0.650	0.650	0.650	0.650	0.650	0.650	0.650	0.650	0.650	0.650
N*p	136.000	136.000	136.000	135.775	98.541	98.282	98.022	97.762	97.947	98.223
dc	0.000	0.000	0.000	0.000	0.007	0.009	0.012	0.015	0.014	0.016
Thickness of centrifuged layer, mm	0.000	0.000	0.000	0.000	3.685	4.756	6.138	7.922	7.411	8.601
Deff	0.526	0.526	0.526	0.526	0.519	0.516	0.514	0.510	0.511	0.509
Jeff	0.200	0.200	0.200	0.200	0.177	0.170	0.161	0.150	0.161	0.188
Nceff , (rpm)	58.747	58.747	58.747	58.747	59.171	59.296	59.459	59.670	59.610	59.752
Neff , (%)	98.300	98.300	98.300	98.300	97.596	97.390	97.124	96.779	96.878	96.648
a	0.785	0.785	0.785	0.785	0.785	0.785	0.785	0.785	0.785	0.785
Power_Model (Watts)	274.425	281.368	288.310	295.253	260.957	252.788	241.002	224.448	233.826	235.908
Δ(Expt - Mod)	-4.619	9.139	1.563	-6.323	3.361	-1.723	-3.154	1.915	0.017	-0.012
SSE	175.150									

A3.3 REGRESSION ON POWER DATA FROM FINE PARTICLE EXPERIMENTS

Table A3.10: Power prediction with N* = 64 for fine particles at the mill speed of 63% of the critical

Parameters											
K	0.098										
β	0.836										
Δ_J	2.935										
N*	136.000										
Δ_N	1.018										
Experiment Data											
Particle Filling, U (-)	0	20	40	60	70	80	90	100	110	120	160
Power_Expt (Watts)	167.942	181.698	181.433	184.189	189.021	183.122	185.710	177.801	176.412	175.613	178.132
StdDev	0.920	1.065	2.200	1.202	3.081	1.886	1.086	1.525	2.211	1.426	1.714
Mill Speed (%)	63.335	63.335	63.335	63.335	63.335	63.335	63.335	63.335	63.335	63.335	63.335
Mill Speed rpm	37.207	37.207	37.207	37.207	37.207	37.207	37.207	37.207	37.207	37.207	37.207
Ball filling (J)	0.200	0.200	0.200	0.200	0.200	0.200	0.200	0.200	0.208	0.240	0.240
Internal Mill Diameter, D (m)	0.526	0.526	0.526	0.526	0.526	0.526	0.526	0.526	0.526	0.526	0.526
Mill Length, L (m)	0.180	0.180	0.180	0.180	0.180	0.180	0.180	0.180	0.180	0.180	0.180
Ball Density (Kg/m3)	7800.000	7800.000	7800.000	7800.000	7800.000	7800.000	7800.000	7800.000	7800.000	7800.000	7800.000
Particle Density (Kg/m3)	2466.667	2466.667	2466.667	2466.667	2466.667	2466.667	2466.667	2466.667	2466.667	2466.667	2466.667
Load Density (kg/m3)	4680.000	4798.400	4916.800	5035.200	5094.400	5153.600	5212.800	5272.000	5126.154	4991.111	4538.065
Model Data											
N*	136.000	136.000	136.000	136.000	136.000	136.000	136.000	64.000	64.000	64.000	64.000
dc	0.000	0.000	0.000	0.000	0.000	0.000	0.000	0.005	0.005	0.008	0.008
Thickness of centrifuged layer, mm	0.000	0.000	0.000	0.000	0.000	0.000	0.000	2.429	2.725	4.147	4.147
Deff	0.526	0.526	0.526	0.526	0.526	0.526	0.526	0.521	0.521	0.518	0.518
Jeff	0.200	0.200	0.200	0.200	0.200	0.200	0.200	0.185	0.191	0.216	0.248
Nceff , (rpm)	58.747	58.747	58.747	58.747	58.747	58.747	58.747	59.026	59.060	59.225	59.225
Neff , (%)	63.335	63.335	63.335	63.335	63.335	63.335	63.335	63.036	62.999	62.824	62.824
a	0.785	0.785	0.785	0.785	0.785	0.785	0.785	0.785	0.785	0.785	0.785
Power_Model (Watts)	170.711	175.030	179.349	183.667	185.827	187.986	190.146	176.421	175.782	185.898	187.725
Δ(Expt - Mod)	-2.769	6.668	2.085	0.521	3.194	-4.864	-4.435	1.380	0.630	-10.285	-9.593
SSE	310.381										

Table A3.11: N* linear model parameter estimation for fine particles at the mill speed of 63% of the critical

Parameters											
K	0.098										
β	0.836										
Δ_J	2.935										
N*	136.000										
Δ_N	1.018										
N* Linear model parameters											
a	-1.583										
b	65.630										
Experiment Data											
Particle Filling, U (-)	0	20	40	60	70	80	90	100	110	120	160
Power_Expt (Watts)	167.942	181.698	181.433	184.189	189.021	183.122	185.710	177.801	176.412	175.613	178.132
StdDev	0.920	1.065	2.200	1.202	3.081	1.886	1.086	1.525	2.211	1.426	1.714
Mill Speed (%)	63.335	63.335	63.335	63.335	63.335	63.335	63.335	63.335	63.335	63.335	63.335
Mill Speed rpm	37.207	37.207	37.207	37.207	37.207	37.207	37.207	37.207	37.207	37.207	37.207
Ball filling (J)	0.200	0.200	0.200	0.200	0.200	0.200	0.200	0.200	0.208	0.240	0.240
Internal Mill Diameter, D (m)	0.526	0.526	0.526	0.526	0.526	0.526	0.526	0.526	0.526	0.526	0.526
Mill Length, L (m)	0.180	0.180	0.180	0.180	0.180	0.180	0.180	0.180	0.180	0.180	0.180
Ball Density (Kg/m3)	7800.000	7800.000	7800.000	7800.000	7800.000	7800.000	7800.000	7800.000	7800.000	7800.000	7800.000
Particle Density (Kg/m3)	2466.667	2466.667	2466.667	2466.667	2466.667	2466.667	2466.667	2466.667	2466.667	2466.667	2466.667
Load Density (kg/m3)	4680.000	4798.400	4916.800	5035.200	5094.400	5153.600	5212.800	5272.000	5126.154	4991.111	4538.065
Model Data											
N*	136.000	136.000	136.000	136.000	136.000	136.000	136.000	64.047	63.889	63.731	63.098
$\delta\chi$	0.000	0.000	0.000	0.000	0.000	0.000	0.000	0.004	0.006	0.010	0.019
Thickness of centrifuged layer, mm	0.000	0.000	0.000	0.000	0.000	0.000	0.000	2.318	3.038	5.402	10.063
Deff	0.526	0.526	0.526	0.526	0.526	0.526	0.526	0.521	0.520	0.515	0.506
Jeff	0.200	0.200	0.200	0.200	0.200	0.200	0.200	0.186	0.189	0.216	0.248
Nceff , (rpm)	58.747	58.747	58.747	58.747	58.747	58.747	58.747	59.013	59.096	59.372	59.928
Neff , (%)	63.335	63.335	63.335	63.335	63.335	63.335	63.335	63.049	62.961	62.668	62.087
α	0.785	0.785	0.785	0.785	0.785	0.785	0.785	0.785	0.785	0.785	0.785
Power_Model (Watts)	170.711	175.030	179.349	183.667	185.827	187.986	190.146	177.148	173.801	183.644	177.142
Δ(Expt - Mod)	-2.769	6.668	2.085	0.521	3.194	-4.864	-4.435	0.653	2.611	-8.031	0.990
SSE	183.000										

Table A3.12: Power prediction with N* = 78.98 for fine particles at the mill speed of 78% of the critical

Parameters										
K	0.101									
β	0.836									
Δ_J	2.935									
N*	136.000									
Δ_N	1.018									
Experiment Data										
Particle Filling, U (-)	0	20	40	60	70	80	90	100	110	160
Power_Expt (Watts)	207.920	224.555	233.800	240.151	238.960	232.540	241.144	236.123	226.994	229.293
StdDev	1.323	1.152	1.061	1.491	1.094	1.477	1.578	1.193	1.270	1.508
Mill Speed (%)	78.064	78.064	78.064	78.064	78.064	78.064	78.064	78.064	78.064	78.064
Mill Speed rpm	45.860	45.860	45.860	45.860	45.860	45.860	45.860	45.860	45.860	45.860
Ball filling (J)	0.200	0.200	0.200	0.200	0.200	0.200	0.200	0.200	0.208	0.240
Internal Mill Diameter, D (m)	0.526	0.526	0.526	0.526	0.526	0.526	0.526	0.526	0.526	0.526
Mill Length, L (m)	0.180	0.180	0.180	0.180	0.180	0.180	0.180	0.180	0.180	0.180
Ball Density (Kg/m3)	7800.000	7800.000	7800.000	7800.000	7800.000	7800.000	7800.000	7800.000	7800.000	7800.000
Particle Density (Kg/m3)	2466.667	2466.667	2466.667	2466.667	2466.667	2466.667	2466.667	2466.667	2466.667	2466.667
Load Density (kg/m3)	4680.000	4798.400	4916.800	5035.200	5094.400	5153.600	5212.800	5272.000	5126.154	4538.065
Model Data										
N*	136.000	136.000	136.000	136.000	136.000	136.000	136.000	78.983	78.983	78.983
dc	0.000	0.000	0.000	0.000	0.000	0.000	0.000	0.004	0.004	0.006
Thickness of centrifuged layer, mm	0.000	0.000	0.000	0.000	0.000	0.000	0.000	1.893	2.124	3.232
Deff	0.526	0.526	0.526	0.526	0.526	0.526	0.526	0.522	0.522	0.520
Jeff	0.200	0.200	0.200	0.200	0.200	0.200	0.200	0.188	0.195	0.248
Nceff , (rpm)	58.747	58.747	58.747	58.747	58.747	58.747	58.747	58.964	58.991	59.119
Neff , (%)	78.064	78.064	78.064	78.064	78.064	78.064	78.064	77.777	77.742	77.573
α	0.785	0.785	0.785	0.785	0.785	0.785	0.785	0.785	0.785	0.785
Power_Model (Watts)	217.206	222.701	228.196	233.691	236.439	239.186	241.934	228.948	228.485	240.979
Δ(Expt - Mod)	-9.286	1.854	5.604	6.460	2.522	-6.646	-0.790	7.175	-1.490	-11.686
SSE	404.221									

Table A3.13: N* linear model parameter estimation for fine particles at the mill speed of 78% of the critical

Parameters										
K	0.101372									
β	0.836413									
Δ_J	2.935335									
N*	136									
Δ_N	1.017754									
N* Linear model parameters										
a	-2.13729									
b	81.4188									
Experiment Data										
Particle Filling, U (-)	0	20	40	60	70	80	90	100	110	160
Power_Expt (Watts)	207.92	224.5554	233.8003	240.151	238.9604	232.5403	241.1444	236.1229	226.9944	229.2931
StdDev	1.323088	1.15194	1.0609	1.491424	1.094196	1.477159	1.577637	1.192754	1.269668	1.508451
Mill Speed (%)	78.06385	78.06385	78.06385	78.06385	78.06385	78.06385	78.06385	78.06385	78.06385	78.06385
Mill Speed rpm	45.86037	45.86037	45.86037	45.86037	45.86037	45.86037	45.86037	45.86037	45.86037	45.86037
Ball filling (J)	0.2	0.2	0.2	0.2	0.2	0.2	0.2	0.2	0.208	0.24
Internal Mill Diameter, D (m)	0.526	0.526	0.526	0.526	0.526	0.526	0.526	0.526	0.526	0.526
Mill Length, L (m)	0.18	0.18	0.18	0.18	0.18	0.18	0.18	0.18	0.18	0.18
Ball Density (Kg/m3)	7800	7800	7800	7800	7800	7800	7800	7800	7800	7800
Particle Density (Kg/m3)	2466.667	2466.667	2466.667	2466.667	2466.667	2466.667	2466.667	2466.667	2466.667	2466.667
Load Density (kg/m3)	4680	4798.4	4916.8	5035.2	5094.4	5153.6	5212.8	5272	5126.154	4538.065
Model Data										
N*	136	136	136	136	136	136	136	79.28151	79.06778	77.99913
dc	1.68E-27	1.68E-27	1.68E-27	1.68E-27	1.68E-27	1.68E-27	1.68E-27	0.002683	0.003714	0.016156
Thickness of centrifuged layer, mm	8.85E-25	8.85E-25	8.85E-25	8.85E-25	8.85E-25	8.85E-25	8.85E-25	1.411485	1.953787	8.497939
Deff	0.526	0.526	0.526	0.526	0.526	0.526	0.526	0.523177	0.522092	0.509004
Jeff	0.2	0.2	0.2	0.2	0.2	0.2	0.2	0.191343	0.1961	0.248
Nceff , (rpm)	58.74726	58.74726	58.74726	58.74726	58.74726	58.74726	58.74726	58.90862	58.97097	59.73934
Neff , (%)	78.06385	78.06385	78.06385	78.06385	78.06385	78.06385	78.06385	77.85002	77.76771	76.76746
a	0.785398	0.785398	0.785398	0.785398	0.785398	0.785398	0.785398	0.785398	0.785398	0.785398
Power_Model (Watts)	217.2058	222.701	228.1961	233.6912	236.4388	239.1863	241.9339	232.9587	229.8455	228.9054
Δ(Expt - Mod)	-9.28588	1.85438	5.604171	6.459741	2.521644	-6.64607	-0.78951	3.164181	-2.85104	0.387671
SSE	232.2444									

Table A3.14: Power prediction with N* = 89.2 for fine particles at the mill speed of 88% of the critical

Parameters											
K	0.103										
β	0.836										
Δ_J	2.935										
N*	136.000										
Δ_N	1.018										
Experiment Data											
Particle Filling, U (-)	0	20	40	60	70	80	90	100	110	120	160
Power_Expt (Watts)	236.164	262.164	273.872	270.353	270.558	274.481	278.230	271.934	265.691	266.807	255.828
StdDev	1.901	1.855	3.315	4.083	2.660	1.835	2.833	3.738	2.261	2.534	3.524
Mill Speed (%)	88.144	88.144	88.144	88.144	88.144	88.144	88.144	88.144	88.144	88.144	88.144
Mill Speed rpm	51.782	51.782	51.782	51.782	51.782	51.782	51.782	51.782	51.782	51.782	51.782
Ball filling (J)	0.200	0.200	0.200	0.200	0.200	0.200	0.200	0.200	0.208	0.218	0.240
Internal Mill Diameter, D (m)	0.526	0.526	0.526	0.526	0.526	0.526	0.526	0.526	0.526	0.526	0.526
Mill Length, L (m)	0.180	0.180	0.180	0.180	0.180	0.180	0.180	0.180	0.180	0.180	0.180
Ball Density (Kg/m3)	7800.000	7800.000	7800.000	7800.000	7800.000	7800.000	7800.000	7800.000	7800.000	7800.000	7800.000
Particle Density (Kg/m3)	2466.667	2466.667	2466.667	2466.667	2466.667	2466.667	2466.667	2466.667	2466.667	2466.667	2466.667
Load Density (kg/m3)	4680.000	4798.400	4916.800	5035.200	5094.400	5153.600	5212.800	5272.000	5126.154	4991.111	4538.065
Model Data											
N*	136.000	136.000	136.000	136.000	136.000	136.000	136.000	89.166	89.166	89.166	89.166
δ_c	0.000	0.000	0.000	0.000	0.000	0.000	0.000	0.003	0.004	0.004	0.006
Thickness of centrifuged layer, mm	0.000	0.000	0.000	0.000	0.000	0.000	0.000	1.711	1.920	2.203	2.922
Deff	0.526	0.526	0.526	0.526	0.526	0.526	0.526	0.523	0.522	0.522	0.520
Jeff	0.200	0.200	0.200	0.200	0.200	0.200	0.200	0.189	0.196	0.205	0.240
Nceff , (rpm)	58.747	58.747	58.747	58.747	58.747	58.747	58.747	58.943	58.967	59.000	59.083
Neff , (%)	88.144	88.144	88.144	88.144	88.144	88.144	88.144	87.851	87.815	87.767	87.643
α (Radians)	0.785	0.785	0.785	0.785	0.785	0.785	0.785	0.785	0.785	0.785	0.785
Power_Model (Watts)	250.321	256.653	262.986	269.319	272.486	275.652	278.819	265.601	265.203	266.296	271.843
Δ(Expt - Mod)	-14.156	5.511	10.886	1.034	-1.927	-1.171	-0.589	6.334	0.488	0.511	-16.015
SSE	652.869										

Table A3.15: N* linear model parameter estimation for fine particles at the mill speed of 88% of the critical

Parameters											
K	0.103467										
β	0.836413										
Δ_J	2.935335										
N*	136										
Δ_N	1.017754										
N* Linear model parameters											
a	-2.67781										
b	92.30461										
Experiment Data											
Particle Filling, U (-)	0	20	40	60	70	80	90	100	110	120	160
Power_Expt (Watts)	236.164	262.164	273.872	270.353	270.558	274.481	278.230	271.934	265.691	266.807	255.828
StdDev	1.901	1.855	3.315	4.083	2.660	1.835	2.833	3.738	2.261	2.534	3.524
Mill Speed (%)	88.144	88.144	88.144	88.144	88.144	88.144	88.144	88.144	88.144	88.144	88.144
Mill Speed rpm	51.782	51.782	51.782	51.782	51.782	51.782	51.782	51.782	51.782	51.782	51.782
Ball filling (J)	0.200	0.200	0.200	0.200	0.200	0.200	0.200	0.200	0.208	0.218	0.240
Internal Mill Diameter, D (m)	0.526	0.526	0.526	0.526	0.526	0.526	0.526	0.526	0.526	0.526	0.526
Mill Length, L (m)	0.180	0.180	0.180	0.180	0.180	0.180	0.180	0.180	0.180	0.180	0.180
Ball Density (Kg/m3)	7800.000	7800.000	7800.000	7800.000	7800.000	7800.000	7800.000	7800.000	7800.000	7800.000	7800.000
Particle Density (Kg/m3)	2466.667	2466.667	2466.667	2466.667	2466.667	2466.667	2466.667	2466.667	2466.667	2466.667	2466.667
Load Density (kg/m3)	4680.000	4798.400	4916.800	5035.200	5094.400	5153.600	5212.800	5272.000	5126.154	4991.111	4538.065
Model Data											
N*	136.000	136.000	136.000	136.000	136.000	136.000	136.000	89.627	89.359	89.091	88.020
δ_c	0.000	0.000	0.000	0.000	0.000	0.000	0.000	0.002	0.003	0.005	0.017
Thickness of centrifuged layer, mm	0.000	0.000	0.000	0.000	0.000	0.000	0.000	1.087	1.587	2.370	9.004
Deff	0.526	0.526	0.526	0.526	0.526	0.526	0.526	0.524	0.523	0.521	0.508
Jeff	0.200	0.200	0.200	0.200	0.200	0.200	0.200	0.193	0.198	0.204	0.240
Nceff , (rpm)	58.747	58.747	58.747	58.747	58.747	58.747	58.747	58.871	58.929	59.019	59.800
Neff , (%)	88.144	88.144	88.144	88.144	88.144	88.144	88.144	87.958	87.872	87.738	86.592
α (Radians)	0.785	0.785	0.785	0.785	0.785	0.785	0.785	0.785	0.785	0.785	0.785
Power_Model (Watts)	250.321	256.653	262.986	269.319	272.486	275.652	278.819	271.583	268.269	264.816	256.167
Δ(Expt - Mod)	-14.156	5.511	10.886	1.034	-1.927	-1.171	-0.589	0.351	-2.577	1.991	-0.339
SSE	366.6181										

Table A3.16: Power prediction with N* = 98.27 for fine particles at the mill speed of 98% of the critical

Parameters											
K	0.103										
β	0.836										
Δ_J	2.935										
N*	136.000										
Δ_N	1.018										
Experiment Data											
Particle Filling, U (-)	0	20	40	60	70	80	90	100	110	120	160
Power_Expt (Watts)	269.806	292.105	286.200	239.589	255.748	233.928	246.302	248.017	254.614	254.242	219.467
StdDev	2.560	1.973	2.421	7.700	21.309	10.519	10.765	6.281	2.731	3.320	4.773
Mill Speed (%)	98.455	98.455	98.455	98.455	98.455	98.455	98.455	98.455	98.455	98.455	98.455
Mill Speed rpm	57.840	57.840	57.840	57.840	57.840	57.840	57.840	57.840	57.840	57.840	57.840
Ball filling (J)	0.200	0.200	0.200	0.200	0.200	0.200	0.200	0.200	0.208	0.218	0.240
Internal Mill Diameter, D (m)	0.526	0.526	0.526	0.526	0.526	0.526	0.526	0.526	0.526	0.526	0.526
Mill Length, L (m)	0.180	0.180	0.180	0.180	0.180	0.180	0.180	0.180	0.180	0.180	0.180
Ball Density (Kg/m3)	7800.000	7800.000	7800.000	7800.000	7800.000	7800.000	7800.000	7800.000	7800.000	7800.000	7800.000
Particle Density (Kg/m3)	2466.667	2466.667	2466.667	2466.667	2466.667	2466.667	2466.667	2466.667	2466.667	2466.667	2466.667
Load Density (kg/m3)	4680.000	4798.400	4916.800	5035.200	5094.400	5153.600	5212.800	5272.000	5126.154	4991.111	4538.065
Model Data											
N*	136.000	136.000	136.000	98.265	98.265	98.265	98.265	98.265	98.265	98.265	98.265
δ_c	0.000	0.000	0.000	0.011	0.011	0.011	0.011	0.011	0.012	0.014	0.018
Thickness of centrifuged layer, mm	0.000	0.000	0.000	5.628	5.628	5.628	5.628	5.628	6.315	7.248	9.612
Deff	0.526	0.526	0.526	0.515	0.515	0.515	0.515	0.515	0.513	0.512	0.507
Jeff	0.200	0.200	0.200	0.165	0.165	0.165	0.165	0.165	0.169	0.173	0.181
Nceff , (rpm)	58.747	58.747	58.747	59.399	59.399	59.399	59.399	59.399	59.480	59.590	59.873
Neff , (%)	98.455	98.455	98.455	97.375	97.375	97.375	97.375	97.375	97.243	97.062	96.604
α (Radians)	0.785	0.785	0.785	0.785	0.785	0.785	0.785	0.785	0.785	0.785	0.785
Power_Model (Watts)	277.205	284.218	291.231	240.783	243.614	246.445	249.276	252.107	248.347	244.918	226.041
Δ(Expt - Mod)	-7.399	7.887	-5.031	-1.194	12.134	-12.517	-2.975	-4.090	6.266	9.324	-6.575
SSE	642.599										

Table A3.17: N* linear model parameter estimation for fine particles at the mill speed of 98% of the critical

Parameters											
K	0.103										
β	0.836										
Δ_J	2.935										
N*	136.000										
Δ_N	1.018										
N* Linear model parameters											
a	-0.050										
b	98.318										
Experiment Data											
Particle Filling, U (-)	0	20	40	60	70	80	90	100	110	120	160
Power_Expt (Watts)	269.806	292.105	286.200	239.589	255.748	233.928	246.302	248.017	254.614	254.242	219.467
StdDev	2.560	1.973	2.421	7.700	21.309	10.519	10.765	6.281	2.731	3.320	4.773
Mill Speed (%)	98.455	98.455	98.455	98.455	98.455	98.455	98.455	98.455	98.455	98.455	98.455
Mill Speed rpm	57.840	57.840	57.840	57.840	57.840	57.840	57.840	57.840	57.840	57.840	57.840
Ball filling (J)	0.200	0.200	0.200	0.200	0.200	0.200	0.200	0.200	0.208	0.218	0.240
Internal Mill Diameter, D (m)	0.526	0.526	0.526	0.526	0.526	0.526	0.526	0.526	0.526	0.526	0.526
Mill Length, L (m)	0.180	0.180	0.180	0.180	0.180	0.180	0.180	0.180	0.180	0.180	0.180
Ball Density (Kg/m3)	7800.000	7800.000	7800.000	7800.000	7800.000	7800.000	7800.000	7800.000	7800.000	7800.000	7800.000
Particle Density (Kg/m3)	2466.667	2466.667	2466.667	2466.667	2466.667	2466.667	2466.667	2466.667	2466.667	2466.667	2466.667
Load Density (kg/m3)	4680.000	4798.400	4916.800	5035.200	5094.400	5153.600	5212.800	5272.000	5126.154	4991.111	4538.065
Model Data											
N*	136.000	136.000	136.000	98.289	98.284	98.279	98.274	98.269	98.264	98.259	98.239
δ_c	0.000	0.000	0.000	0.010	0.011	0.011	0.011	0.011	0.012	0.014	0.019
Thickness of centrifuged layer, mm	0.000	0.000	0.000	5.501	5.527	5.554	5.582	5.609	6.324	7.294	9.863
Deff	0.526	0.526	0.526	0.515	0.515	0.515	0.515	0.515	0.513	0.511	0.506
Jeff	0.200	0.200	0.200	0.165	0.165	0.165	0.165	0.165	0.168	0.173	0.180
Nceff , (rpm)	58.747	58.747	58.747	59.384	59.387	59.390	59.393	59.396	59.481	59.596	59.903
Neff , (%)	98.455	98.455	98.455	97.400	97.395	97.390	97.384	97.379	97.241	97.054	96.555
α (Radians)	0.785	0.785	0.785	0.785	0.785	0.785	0.785	0.785	0.785	0.785	0.785
Power_Model (Watts)	277.205	284.218	291.231	242.104	244.669	247.227	249.776	252.318	248.254	244.460	223.814
Δ(Expt - Mod)	-7.399	7.887	-5.031	-2.514	11.079	-13.298	-3.475	-4.301	6.359	9.782	-4.347
SSE	633.769										